

Peter Grünberg Institute / Institute of Complex Systems
Bioelectronics (PGI-8/ICS-8)

Stimulation of neuronal tissue using microelectrodes: experiments with a model system and simulations

Eckhard Wehrse

Stimulation of neuronal tissue using microelectrodes: experiments with a model system and simulations

Eckhard Wehrse

Berichte des Forschungszentrums Jülich; 4352
ISSN 0944-2952
Peter Grünberg Institute / Institute of Complex Systems
Bioelectronics (PGI-8/ICS-8)
Jül-4352

Zu beziehen durch: Forschungszentrum Jülich GmbH · Zentralbibliothek, Verlag
D-52425 Jülich · Bundesrepublik Deutschland
 02461 61-5220 · Telefax: 02461 61-6103 · e-mail: zb-publikation@fz-juelich.de

Own Work Declaration

I hereby certify that this thesis is based on my own work, and no other than the stated sources and aids were used. All content that is taken literally or analogously, from published and unpublished writings, is identified as such.

Hiermit versichere ich, dass ich diese Arbeit selbstständig verfasst und keine anderen als die angegebenen Quellen und Hilfsmittel benutzt habe. Alle Inhalte, die wörtlich oder sinngemäß aus veröffentlichten oder nicht veröffentlichten Schriften entnommen wurden, sind als solche kenntlich gemacht.

Jülich, den 31. Mai 2012

Contents

1	Introduction	1
1.1	Applications, Motivation and Aims	1
1.1.1	Multielectrode Arrays	1
1.1.2	BiMEA	2
1.1.3	Challenges in Electrical Stimulation	3
1.2	Basics of Neuronal Tissue	4
1.2.1	Goldman-Hodgkin-Katz Equation	4
1.2.2	Extracellular Fluid	5
1.3	Basics of Electrostimulation	6
1.3.1	Central Physical Equations	6
1.3.2	Conditions at the Boundaries	7
1.3.3	Stimulation Pulse Forms	8
1.3.4	Safe Stimulation	13
1.3.5	Activation Function	13
2	Experiment	17
2.1	Experimental Setup	17
2.1.1	BioMas-Main-Amplifier	17
2.1.2	Headstage	18
2.1.3	Multielectrode Arrays	19
2.1.4	Setup in the Faraday Cage	27
2.1.5	Rack	29
2.1.6	Software	29
2.2	Stimulation and Recording on the same MEA	30
2.2.1	Preliminary Tests	31
2.2.2	Results	31
2.2.3	Discussion and Outlook for the Stimulation on the same MEA	40
2.3	Stimulation on a second MEA	41
2.3.1	Monopolar Stimulation	41
2.3.2	Bipolar Stimulation	45
2.3.3	Discussion and Outlook for the Stimulation on a second MEA	46
2.4	Summary and Discussion of the Experimental Part	48

3	Simulations based on an Equivalent Circuit Model	51
3.1	Fundamentals	52
3.2	R(RC)-Circuit Model of a Microelectrode	54
3.2.1	Simulating Impedance Spectroscopy Data	54
3.2.2	Simulating Cyclic Voltammetry Data	57
3.2.3	Simulating Stimulation Pulses	59
3.3	R(BVC)-Circuit Model of a Microelectrode	63
3.3.1	Butler-Volmer Model	63
3.3.2	Simulating Cyclic Voltammetry Data	65
3.3.3	Simulating Impedance Spectroscopy Data	66
3.3.4	Simulating Stimulation Pulses	67
3.3.5	Summary and Outlook	71
3.4	R-CPE-Circuit Model of a Microelectrode	71
3.4.1	Simulating Impedance Spectroscopy Data	71
3.4.2	Simulating Cyclic Voltammetry Data	73
3.4.3	Simulating Stimulation Pulses	75
3.4.4	Summary and Outlook	79
3.5	Summary and Outlook of the considered Electrode Models	79
3.6	Simulation of a two Microelectrode System based on a R(RC)-Model	81
3.6.1	Stimulation Frequency Dependence	82
3.6.2	Amplitude Dependence	83
3.6.3	Dependence on the Number of Stimulating Electrodes	83
3.6.4	Spatial Dependence	84
3.6.5	Concentration Dependence	85
3.6.6	Dependence on the Capacitance of the Recording Electrode	85
3.6.7	Parasitic Capacitance Dependence	86
3.6.8	Summary and Outlook	87
4	Finite Element Simulation	89
4.1	Motivation and Overview	89
4.2	Simulation Settings	90
4.2.1	Equations to solve	90
4.2.2	Boundary Conditions	91
4.2.3	Meshing	92
4.3	Pretests	93
4.4	Results	94
4.5	Summary and Outlook	97
	Appendices	97
	A Mathematical Methods	99
	B Software	103
	C Supplements to previous Chapters	109
	Nomenclature	117
	Acknowledgments	120
	Bibliography	122

Chapter 1

Introduction

1.1 Applications, Motivation and Aims

The electrical stimulation of neuronal tissue proves to be a growing topic in current research both in physics, chemistry and in biomedical sciences [1] [2]. Insights of this field led to powerful techniques like Deep Brain Stimulation (DBS) as a standard therapy against idiopathic dystonia, Parkinson's disease, essential tremor [3] [4] and severe forms of depression [5] [6] (see [7] for a list of reviews in the high frequency stimulation field of the last decade). A further field of application are medical prostheses like in the retina [8] or cochlea [9]. In these cases an electrical stimulation is used to influence neuronal tissue in a designated manner, often by triggering action potentials. To excite the neuron (depolarisation), the stimulation pulse drives the extracellular space to (more) negative potentials leading to a smaller absolute value of the membrane potential, which remains still negative. If the potential difference over the axon membrane rises above a given value, an action potential occurs. The principle processes of generating a physiological action potential are well understood and reviewed in literature [10] [11] [12].

1.1.1 Multielectrode Arrays

Multielectrode arrays (MEAs) are two-dimensional arrangements of electrodes acting as voltage probes or as electrical stimulators [13]. For this purpose contact is applied with electrogenic cells of neuronal, skeleton muscle or cardiac tissue. There exists a large field of application both *in vivo* [8] and *in vitro* [14]. If the diameter of an electrode is in the micrometer range, the expression *microelectrode array* is used (also abbreviated by "MEA"). A combination of several MEAs leads to a three-dimensional array (see the actual product catalog of Neuronexus Technologies, Ann Arbor, MI USA for examples).

1.1.2 BiMEA

Electrical Stimulation of the retina aims to restore vision of blind individuals, suffering from diseases like the age-related macular degeneration (AMD) and the retinitis pigmentosa (RP). AMD starts with a deposition of metabolites in the pigment epithelium, while RP leads to a loss of photoreceptors [8]. The idea of retinal prostheses is to stimulate the intact ganglion cell layer according to a signal of a digital camera outside the body. The loss of the natural detector of light is then compensated by an artificial one.

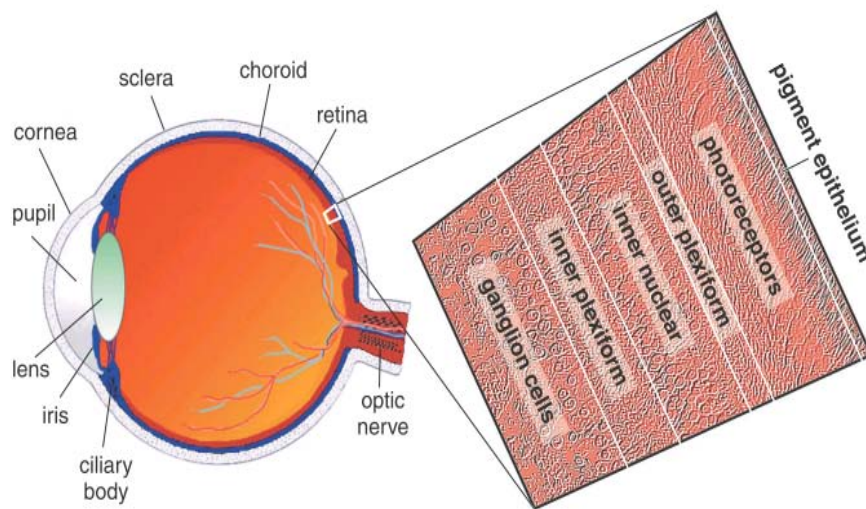


Figure 1.1: localisation and histological layers of the retina, from Helga Kolb 2003 *How the retina works* American Scientist 91:28-35 (see also [15] in the bibliography)

There are two major approaches for retinal implants: Subretinal implants are placed between bipolar cells and retinal pigment epithelium. On the contrary, epiretinal implants are attached to the barrier between the retina and the vitreous. In the BiMEA project (Bidirectional Micro-Electrode-Arrays) a microelectrode is penetrating the retina. This way, stimulating and recording electrodes are placed in different layers. A changing of the ganglion cell activity indicating the excitation can be investigated while stimulating the deeper retina layers. The physiological signal path is utilized by the experimental setup and the stimulation parameters can be adapted. A kind of “communication” might be established this way: Giving input to the remaining cones and rods and getting output from the ganglion cells, several stimulation protocols might be tested, resulting in gentle and precise stimulation protocols. The application of various electrodes surrounding a defined spot in the retina might lead to a focussed and gentle stimulation, when combined with bipolar or multipolar stimulation functions.

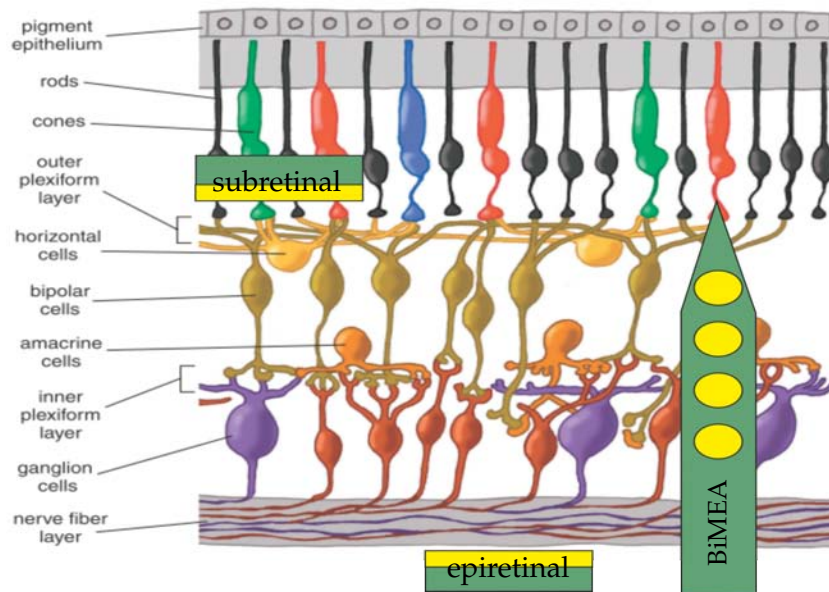


Figure 1.2: retinal prostheses in the retinal layers, modified from Helga Kolb 2003 *How the retina works* American Scientist 91:28-35 (see also [15] in the bibliography)

The BiMEA-approach has to deal with electrodes in the micrometer range and with very small distances between stimulating and recording microelectrodes. In this thesis, the influence of the stimulation on the recording is investigated and the feasibility of simultaneous stimulation and recording is studied.

1.1.3 Challenges in Electrical Stimulation

In the case of living organisms, the stimulation of neuronal tissue is a serious intervention. A fundamental understanding of the electrical and chemical properties of the electrodes and the stimulation pulses and protocols used is imperative

- to avoid damage to this sensitive tissue. Especially higher current densities [16], gas evolution [17] and dissolution of electrode material is possibly poisonous to the whole organism.
- to stimulate precisely and energy saving, since
 - the heat generated by the stimulation apparatus in biological tissue is a severe problem [18] (for long time stimulation, the temperature of surrounding tissue should not rise above 38°C, for shorter durations the limit is 42 °)
 - in many cases the battery is implanted in the body. Frequent operations are necessary to replace flat ones. *Sartorius et al.* reported the severe consequences of a delayed battery replacement [6].

If Micro-Electrode-Arrays (MEAs) are used, additional points have to be kept in mind:

- There is a high risk of mechanical damage at the operation or in daily use (section 2.1.3.1).
- The condition of the electrode can only be seen directly using scanning electron microscopy (SEM) (which might damage the passivation layer) or other complex techniques.
- Single electrodes have major differences in their electrical properties (section 3.2.1).
- The miniaturization leads to a higher rate of cross talk (section 2.2), thus reducing spatial resolution and the ability of contemporaneous stimulation and recording.

This thesis aims a deeper understanding of the stimulation with microelectrodes by investigating the electrode-electrolyte surface in an equivalent-circuit model and experiments. The propagation of the stimulus in the bulk solution is further studied with a Finite-Element simulation. Main focus is here on the ion distribution and the various potentials as the basis of neuronal stimulation.

1.2 Basics of Neuronal Tissue

Neuronal tissue consists of various types of glia cells and neurons. Most of the neurons ($\sim 10^{11}$) are part of the central nervous system. A neuron can be divided into dendrites, the soma (cell body) for receiving information and the axon, which forwards this information. Some sorts of glia cells are in charge of homeostasis and the nutrition of neurons, while others form myelin around the neurons' axons (electrical isolation). Neurons generate and distribute electrical signals (action potentials) over long distances to up to 5000 other neurons or cells of the smooth or skeletal muscle [19].

1.2.1 Goldman-Hodgkin-Katz Equation

The membrane potential of a neuron determines its excitation: It rises in the depolarisation phase when firing, and is lowered in the hyper polarisation phase afterwards. Taking three ion sorts into account, the membrane potential can be calculated [20] [10] according to

$$E_{rev} = \frac{RT}{F} \ln \left(\frac{P_{Na^+} [Na^+]_o + P_{K^+} [K^+]_o + P_{Cl^-} [Cl^-]_i}{P_{Na^+} [Na^+]_i + P_{K^+} [K^+]_i + P_{Cl^-} [Cl^-]_o} \right) \quad (1.1)$$

$P_{\text{Na}^+}, P_{\text{K}^+}, P_{\text{Cl}^-}$ stands for the permeability of the membrane concerning sodium, potassium and chloride ions and $[\text{Na}^+]_{i/o}, [\text{K}^+]_{i/o}, [\text{Cl}^-]_{i/o}$ gives the concentration within the cell or in the extracellular medium, respectively. R is the universal gas constant, T the absolute temperature and F the Faraday constant. The permeabilities of the different ion sorts in a resting neuron are in a ratio of (see amongst others [21])

$$P_{\text{K}^+} : P_{\text{Na}^+} : P_{\text{Cl}^-} = 1 : 0.04 : 0.45 \quad (1.2)$$

1.2.2 Extracellular Fluid

In the present thesis it is assumed that electrodes used in nerve tissue are not connected to the cells directly (common surface of membrane and electrode), but are surrounded by extracellular fluid (ECF). A stimulus applied by an electrode has to propagate through this medium before reaching the cell. The ECF mostly consists of water, sodium, chloride and potassium. This saline is approximated by Phosphate Buffered Saline (PBS), if the buffer of carbonic acid is replaced by phosphoric acid.

element	concentration in ECF [mM] [22]	concentration in PBS 1 × [mM] [23]	diffusion constant at infinite dilution [$10^{-9}\text{m}^2/\text{s}$] [24] [25]
Na^+	143	153	1.334
Cl^-	125.4	139.7	2.032
K^+	3.6	4.5	1.957
HCO_3^-	22.6	0	1.185
H_2PO_4^-	0.1	1.8	0.959
HPO_4^{2-}	0.8	8	1.225
Debye length	$7.8 \times 10^{-10}\text{m}$	$7.4 \times 10^{-10}\text{m}$	

The concentrations of HPO_4^{2-} and H_2PO_4^- refer to the amount of Na_2HPO_4 and KH_2PO_4 given into solution. When dissolved, the different species of the phosphoric acid determinate the pH value [25] according to Hendersson and Hasselbalch [26]. Since the second dissociation constant corresponds to the pH value of neutral water ($7.21 \approx 7$), the concentrations of both dissociation forms are nearly the same:

$$c(\text{H}_2\text{PO}_4^-) \approx c(\text{HPO}_4^{2-}) = 4.9 \times 10^{-3}\text{mol/l} = 4.9\text{mM} \quad (1.3)$$

1.3 Basics of Electrostimulation

The direct transmission of electrical signals to the neurons has two inherent advantages: First, there is no need of giving input via very specialised receptor cells. Second, the stimulation is relatively quick and easy to adapt in comparison to the injection of drugs, for example. In many cases, proximate influence on the signal processing of the nervous system is needed, when no other possibilities exist but to stimulate electrically [27].

1.3.1 Central Physical Equations

For the applied stimulation frequencies ($f \ll 10^{12}$ Hz) the laws of electrostatics can be used, leading to the time-dependent Poisson's equation

$$-\nabla^2 \Phi(t) = \frac{\rho(t)}{\epsilon_0 \epsilon_r} \quad (1.4)$$

∇^2 stands for the Laplace operator, ρ for the total charge density and Φ represents the resulting potential. ϵ_0 is the vacuum permittivity, while ϵ_r means the dielectric constant. In the next sections, the principles for the ion distribution (leading to ρ) and the boundary conditions for potentials are explained. Furthermore, it is reasoned why ϵ_r can be held constant.

parenthesis: currents

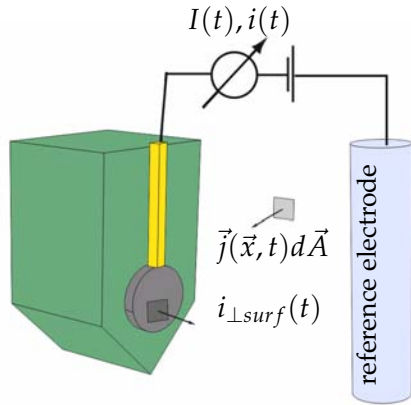


Figure 1.3: scheme for demonstrating the various meanings of "current"

Since the name "current" is often used by physicists, electrical engineers and biologists in a different manner, it is worth noting some conventions for this thesis: When a current $I(t)$ is generated, the amount of electrical charge is fully accumulating onto the electrode surface or is partly leaving the material through chemical reactions ($i_{\perp surf}(t)$). In contrary, the current density $j(\vec{x}, t)$ consists of charged particles of any kind, which have not been injected. They move because of potential gradients within the solution.

The dielectric constant ϵ_r is thought as a constant for all stimulation frequencies: *Udo Kaatz* [28] showed that changes $\geq 1\%$ are occurring for frequencies greater than 1 GHz. In the experiment the maximal frequency is at ~ 3 kHz. *Hasted et. al* [29] investigated the influence of the ion concentrations on the dielectric constant. They found an exponential decrease of the dielectric constant from 80

to 50 for ion concentrations ranging from distilled water up $2 \frac{\text{mol}}{\text{l}} = 2 \text{ M}$. Though, for $c \sim 150 \text{ mM}$ ϵ_r can be approximated by the value of pure water ($\epsilon_{r,\text{H}_2\text{O}} = 80.1$, see [25]).

All ions, representing electrical charges in a fluid, obey a few physical laws: The combination of continuity equation for the conservation of mass

$$\partial_t c + \vec{\nabla} \cdot \vec{j}_{ions} = 0 \quad (1.5)$$

and A.E. Fick's First Law

$$\vec{j}_{ions} = -D \vec{\nabla} c \quad (1.6)$$

is also known as Fick's second law. \vec{j}_{ions} means the flow of ions per area, D is the diffusion coefficient and c the ion concentration.

Ohm's law is given for aqueous solutions by:

$$\vec{j} = - \underbrace{zF\mu c}_{=\sigma} \vec{\nabla} \Phi \quad (1.7)$$

z is the charge number of the ions, F the Faraday constant and μ the ion's mobility. For low concentrations (like here) the electrical conductivity is proportional to the total ion concentration [30]. For PBS $1 \times$ a conductivity of $16.4 \frac{\text{mS}}{\text{cm}}$ was measured (using *Seven Easy* from Mettler Toledo, Columbus, USA). The combination of the equations 1.5, 1.6, 1.7 is also known as the *Nernst-Planck equation*, leading to the *Poisson-Nernst-Planck equation* (PNP) if Poisson's equation (eq. 1.4) is implemented.

1.3.2 Conditions at the Boundaries

For insulators, the external potential has to fulfil the *von Neumann* boundary conditions (BC)

$$\underbrace{\sigma \vec{\nabla} \Phi}_{\vec{j}} \cdot \vec{n} = 0 \quad (1.8)$$

while for an (ideal) conductor, the Dirichlet conditions are applied

$$\Phi(r \in \text{surface}) \stackrel{!}{=} \Phi_{\text{surface}} \quad (1.9)$$

The *Robin BC* are a mixture of both, describing a non-ideal conductor [31].

External potential in the saline ¹

If a voltage is applied between a metal surface and a reference electrode, the

¹For the interesting reader a comprehensive review article on the electrical stimulation of biological tissue [1] is recommended.

hydrated ions will migrate to the applied surface in accordance to their electrical charge. This accumulation of opposite charge leads to an exponential drop of the external potential. At the debye-length there is $\frac{1}{e}$ of the value at the surface left. This can be analytically derived by solving the PNP for a simple geometry or in the one-dimensional case (see also [1]). The debye-length of a system containing various ions i is given by

$$\lambda_D = \sqrt{\frac{\epsilon_0 \epsilon_r k T}{e^2 \sum_i z_i^2 n_i}} \quad (1.10)$$

ϵ_0 refers to the dielectric constant, ϵ_r to the relative permittivity, k is the Boltzmann constant and T the absolute temperature. The influence of ions is implemented by their charge normed to the elementary charge z_i and their number per volume n_i . The drop of the external potential in the range of the debye-length results in a storage of electrical charge. The equation for the ideal capacitor ($C \propto \frac{1}{\text{plate distance}}$) has therefore to be adapted to $C \propto \frac{1}{\lambda_D}$. In fact, the Gouy-Chapman-Stern-theory [32] [33] derives the capacitance of such a metal in an electrolyte:

$$\frac{1}{C_{dl}} = \frac{d}{2\epsilon_r \epsilon_0} + \frac{\lambda_D}{\epsilon_r \epsilon_0 \sqrt{1 + \frac{b^2}{4}}} \quad (1.11)$$

with b as a measure for the charge density at the surface:

$$b = \frac{ze\sigma\lambda_D}{kT\epsilon_0\epsilon_r} \quad (1.12)$$

1.3.3 Stimulation Pulse Forms

1.3.3.1 Current controlled Stimulation

In the case of current controlled stimulation, the voltage is adapted with very quick response. The amount of current is consequently readjusted until the value is achieved which is dictated by the stimulation function. In the hope, that nearly all chemical reactions are reversible, **charge-balanced current pulses** take care, that anodic ($I(t) < 0$) and cathodic ($I(t) > 0$) pulses have the same integral over time:

$$\int_0^{f^{-1}} I_+ dt = Q_+ \stackrel{!}{=} Q_- = \int_0^{f^{-1}} I_- dt \quad (1.13)$$

Q_+ (Q_-) stands for the positive (negative) charge and f for the stimulation frequency. If $Q = C \cdot U$ is taken as a first assumption, the applied voltage increases steadily in the anodic pulse, remains high when there are no currents and decreases in the cathodic pulse (see figure 1.4). According to equation 1.29, different voltages

are needed for the higher cathodic pulse than for the lower anodic pulse afterwards ($I \propto \exp(\eta)$) (η refers to the overpotential). The applied voltages induces chemical reactions, which are in general not reversed by the following smaller positive voltage. Though, this shall be seen as a first successful [16] [2] effort to make stimulations more gentle for surrounding tissue. As described in section 2.1.3.2, another disadvantage of current controlled stimulation exists: For a decreasing stimulation frequency, a higher amount of electrical charge accumulates in one phase on the electrode. If this accumulation exceeds a limit, which is called charge capacity, the voltage crosses the standard potentials of the gas evolution (see section C.1). With the term “gas evolution” the creation of hydrogen and oxygen gas from water is meant, as it is described below (Table 1.1). Even the evolution of Cl-gas is possible at thick iridium oxide films (IrOx) [34]. For long term stimulations an accumulation of charges is possible in this manner, leading to hazardous peak voltages. The stimulation amplitudes are in a range of $i \lesssim 1 \frac{\text{A}}{\text{cm}^2}$.

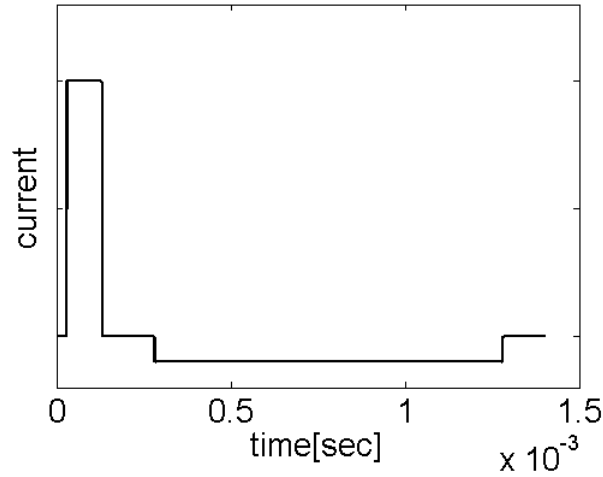


Figure 1.4: a typical charge balanced pulse

1.3.3.2 Voltage controlled Stimulation

In the voltage controlled stimulation, a certain voltage with the shape of the pulse function is applied between the working electrode and the counter electrode ¹. Though it is physically more intuitive (solution of Poisson’s equation (eq. 1.4)), the creation of charge-balanced pulses is critical. They are achieved easily only if

¹Another stimulation mode is the application of a current flowing from working to counter electrode. The amount of current is chosen in a way, that ensures the working electrode to remain on the potential required [1]

the injected currents follow the ohmic law:

$$\int_{t=0}^T U_{+/-} dt \underset{\text{if and only if } U \propto I}{=} Q_{+/-} \quad (1.14)$$

Electrical charges enter the solution via chemical reactions, which strongly depend on the applied voltage. Consequently, applying the same integrals for anodic and cathodic pulse cannot be implemented in a voltage controlled stimulation. The stimulation amplitudes are in a range up to 3.5 V [35] [3]. When capacitive stimulation is predominant and rectangular pulse shapes are chosen, the current in the medium runs into singularities (according to $I = C \cdot d_t U$). As a consequence voltage controlled stimulation with rectangular pulse shapes is rarely used [1] and will not be discussed here in detail.

1.3.3.3 Stimulation Pulse Frequencies

A large frequency spectrum and different shapes of the stimulating pulses exist both for the voltage and for the current controlled stimulation: In Deep Brain Stimulation (DBS) pulses in the range of 10^{-4} s are applied [3], while *Freeman et al.* [36] were able to activate retinal cell types selectively with frequencies ranging from 5 Hz to 100 Hz. Also new pulse forms are studied. Besides current developments in DBS [27], pulse shapes emerge, which take electrode materials into account or promise energy-saving effects ([37]). In the *Switched capacitor* approach, a capacitor is discharged very quickly, generating current peaks in the ranges of $10 \mu s$ [38]. Since the ideal stimulation function clearly remains a field of current investigations, this thesis focuses on the sinusoidal stimulation as the basis of many pulse shapes.

1.3.3.4 Capacitive Stimulation

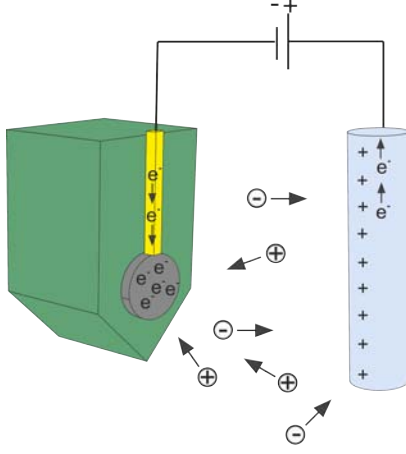


Figure 1.5: scheme of a capacitive stimulation leading to a change of the ion concentration

For a purely capacitive stimulation no charge is transferred across the electrode-electrolyte-border ($j_{\perp surf}(t) = 0, \forall t$). The electrical charges applied at the surface of the electrode create a potential, which demands Poisson's equation (eq. 1.4). This potential induces a movement of ions ($j(\vec{x}, \theta, \phi, t)$) in the bulk solution building up an "internal" potential, which is weakening the external one. (See section 4.2.1 for the equations in detail.)

1.3.3.5 Faradaic Stimulation

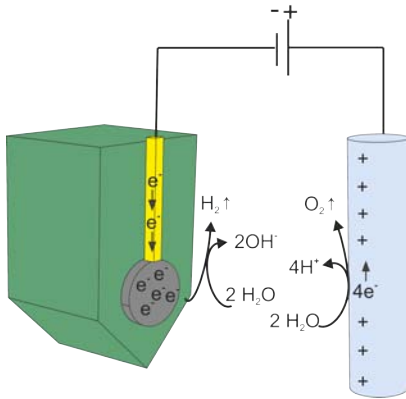


Figure 1.6: scheme of the faradaic stimulation leading to chemical reactions

If the stimulation voltage increases, electrochemical reactions (*faradaic currents*) can occur (oxidation and reduction), resulting in a crossing of electrical charges through the electrode-electrolyte surface ($j_{\perp surf}(t) \neq 0$). The faradaic current is limited in its inherent reactions by the voltage drop and in its quantity by the current applied ($I(t)$). Also the amount of educts being available at the surface restricts the reactions, which leads to a transport limitation for longer stimulation pulses ($> 10^{-4}$ s).

In a faradaic stimulation, multiple chemical reactions can occur (see Table 1.1). In the term *IrOx* all oxidation species of iridium are included. The voltage range confined by the standard potentials of the hydrogen and oxygen evolution is called "water window" [40]. Na^+ , K^+ and Cl^- change their oxidation state at higher voltages.

INTRODUCTION

reaction name	reaction	st. pot.	eq. no.	source
oxidation of water	$2\text{H}_2\text{O} \rightarrow \text{O}_2 \uparrow + 4\text{H}^+ + 4\text{e}^-$	1.229	(1.15)	[1]
reduction of water	$2\text{H}_2\text{O} + 2\text{e}^- \rightarrow \text{H}_2 \uparrow + 2\text{OH}^-$	-0.828	(1.16)	[1]
oxide formation & red.	$\text{IrO} + 2\text{H}^+ + 2\text{e}^- \rightleftharpoons \text{Ir} + \text{H}_2\text{O}$	-	(1.17)	[1]
oxide formation & red.	$\text{IrO}_2 + 4\text{H}^+ + 4\text{e}^- \rightleftharpoons \text{Ir} + 2\text{H}_2\text{O}$	-	(1.18)	[1]
oxide formation & red.	$2\text{IrO}_2 + 2\text{H}^+ + 2\text{e}^- \rightleftharpoons \text{Ir}_2\text{O}_3 + 2\text{H}_2\text{O}$	-	(1.19)	[1]
oxide formation & red.	$2\text{Ir} + 6\text{OH}^- \rightleftharpoons \text{Ir}_2\text{O}_3 + 2\text{H}_2\text{O} + 6\text{e}^-$	0.098	(1.20)	[25]
iridium chloride evol.	$\text{Ir} + 6\text{Cl}^- \rightarrow [\text{IrCl}_6]^{3-} + 3\text{e}^-$	0.77	(1.21)	[25]
reduction of IrOx	$\text{Ir}^{4+} + \text{e}^- \rightleftharpoons \text{Ir}^{3+}$	-	(1.22)	[2]
reduction of IrOx	$\text{Ir}^{3+} + \text{e}^- \rightleftharpoons \text{Ir}$	1.156	(1.23)	[25]
Ir hydroxide formation	$\text{Ir}(\text{OH})_n \rightleftharpoons \text{IrO}_n(\text{OH})_{n-x} + x\text{H}^+ + x\text{e}^-$	-	(1.24)	[2]
sodium reduction	$\text{Na}^+ \rightleftharpoons \text{Na}$	-2.71	(1.25)	[25]
potassium reduction	$\text{K}^+ \rightleftharpoons \text{K}$	-2.931	(1.26)	[2]
chlorine gas evolution	$2\text{Cl}^- \rightarrow \text{Cl}_2 \uparrow + 2\text{e}^-$	1.358	(1.27)	[1] [25]

Table 1.1: reactions at a faradaic stimulation with IrOx (no claim to be complete), *st. pot.* refers to the standard reduction potential vs. Standard Hydrogen Electrode at 1013.35 hPa and 298.15 K according to [25]. See also [39] and [40]

To calculate a potential E referred to another reference electrode from the standard potential $E_{st.p.}$ and to another pH than 0, equation 1.28 can be used (similar in [39]):

$$E = E_{st.p.} - E_{ref.el} - 59.16 \frac{\text{mV}}{\text{pH}} \quad (1.28)$$

$E_{ref.el}$ means the reference electrode potential when taking the standard hydrogen electrode as reference.

Butler-Volmer Equation

What is the amount of faradaic current flowing through the electrode-electrolyte surface, when applying a certain voltage? John A.V. Butler and Max Volmer developed an equation to answer this question [41]

$$i = F A k^0 \left(C_O(0, t) e^{-\alpha f (E - E^{0'})} - C_R(0, t) e^{(1-\alpha) f (E - E^{0'})} \right) \quad (1.29)$$

F refers to the Faraday constant, A is the area of the electrode, k^0 stands for the standard rate constant, $C_O(0, t)$ means the concentration of the oxidized reactant directly at the surface (therefore the first argument (coordinate) is symbolically set zero), while $C_R(0, t)$ is the concentration of the reduced reactant. α stands for the transfer coefficient, the abbreviation $f = \frac{F}{RT}$ is used and $E^{0'}$ means the reference potential.

The Equilibrium Potential or Nernst-Potential E_{eq} is given by Walther Nernst as

$$E_{eq} = E^{0'} + \frac{RT}{F} \ln \left(\frac{C_O^*}{C_R^*} \right) \quad (1.30)$$

C_O^* (C_R^*) stands for the concentration of the oxidized (reduced) reactant in the bulk. Introducing a physical quantity called exchange current i_0

$$i_0 = F A k^0 C_O^{*(1-\alpha)} C_R^{*(\alpha)} \quad (1.31)$$

equation 1.29 can be transformed into a more convenient form:

$$i = i_0 \left(\frac{C_O(0, t)}{C_O^*} e^{-\alpha f \eta} - \frac{C_R(0, t)}{C_R^*} e^{(1-\alpha) f \eta} \right) \quad (1.32)$$

$\eta = E - E_{eq}$ stands for the overpotential.

If the potential of the reference electrode is similar to the potential of the IrOx electrode, the concentration of any reactant at the surface is approximately equal to the bulk concentration. As a first assumption (valid for short stimulation pulses) $C_{O/R}(0, t)$ is almost constant over time. Then $C_{O/R}(0, t)$ is similar to $C_{O/R}^*$ and equation 1.32 is reduced to:

$$i = i_0 \left(e^{-\alpha f \eta} - e^{(1-\alpha) f \eta} \right) \quad (1.33)$$

1.3.4 Safe Stimulation

Harnack et al. [16] studied the influence of different current densities and stimulation treatment durations on the subthalamic nucleus of rats. According to histological examinations, they concluded that a stimulation with a frequency of 130 Hz and a pulse width of 60 μ s did not "produce any relevant tissue damage". They used charge densities up to 26 $\frac{\mu C}{cm^2 \text{ phase}}$ and maximal current densities of $1.30 \times 10^5 \frac{\mu A}{cm^2}$ leading to a applied charge of $1.8 \times 10^{-2} \frac{\mu C}{cm^2}$.

1.3.5 Activation Function

In simulations, criteria for a successful activation of neuronal tissue are needed. As an addition to the membrane potential (eq. 1.2.1) a model is introduced relying on a Hodgkin Huxley model (see [42]).

To understand the idea behind this approach a view on Poisson's equation is necessary again (eq. 1.4). If the electric potential is calculated, for example by assuming an ohmic resistor for the nerve tissue [3] [31], no ion distribution is determined directly (as in the case of the Finite-Element-Simulation in chapter 4). With the assumption, that the ions are distributed according to Poisson, the question "is

the cell stimulated?" is answered by the external electrical field instead of the local ion concentration. If the second derivative of the extracellular potential $\frac{d^2 V_e}{dx_i^2}$ exceeds a certain threshold for some $x_i \in \{x, y, z\}$, a neuron at this precise position will fire with a high probability according to the model. The spatial adjustment of neurons in a united cell structure is ignored. In a first step the relationship between stimulation duration and threshold current for activation ("Strength duration curve") [11] [1] is calculated from an ordinary Hodgkin-Huxley model.

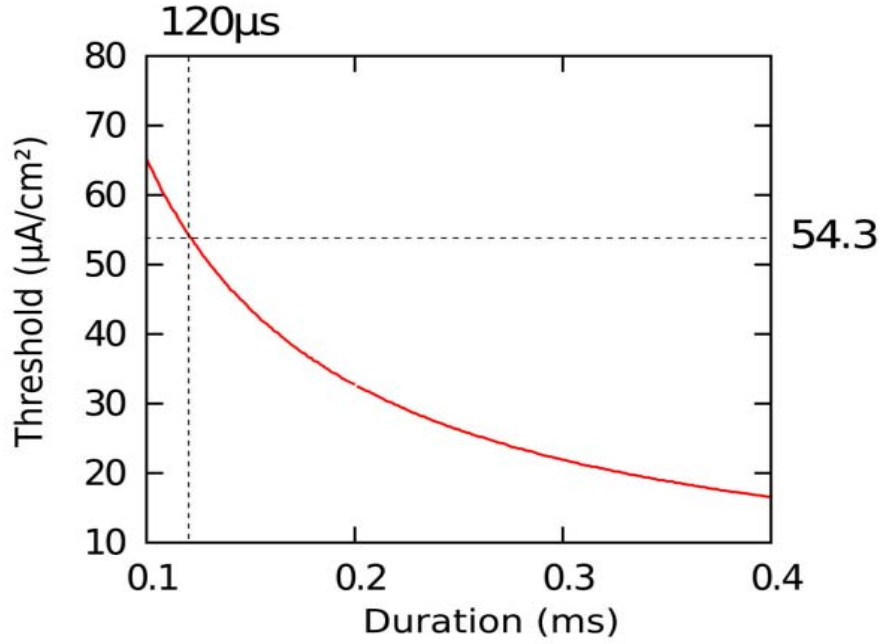


Figure 1.7: strength-duration curve calculated with a Hodgkin-Huxley-Model, taken from Julia Buhlmann et al. *Modeling of a segmented electrode for desynchronizing deep brain stimulation* Frontiers in Neuroengineering, 2011 (see also [3] in the bibliography)

For a chosen stimulation duration the threshold current I is assigned and the Activation function S can be calculated via

$$I_{thr} = \frac{S}{\bar{r}_s} \quad (1.34)$$

I_{thr} refers to the threshold current and \bar{r}_s is the axon's resistivity, which is modelled as a cylinder:

$$\bar{r}_s = \rho \frac{l}{\pi r^2} \quad (1.35)$$

with the axoplasmic resistivity ρ , l and r the axon's approximate length and radius. For the retina these parameters are listed in Table 1.2.

The total resistivity of an axon observed is therefore $\bar{r}_s = 1.45 \times 10^7 \Omega$, when the

parameter	values	source
axon resistivity	70 Ωcm	[43]
length of rod bipolar cell's axon	65 μm	[44]
radius of rod bipolar cell's axon	1 μm	ICS-4

Table 1.2: parameters and their estimated values needed for the calculation of the Activation function. The value for the axon radius comes from Sonia Biswas, M.Sc., Institute of Complex Systems 4 - Cellular Biophysics. It is compatible to [43]

axon is approximated by a cylinder.

The relationship of the duration to the current for a successful stimulation is given by the strength-duration curve. It can be described [3] by

$$I_{th} = \frac{I_{rh}}{1 - \exp(-\frac{W}{\tau_m})} \quad (1.36)$$

I_{th} is the threshold current, W the pulse width and τ_m a membrane time constant. The rheobase current I_{rh} is the amount of current that is needed for the stimulation of a neuron using a pulse of endless duration ($W \rightarrow \infty$). τ_m is estimated to be similar to the membranes of the neurons, which DBS uses to stimulate (see [3]): According to a stimulus duration of 100 ms a threshold current of $65 \frac{\mu\text{A}}{\text{cm}^2}$ is necessary. Via $I_{th} = \frac{S}{\bar{r}_s}$ the Activation function yields $940 \frac{\text{V}}{\text{cm}^2}$.

INTRODUCTION

Chapter 2

Experiment

2.1 Experimental Setup

2.1.1 BioMas-Main-Amplifier

For the measurements 16 channels of a 64-channel readout-system consisting of headstage (see section 2.1.2) and main amplifier was used. The system was recording at a sampling rate of 10^4 Hz and able to stimulate at 1.25×10^6 Hz with maximal two different stimulation functions, which can be applied on an arbitrary number of channels. The main amplifier has a hundred-fold magnification and a variable high-pass filter ranging from 0 Hz to 72 Hz. For further documentation see [45] [46] [47].

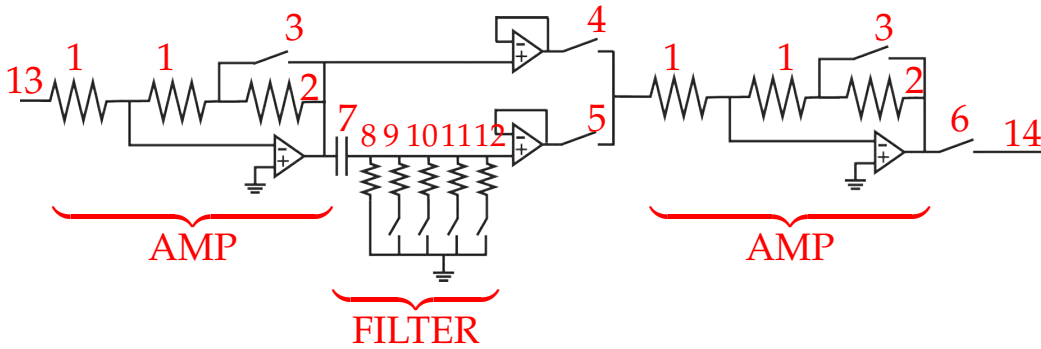


Figure 2.1: scheme of the mainamplifier developed and built in the Institute of Complex Systems-8

When the signal comes from the pre-amplifier (78-pin, 13), the first amplification takes place. The amplification (AMP) consists of an ohmic resistance R (1), followed by a switchable (3) resistor $9 \times R$ (2). A tenfold amplification can be selected this way. The same amplification subsystem can be found also at the end, so that the complete system is able to amplify $10^0 \times$, $10^1 \times$ or $10^2 \times$. In the alternating

current(AC) coupled mode (5) the high pass filter (FILTER) consists of a capacitor (7) to block directive current and ohmic resistances ranging from 5 M Ω to 1 k Ω (8 ... 12). Time constants ($1/e$) $\tau \in \{11, 1, 0.1, 0.01, 0.002 s\}$ can be set this way. Also directive current (DC) measurement is possible (4). After a second amplification, there is a switch to the analog-digital converter (6), the output leads to a 64-channel data acquisition module (NI PCI-6071E, National Instruments, Austin Texas, 14).

2.1.2 Headstage

While three different headstages were built in the electronic workshop of the institute, only the last version was used to collect the data presented in thesis. The two previous designs can be found in the appendix (C.3). They turned out not to be sufficient to resolve the differences of the recording channels, which resulted in a common signal more or less for all 16 channels. The headstage presented here was custom-designed for this experiment. A simple design was aimed at with feedlines as short as possible to reduce crosstalk. Moreover, the sites of the four-shank Neuronexus MEA (see section 2.1.3.1) were directly assigned to the recording channels.

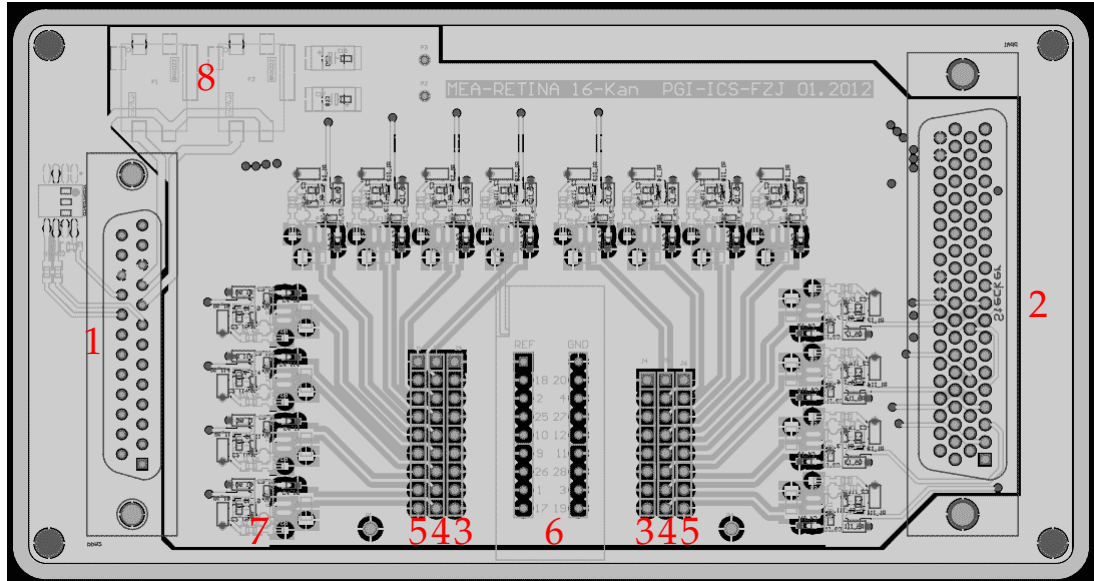


Figure 2.2: custom designed headstage for the 16-channel Neuronexus-electrodes

The preamplifier has to be connected at the power supply adapter (1) and at the data cable adapter (analog, originally for 64 channels) (2). When stimulating, an external cable is connected to one of the socket pins (3), while the amplifier

pin (4) and ground pin (5) are connected as well to prevent cross talk in the main amplifier. The central socket-row (6) fits in the Omnetics Adapter (Fig. 2.1.3.1), in order to connect a multielectrode to the system via plug-and-play. For an appropriate data recording, there is an operational amplifier 124X (OPA124, Texas Instruments, Dallas Texas) (7) and a noise filter (8). Figure 2.11 shows the headstage integrated in the setup.

2.1.3 Multielectrode Arrays

A principal point of a neuronal implants are the electrodes. Together with the lower fraction of the feedlines, they are the only part within the neuronal tissue and inherent the only metal which comes into direct contact with the neurons. For recording and particularly for stimulation a precise knowledge of the geometry and the electrochemical characteristics of the electrodes is imperative.

2.1.3.1 Geometrical Properties and Manufacturer Information

Two types of multi-microelectrodes are used in this thesis. Both are "silicon micro-electrode arrays" produced by NeuroNexus Technologies[®] (Ann Arbor, MI USA) and are designed to record and to stimulate brain regions in depth up to 10 mm both in acute as well as in chronic experiments.

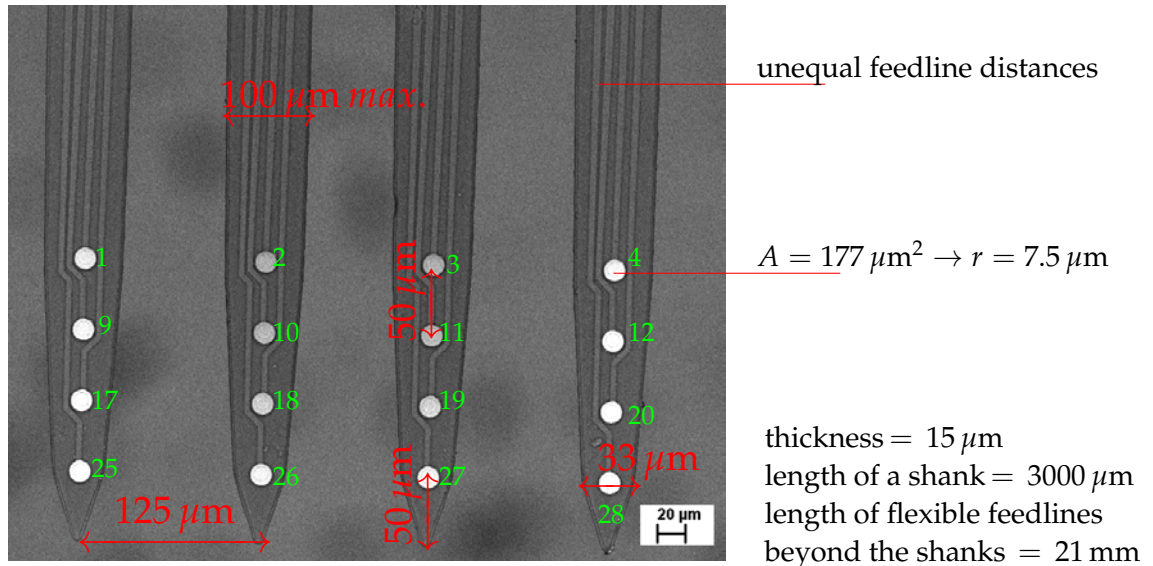


Figure 2.3: SEM-picture of a Multielectrode of the type $A4 \times 4 - 3MM50 - 125 - 177$ with channel assignment (small numbers)

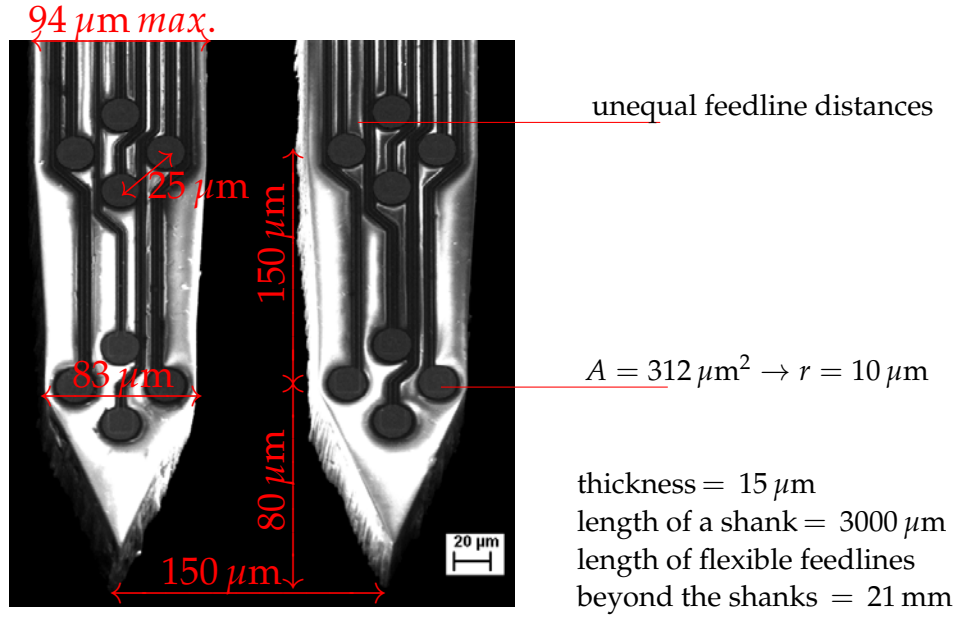


Figure 2.4: SEM-picture of a Multielectrode of the type $A2 \times 2 - TET - 3MM150 - 150 - 312$

Both MEA types have a total length of 3 mm and are 15 μm thick, what makes them sophisticated and not easy to handle. Because the distances between the electrodes in the four-shank type are equal and the shape is adequate to the BiMEA-project, it was mostly used. The electrode area of the two shank-type MEA is approximately two times greater, which leads to stronger stimulation pulses. This was utilized when dealing with two MEAs in section 2.3.

Mechanical Stability Out of eight electrodes that were used for this thesis three got broken in the 12-month-period. Because of the size in the 100 μm range, efforts to collect the leftovers were successful not even in a single case. It has been a question, how to preserve the remainings, so they cannot be sucked in the vacuum pump of the sputtering machine and the SEM. To prevent mechanical damage a cage was constructed. Screws were used to ensure that all parts except the board where the microelectrode is glued onto, can be removed. For Scanning Electrode Microscopy and preliminary experiments it was necessary to remove parts of the cage. To be able to connect the electrode with two different adapter systems, the plate just in front of the feedlines (6) is removable.

Experimental Setup

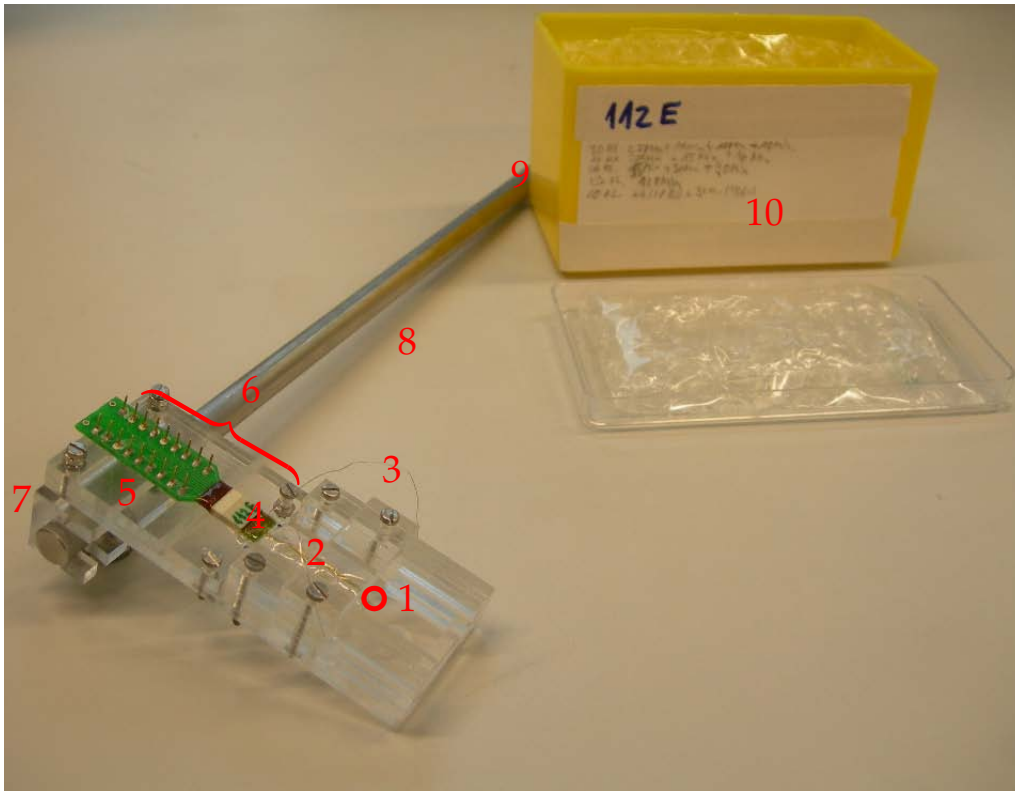


Figure 2.5: MEA, cage and box

- 1 Multielectrode tip with up to four shanks
- 2 feedlines glued on a acrylic glass board
- 3 Reference/Ground Ag/AgCl-electrode (in the experiments the Ag/AgCl-pellet E206 (In Vivo Metric, Healdsburg, California) was used instead)
- 4 Connection to Omnetics Adapter, labeled with electrode name
- 5 Omnetics-to-DIL Adapter
- 6 upper one of two removable acrylic glass boards
- 7 C-shape part which is fixed by additional screws on the backside to the rod made of steel 8
- 9 preservation box (cushioned) with multielectrode name
- 10 Information about electrode usage was documented for an overview of degeneration)

Assignment of channels To assign the geometrical sites of the multielectrode to the recording channels, the manufacturer's information for the part up to the Omnetics Adapter, the Omnetics Adapter's data sheet and the setting of the custom made headstages had to be connected. Since - at one time - just two shanks out of the four got broken, the assignment was able to be evaluated. The channel

EXPERIMENT

definitions can be seen at Fig. 2.3 and Fig. 2.4, while the assignment to the headstage (section 2.1.2) will be explained in the next lines.

Omnetics Adapter In order to understand some of the results later, a detailed view on the feedlines is necessary:

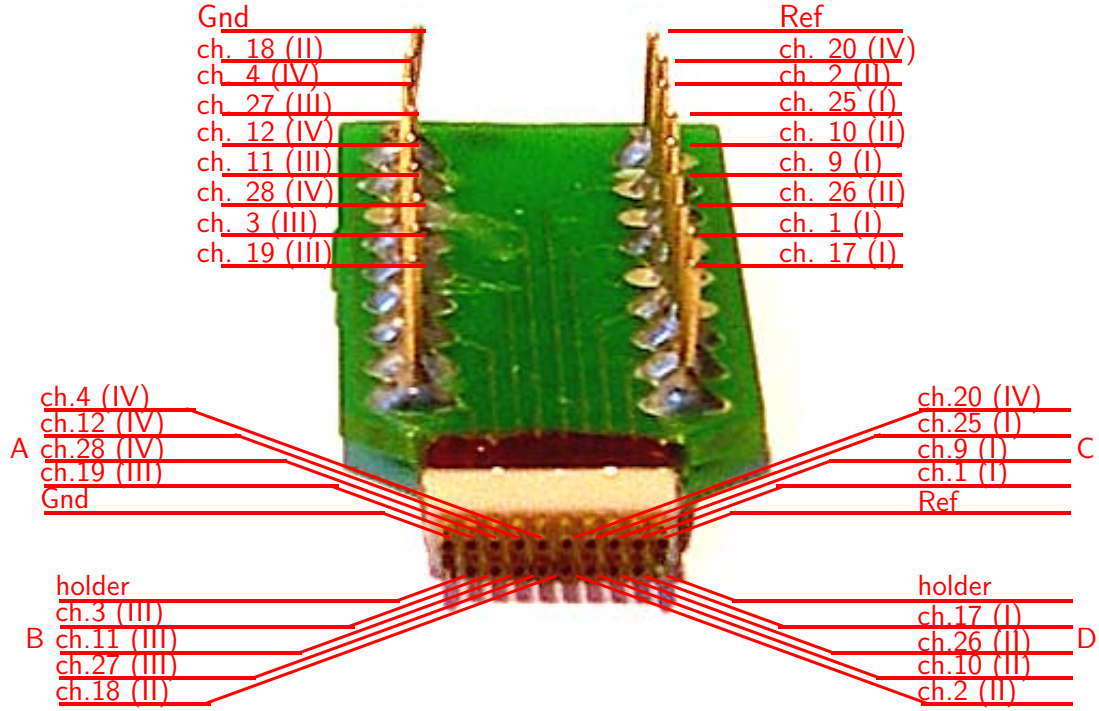


Figure 2.6: Omnetics adapter which is used to connect the microelectrodes with the DIL-socket; channels of the four shank multi-electrode in arabic, their shanks in roman numbers

At the two columns of pins, a two-fold symmetry can be declared: On the right-hand side there are the feedlines for the electrodes of the first and second shank, on the left-hand side of the third and fourth. This symmetry is broken by channels **18** and **20**, which have been switched. This circumstance is important for the discussions of the experimental results in section 2.2. Also the female connectors at the front have a symmetry: Every quarter of connectors (**A,B,C,D**) contacts the electrode of one shank, except one which comes from a shank with a number one less ($IV \rightarrow III$, $III \rightarrow II$, $II \rightarrow I$, $I \rightarrow IV$).

2.1.3.2 Electrochemical Characterisation

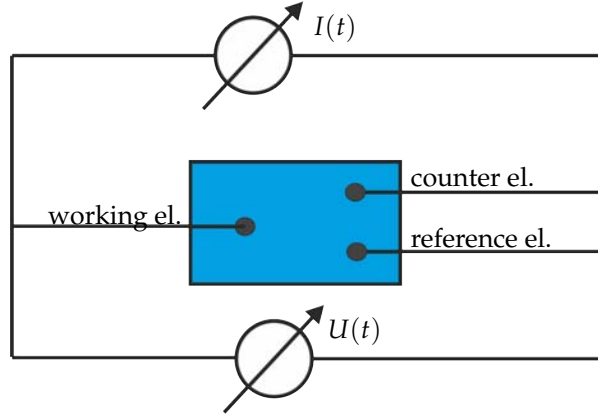


Figure 2.7: scheme of an EIS setup

The **electrical impedance spectroscopy** is one of the most common tools of characterising the frequency-dependent impedance of electrodes. In the potentiostatic mode a sinusoidal voltage is applied with low amplitudes between the working and the reference electrode and the current is measured which flows from the working to the counter electrode. For a precise measurement, the counter electrode has to have a low impedance (high electrochemical active area), absorbing nearly all currents. This procedure is normally done for a large scale of frequencies ($f = 10 \text{ Hz} \dots 10^4 \text{ Hz}$). The **cyclic voltammetry** uses the same setup, thus applying a slow varying voltage (typically $100 \frac{\text{mV}}{\text{s}}$) for a greater voltage range ($-0.8 \text{ V} \dots 0.8 \text{ V}$). In dependence of the charge placed onto the electrode, the current for a certain voltage is different. This leads to a hysteresis effect, which allows to determine the capacitance of the electrode.

Impedance spectroscopy The impedance of a microelectrode of the four-shank type (Fig. 2.3) is measured for 51 different frequencies (Fig. 2.8). The range of possible stimulation frequencies is within the limits of 10 Hz and 10 kHz. The linear behaviour of the impedance in a double-logarithmic plot is typical for electrodes in the μm -range [48] [2]. The impedance data presented cannot be compared directly to experimental data of Neuronexus (Fig. C.1). There the impedance was tenfold higher, though with different salines and times of usage. In discussions about the impedance, normally either the impedance at 1 kHz is mentioned ($\sim 0.2 \text{ M}\Omega$ in this case) or the parameters of a fitted model are given, especially the capacitance. In chapter 3 the parameters of three models are fitted to this data.

EXPERIMENT

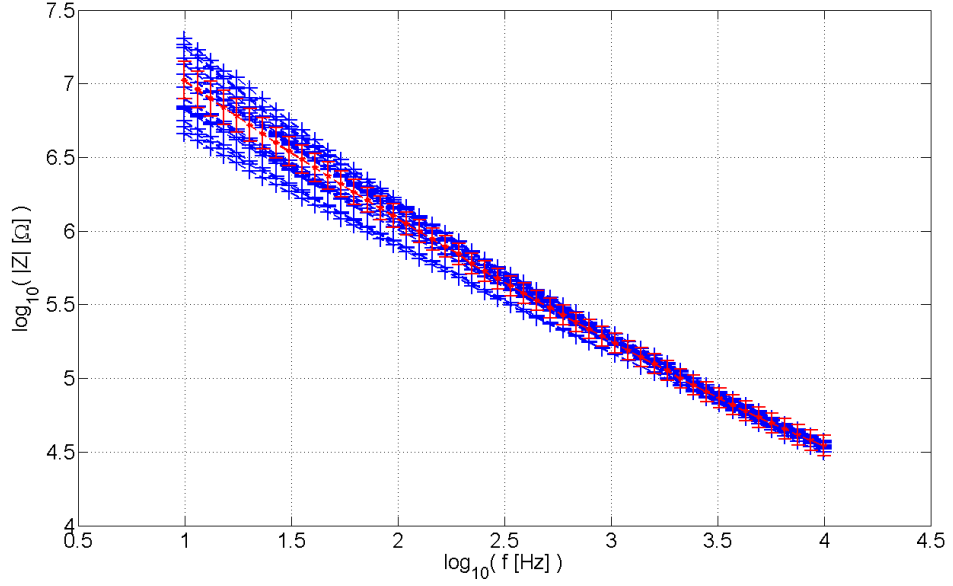


Figure 2.8: impedance spectroscopy graphs of all electrodes of MEA 13710 (blue) and their mean (red)

Cyclic voltammetry In many cases a “charge capacitance” is calculated by the impedance spectroscopy [2] [40]. It describes the maximal charge Q_{max} , before the applied voltage exceeds the water window and chemical reactions occur.

$$2 \times Q_{max} = \int_{t(U_{min})}^{t(U_{max})} Idt = \int_{U_{min}}^{U_{max}} I \frac{1}{dV/dt} dV = \int_{t(U_{min})}^{t(U_{max})} I \frac{1}{v_{sweep}} dV \quad (2.1)$$

v_{sweep} is called sweep-rate and is held constant. In principle, a distinction between $Q_{max,+}$ and $Q_{max,-}$ would be necessary, which are both averaged to Q_{max} . The charge capacity is therefore represented by the half of the inner area of a cyclic voltammetry graph divided by the sweep-rate.

In literature, there exist many data for the relative charge capacity of Ir and its oxidation forms (see Table 2.1). The results are varying much and are partially contradicting each other. Though, a range of $1 - 10 \frac{mC}{cm^2}$ seems reasonable. The MEA which was used in the experiments, was characterized by a cyclic voltammetry (Fig. 2.9). The voltage is varied using a sweep rate of 100 mV/s . It was set 0 V by the potentiostat, when no currents were detected (at the beginning of the voltage sweeping). The maximal charge capacity for this case is calculated to $Q_{max} = 6.5 \times 10^{-8} C \cong 36.7 \frac{mC}{cm^2}$. A calculation of the "charge capacity" to the capacity of

Table 2.1: Charge capacities of Ir and IrOx in literature

source	iridium	iridium oxide
Neuronexus (Fig. C.1)	100 – 150 $\frac{\mu\text{C}}{\text{cm}^2}$	1.2 $\frac{\text{mC}}{\text{cm}^2}$
[2](activated)	—	1 – 5 $\frac{\text{mC}}{\text{cm}^2}$
[2](thermal)	—	$\approx 1 \frac{\text{mC}}{\text{cm}^2}$
[2](sputtered)	—	1 – 5 $\frac{\text{mC}}{\text{cm}^2}$
[48](sputtered & activated)	—	4.91 $\frac{\text{mC}}{\text{cm}^2}$
[48](sputtered & activated)	—	7.91 $\frac{\text{mC}}{\text{cm}^2}$
[49] (activated)	—	$\leq 0.8 \frac{\text{mC}}{\text{cm}^2}$
[49] (unactivated, gassing limit)	—	$\leq 9 \frac{\text{mC}}{\text{cm}^2}$
[49] (activated, gassing limit)	—	$\leq 40 \frac{\text{mC}}{\text{cm}^2}$
[50] (activated)	—	$\leq 43.8 \frac{\text{mC}}{\text{cm}^2}$
[51] (activated)	—	10 $\frac{\text{mC}}{\text{cm}^2}$
[52] (activated)	—	7.37 $\frac{\text{mC}}{\text{cm}^2}$

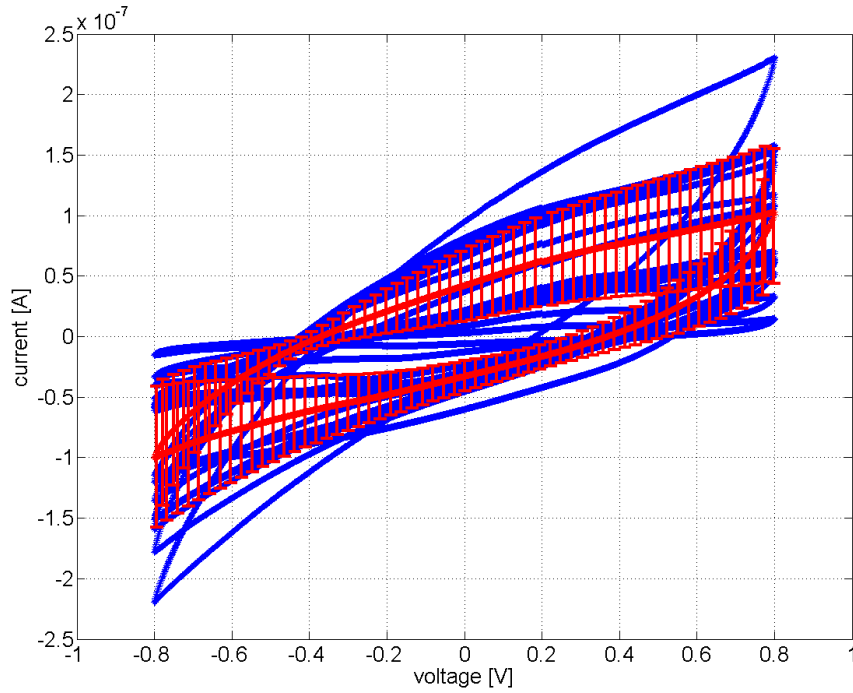


Figure 2.9: cyclic voltammetry data of MEA 112E. The current of each of the 16 electrodes is presented in blue, their arithmetic mean in red. For a better overview just every 20th errorbar is shown, standing for the RMS.

the electrode seen as an ideal capacitor can be done using the capacitor equation:

$$C = \frac{2 Q_{max}}{|U_{max} - U_{min}|} = \frac{2 \times 6.5 \times 10^{-8} \text{ C}}{1.6 \text{ V}} \quad (2.2)$$

$$= 8.2 \times 10^{-8} \text{ F}$$

This leads to a relative capacitance of $46.1 \frac{\text{mF}}{\text{cm}^2}$. These values intend a much higher capacitance. It is not consistent with the impedance of another multielectrode in section 2.1.3.2 and exceeds published values by a factor of ten. These high ranges were also measured with other microelectrodes and on different days (not presented here). Some differences might come from a different choice of the maximal voltage (0.7 V instead of 0.8 V for example) or using another sweep rate, leading to higher or lower capacitive currents. The exact geometry of the electrode (outer ring, Ir-layer thickness, roughness, length feedlines, passivation) is not inherent in the *relative* capacitance (see also section 2.1.3.3). The relative capacitance therefore acts more as a guidance level. Another explanation might be a damaged passivation layer, as it indicated by some SEM-pictures (section C.2). Stimulation on the same multielectrode (section 2.2) shows a huge crosstalk between the electrodes. This leads to an amplification of the affected surface in total and therefore to a higher capacitance. It was not the task of this thesis to study the electrochemical degradation effects of Iridium oxide. For this purpose, a far higher quantity of new microelectrodes would have been necessary. In general, the electrochemical properties of the electrode are changing each time when cyclic voltammetry is done. Producing IrOx-electrodes, Koch [40] claimed in his phd-thesis for the first production charges a complete destruction of the IrOx in the first few hours of stimulation, strong degeneration effects on all electrodes and short cuts of the feedlines. In the simulation part this fact will be provided by a large variation of parameters especially of the capacitance.

What can be seen in Fig. 2.9 is that the current is increasing exponentially when the voltage reaches maximal or minimal values. These exponential "tails" can be found in literature more pronounced [53] [34] [40].

2.1.3.3 Electrode Surface Roughness

Fig. 2.10 shows the typical surface of a microelectrode, which has been used

- just in PBS or pure water (MilliQ TM)
- all time under voltage controlled stimulation ($|U| < 0.8 \text{ V}$)
- less than 20 hours of usage in total
- with various stimulation frequencies

The surface of a brand-new microelectrode is much smoother (Fig. C.3). SEM pictures of microelectrodes that have stimulated biological tissue have additionally large amounts of biological residues ¹. A finite element simulation (chapter 4) is not able to simulate this roughness in detail. Neither is it possible to measure

¹As seen on SEM-pictures of J. Brusius, ICS-8 FZ Juelich

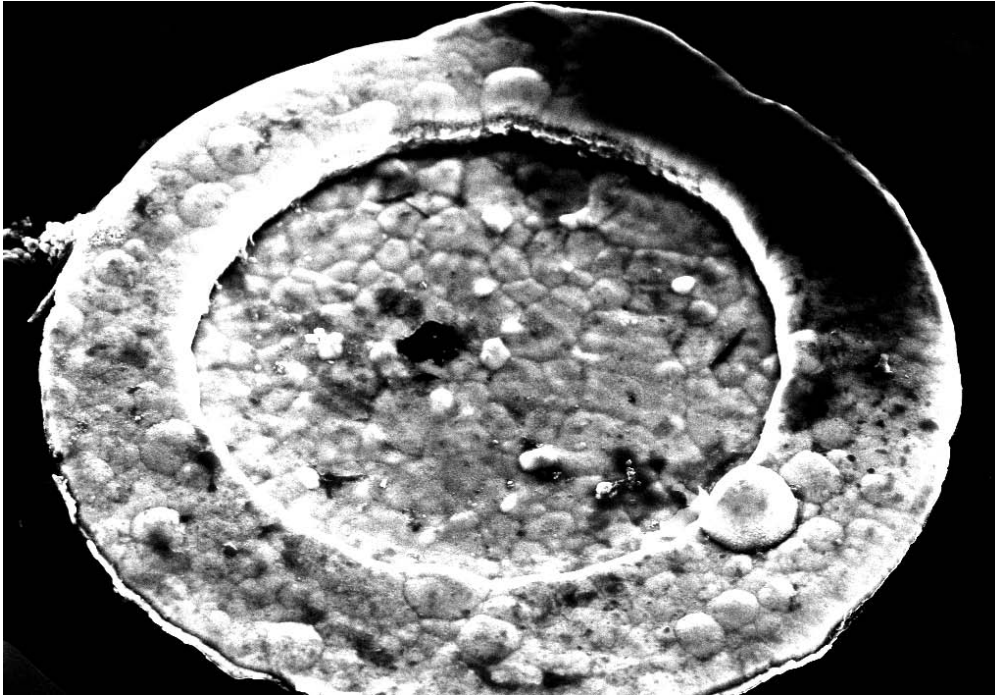


Figure 2.10: SEM-picture of one out of 16 electrodes of the multielectrode 13710

these "bubbles" and depressions in an acceptable time, nor is there a possibility to predict the evolution of new structures in detail. Systematic investigations on the degeneration behaviour of IrOx layers for microelectrodes depending on stimulation protocols are not known to the author. An empirical approach to take degeneration into account, is the *roughness factor* which describes the ratio of *real area* to *geometric area* [1]. In this way, the idea of a capacitance per area is maintained, because the difference of expected to measured capacitance is put into a factor.

2.1.4 Setup in the Faraday Cage

For these experiments a new Faraday cage was built, which consists mainly of a solid ground plate made of steel (~ 15 mm thick) with a grid of screw holes (for metric screws M6 (DIN 13-1)) and thinner aluminium plates at the sides, fixed by a steel frame. The grounding and the power supply of the whole system come from an additionally-shielded cable from outside the room. The front side of the cage is protected from noise by flexible iron curtains (*alphamesh*, proMesh, Mühlacker - Germany), which enables an easy handling.

EXPERIMENT

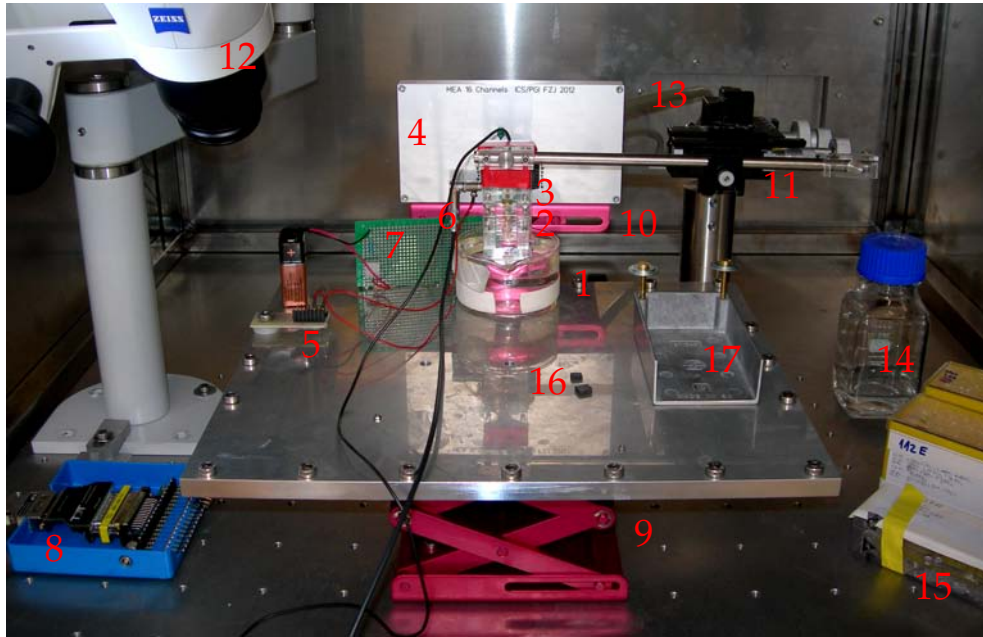


Figure 2.11: experimental setup inside the faraday cage (in general)

In a beaker (250 ml, VWR International GmbH, Darmstadt Germany) filled with PBS (section 1.2.2), both the stimulating MEA 2 and the recording MEA 3 (behind) are arranged. The transparent beaker allows to control, whether the electrode tips are in contact with the medium while keeping the feedlines outside of the solution. Additional heating could be installed directly under the beaker (not shown). The recording electrode is connected to the 16 channel headstage 4 (section 2.1.2) with a Dual In-line (DIL) socket (hidden). The reference potential both for stimulation and recording is provided by an Ag/AgCl pellet in the medium (E206, In Vivo Metric, Healdsburg, California) and distributed by a small socket 5. In some stimulation settings, a connector 6 to an external stimulation source is needed. The second, external MEA 2 can be connected with additional cables and a switching platform 8 (Lemo to Omnetics connector, switchable for each of 16 channels), which can be operated with two different stimulation functions. To illuminate the inter-electrode-space an additional LED 7 was applied. With two lab jacks (Swiss boy) 9, 10 the headstage's and the multielectrodes' height could be adjusted. To fine-adjust the position of the stimulating electrode in relation to the recording electrode, a xyz-table (precision in the mm-range) 11 was fixed to the ground plate. 13 shows power supply and data cable heading for the main amplifier and 14 a bottle for PBS refill. Additionally, a microscope 12 (*Stemi 2000*, Carl Zeiss AG Oberkochen-Germany), different multielectrodes in their storage boxes 15 (Fig. 2.5), jumpers of two different kinds used at the headstage 16 and an additional electrical shielding 17 for the DIL-socket at the headstage can be seen.

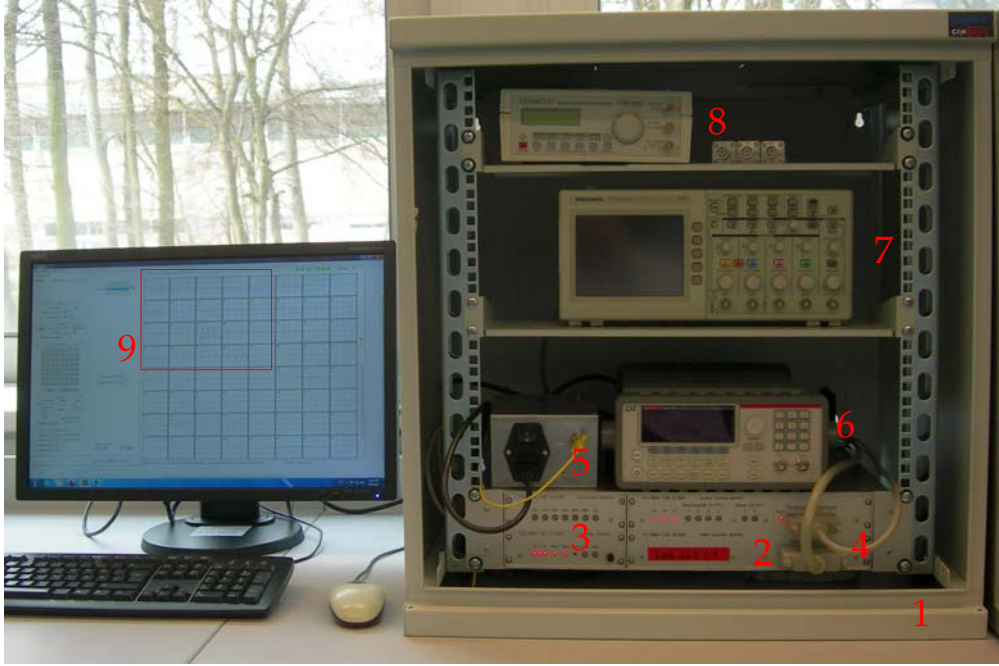


Figure 2.12: rack with mainamplifier, function generators and oscillograph used in the experiments, on the left side monitor the recording and stimulation software [B.1](#)

2.1.5 Rack

A small rack (1 in Fig. 2.12, 19" ,9HE, LogiLink, Canovate, Istanbul-Turkey) contains the main-amplifier 2 (section 2.1.1) and its power supply 5 (additionally grounded). The way of the stimulation (3: female connectors) and recording cables 4 is strictly separated. In preliminary experiments the phase of one function generator 6 could be adapted to the second one 8, which was observed with the oscillograph (7) (Tektronix GmbH, Köln-Germany). This enabled a bipolar stimulation, which was later also possible in a more convenient way (section 2.1.6). Furthermore the oscillograph was used for direct observation of the recorded and generated voltages. With further software improvements a 22 inch monitor (9) is necessary to keep track of all necessary parameters. 9 shows the 22-inch screen for the recording and stimulation software (section 2.1.6) with the graph of 16+2 recording channels (framed, see Fig. [B.1](#)).

2.1.6 Software

The software for data acquisition and stimulation is written in LabVIEW (National Instruments, Austin Texas) and is under constant development. Most of the recordings presented in this thesis were done with version MEA 2.2.5, which can be divided into different recording and stimulation modules.

In this section, just a short description of the software developments for this thesis is given. See appendix B for an extensive description of the recording software and more details of the stimulation modules.

2.1.6.1 Developments in Stimulation Control

Besides the possibility to use a function generator or the combination of both, there are also different ways to stimulate software controlled. A mode for stimulation using just one function and sine, triangular and rectangular wave forms was already existing (*Stim 1* in B.2). The shape of the rectangular wave forms could be specified in detail when using *Rect Stim* B.2. Furthermore, three major developments were made with the author's ideas and testing (besides smaller improvements):

Dual pulse stimulation In a graphical user interface two stimulation functions can be selected. Since the functions are presented both separated and in one graph, a precise phase difference is easy to adjust. Rectangular, triangular and sinusoidal functions with arbitrary parameters are available. When stimulating, the functions are applied at two LEMO-Adapters (LÉon MOuttet) at the front panel of the main amplifier.

Arbitrary pulse A modus was developed which enables the user to stimulate with arbitrary pulse forms at his own discretion. This was done in anticipation of future stimulation pulse forms (section 1.3.3.2) for the various fields of electrostimulation.

Stimulation series For selected 20 frequencies the "Stim series module" stimulates, measures and saves automatically. Arbitrary amplitudes up to 4 V and standard stimulation functions (sine, triangular, rectangular) can be used. This feature is used widely in the experiments (sections 2.2 and 2.3), since it enables to measure in a defined (same length) and very fast way¹.

2.2 Stimulation and Recording on the same MEA

In the following experiments one electrode out of the 16 of the four shank type multielectrode (Fig. 2.3) was used to stimulate, while the others were in detecting mode. The stimulation function is a constant sine, while the amplitude, frequency, and the stimulating electrode are varied. Here and in the next section (2.3) it was utilized that $\frac{1}{2\pi} \int_0^{2\pi} \sin^2(x) dx = \frac{1}{2}$, so that the amplitude of a signal was not just taken as the maximum or the minimum of a data string (sensitive to artefacts),

¹To give a number: A stimulation function set on every of the 16 electrodes for 20 frequencies results in 320 single experiments, not even varying other parameters.

but all data points are considered in the out-coming value. The stimulation signal was taken from an output port of the main-amplifier (Fig. 2.12) and connected to a potential divider, so that two cable ends were formed. One end (with no voltage losses) was put into a recording port at the backside of the main-amplifier, where it was recorded and saved. This was to get a close control over the stimulation pulse with a good voltage recording resolution. The other part of the applied voltage (10.06 %) is connected to the pre-amplifier (Fig. 2.11).

Already here, it should be stated, that the signals recorded here follow mainly from cross talk within the MEA and its feedlines.

2.2.1 Preliminary Tests

To test the crosstalk of the system, the microelectrode and its adapter (Fig. 2.1.3.1) were replaced by ohmic resistances in the same range ($\sim 1\text{ M}\Omega$), the resulting signal could hardly be seen and was at background-noise level. Especially the dimension of the signal was verified (bearing in mind the different amplifications and the discrepancy to the signal expected): On consecutive days the experiment was done with just one frequency and stimulation amplitude in the morning and in the afternoon, where the MEA was pulled in and out of the solution to get an overview of the variances of the values. This resulted in immersing the microelectrodes in PBS for half-an-hour before measuring.

2.2.2 Results

2.2.2.1 Frequency Dependence

With the *stim series* option (section 2.1.6.1) channel (ch.) 1 was stimulating. This single experiment was repeated ten times directly after another, to calculate the mean values of the amplitudes and the sample variance. It is worth noting, that no changes were made in or between the single experiments. It stands to reason, that this variance gets even increased, when the multielectrode has to be pulled out of the bath solution or has to be disconnected from the socket (section 2.1.4).

The recording feedlines of the stimulating ch. 1 are grounded to prevent any crosstalk in the headstage and main amplifier system. Its recorded amplitude represents therefore only the noise level and is superimposed by the other graphs. The biggest signal is seen on channel 9 and 17, which are both in the geometrical order and also at the DIL-socket-order near to ch. 1. Here up to 12% of the applied amplitude are detected, with high variances from experiment to experiment. It is decreasing with the stimulation frequency, what is in contradiction to both the impedance spectroscopy (section 2.1.3.2) and stimulation with a second MEA

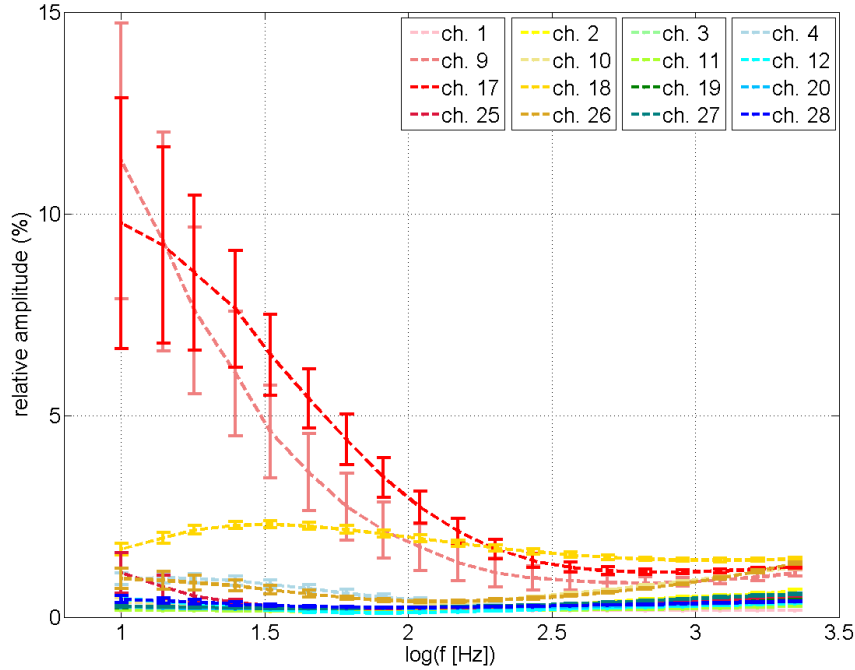


Figure 2.13: amplitudes measured with MEA 112E when stimulating on channel 1 using a sine with 100 mVpp (*Relative amplitude*: ratio of recorded to stimulated signal.)

(section 2.3). The maximum seen on ch. 2 and the minimum on ch. 26 are in sharp contrast to the strictly monotonic decreasing electrode impedance seen in experiment and simulation (section 3.2.1).

2.2.2.2 Amplitude Dependence

To study the stimulation amplitude dependence, the recorded signal of ch. 17 is presented. It is chosen because of its high amplitude to investigate the extremes of crosstalk within a MEA. The shown amplitude dependence is found in other channels' data as well.

If there was a linear correlation of the applied and recorded amplitude, the distances between two graphs would be more or less constant. Instead higher stimulation amplitudes have an influence on the recording system, which is clearly less than linear. The relative amplitude of 45 % on ch. 17 for a stimulation of 100 mV and 10 Hz is much greater than the amplitude in the previous experiment (45 %). This also demonstrates that the variance is high, when not taking data from experiments directly after another. For the next graphs another way of presentation the results is chosen: The data of the channels with the three greatest amplitudes are plotted

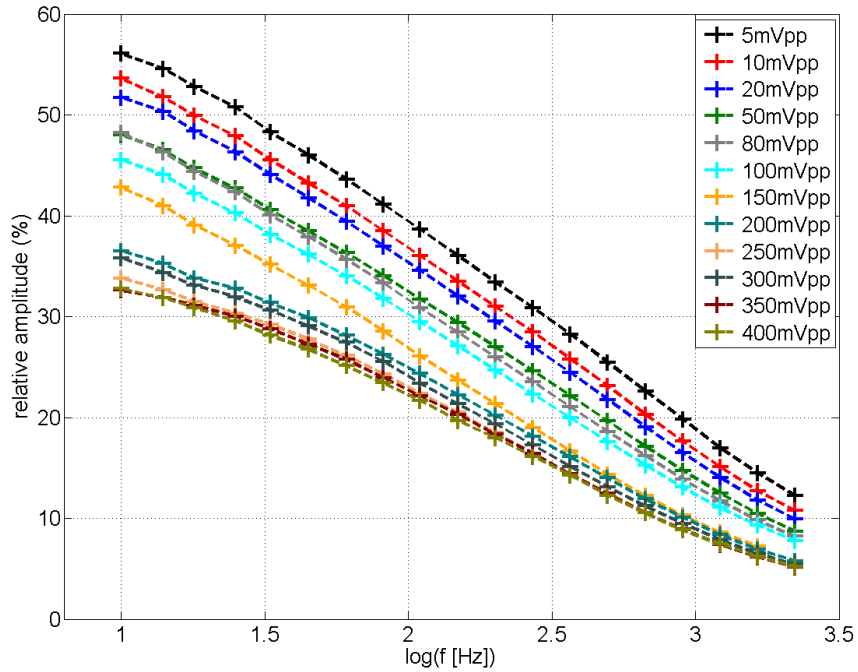


Figure 2.14: relative amplitudes measured on channel 17 for different stimulation amplitudes

against different stimulation amplitudes. In a case of a proportional relation a

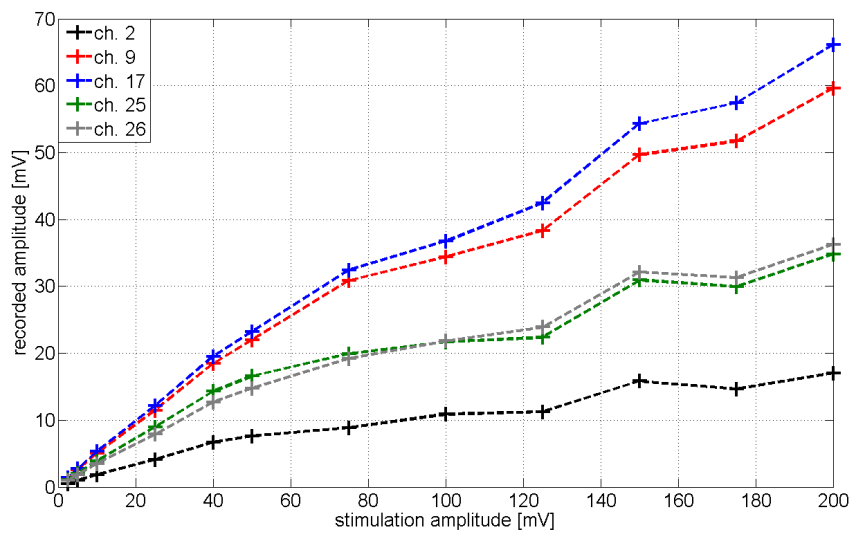


Figure 2.15: absolute amplitudes measured on different channels for different stimulation amplitudes for a sinusoidal stimulation on channel 1 with 10 Hz

straight line would be seen, which is not the case.

2.2.2.3 Stimulation Channel Dependence

A stimulation frequency of 10 Hz and an amplitude of 100 mVpp are chosen and the relative amplitudes are plotted in a matrix form. As seen in sections 2.2.2.1 and 2.2.2.2, high values can be expected using these parameters. For better visualization the data is also represented in colors: the lower the relative amplitude, the weaker is the color intensity. Section 2.2.2.1 demonstrates, that the absolute amplitude differences are at the maximum for this frequency and are decreasing almost exponentially, but the graphs are not crossing each other: The relative ranking remains constant.

When the relative amplitudes are plotted in a matrix, which represents the geometry of the used multielectrode (Fig. 2.3) with vertical entries representing data of one shank (the lowest row representing the electrodes at the very tip) there is a congruence just for a rare number of pictures (just eight pictures are presented in Fig. 2.16 and 2.18 as an example).



(a) ch.1



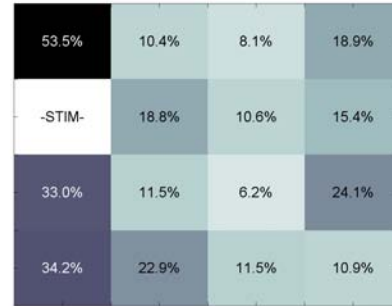
(b) ch.2

Figure 2.16: relative amplitude of different channels in an geometrical order for different electrodes stimulating with 10 Hz and 100 mVpp

Stimulation and Recording on the same MEA



(a) ch.4



(b) ch.9



(c) ch.10



(d) ch.11



(e) ch.25



(f) ch.27

Figure 2.17: relative amplitude of different channels in an geometrical order for different electrodes stimulating with 10 Hz and 100 mVpp

EXPERIMENT

In this selection (Fig. 2.16, Fig. 2.18) just stimulations on ch.1, ch.3, ch.4, ch.9 and ch.25 result in higher values for the electrodes on the same shank than on other electrodes. If ch.2 and ch.27 are set on stimulation mode, 55.4% and the 42.9% do not follow this theory. This is due to the fact, that ch.18 and ch.20 have switched positions in the geometrical settings of the Omnetics Adapter (Fig. 2.1.3.1). Besides that, in almost all cases a clear bisection in the relative amplitudes can be declared, with high probability of higher values for electrodes lying on the same shank. Another regularity is seen when looking on the feedline distances (Fig. 2.3). To take the fourth (far right) shank as an example: The feedlines of channel 12 and 28 have an especially close distance from each other. This can be seen as a correlation when stimulating on ch.12 at the value of ch.28 and vice versa:

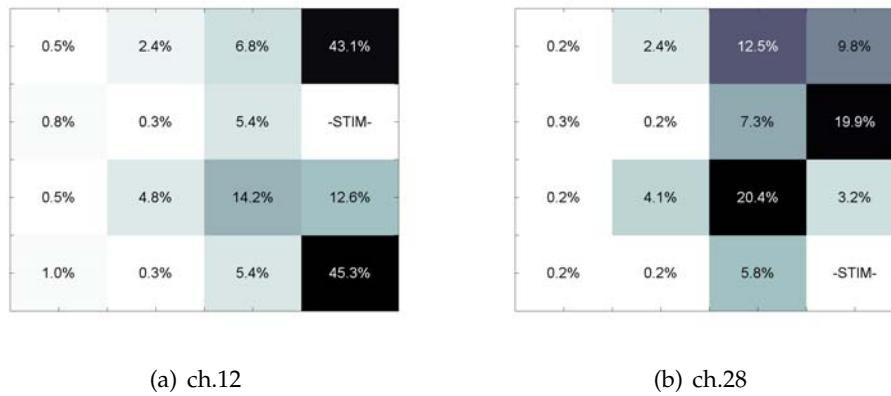


Figure 2.18: relative amplitude of different channels in an geometrical order for different electrodes stimulating with 10 Hz and 100 mVpp

The channel in the middle of ch.12 and ch.28 has a lower amplitude (12.5%), though its geometrical position is close to the stimulation channel. This behaviour can be found on all shanks (first shank a bit less) in 8 out of 8 cases. The procedure can be repeated, with the first and the third electrode of a shank. This time, shank three was taken as example, since the effect is superposed (but still visible) in the cases of ch.18 and ch.20, which form a geometrical exception (Fig. 2.1.3.1). On shank three ch.3 (ch.19) creates a stronger amplitude on ch.19 (ch.3) than on ch.11:

Stimulation and Recording on the same MEA

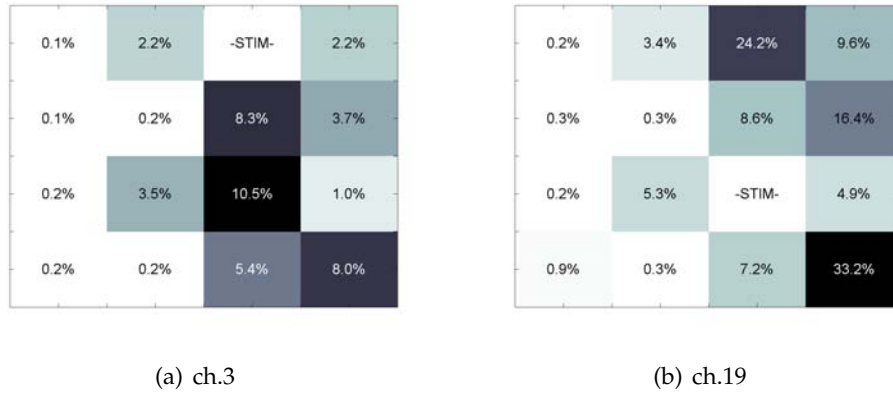


Figure 2.19: relative amplitude of different channels in an geometrical order for different electrodes stimulating with 10 Hz and 100 mVpp

Furthermore it was found out, that especially the electrodes at the tip (ch.25, - ch.26, ch.27, ch.28) where the feedline is passing all other the electrodes is creating a huge crosstalk (ch.28 is shown in Fig. 2.18, other shanks not shown here). This is further investigated in section 2.2.2.4. Since the level of crosstalk seems more to depend on the spatial distances of the feedlines than on the distances of the electrode surfaces, it is appropriate to arrange the results not in a geometrical order, but as they appear at the Omnetics Adapter and its pins. In Fig. 2.1.3.1, the two rows of pins are now represented by a 2×8 matrix; ground and reference are left out. A two-fold symmetry is also visible here, but a complete and exclusive reason for the values is not determined by the channel position of the Omnetics Adapter alone.

EXPERIMENT

-STIM-	6.6%
35.5%	4.6%
6.0%	10.7%
16.4%	1.2%
5.8%	3.5%
9.7%	0.9%
4.5%	1.7%
4.6%	1.1%

(a) ch.18

15.1%	43.0%
42.7%	19.7%
-STIM-	1.1%
82.2%	0.8%
59.6%	1.9%
47.1%	0.7%
24.9%	1.0%
16.2%	0.9%

(b) ch.27

12.7%	4.9%
43.2%	2.4%
5.4%	1.0%
-STIM-	0.3%
5.5%	0.9%
45.4%	0.3%
6.9%	0.6%
14.3%	0.5%

(c) ch.12

17.3%	15.2%
16.4%	16.7%
13.4%	25.1%
12.9%	66.3%
12.0%	34.8%
10.1%	-STIM-
8.9%	37.7%
5.8%	65.9%

(d) ch.26

1.0%	3.5%
2.3%	2.2%
5.4%	0.2%
3.8%	0.2%
8.4%	0.1%
8.1%	0.2%
-STIM-	0.2%
10.5%	0.2%

(e) ch.3

14.2%	8.7%
12.5%	8.2%
8.8%	16.8%
9.6%	15.5%
8.0%	30.0%
8.0%	18.2%
6.7%	-STIM-
5.5%	32.9%

(f) ch.1

4.9%	5.4%
9.7%	3.5%
7.2%	0.9%
16.4%	0.4%
8.6%	0.4%
33.2%	0.3%
24.2%	0.2%
-STIM-	0.3%

(g) ch.19

11.1%	7.4%
9.4%	7.9%
6.8%	13.6%
7.2%	23.1%
6.1%	18.1%
5.5%	28.1%
4.5%	23.1%
3.4%	-STIM-

(h) ch.17

Figure 2.20: relative amplitude of different channels in an order of the omnetics adapter for different electrodes stimulating with 10 Hz and 100 mVpp (first row)

2.2.2.4 Setting Channels to Ground

As demonstrated in Fig. 2.18, the signal of electrodes at the tip is strongly influenced by the stimulation of the upper electrodes. Is it possible to reduce this crosstalk by grounding the electrodes (and therefore the feedlines) in between? To answer this question, the first electrodes of the two right shanks (III and IV) were set to stimulation while electrodes in between were grounded one by one.

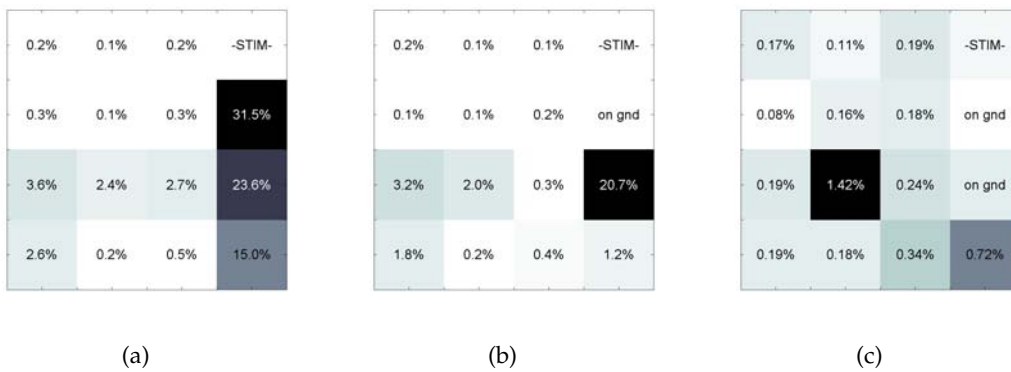


Figure 2.21: relative amplitude of different channels in an geometrical order for ch.4 stimulating with 10 Hz and 100 mVpp

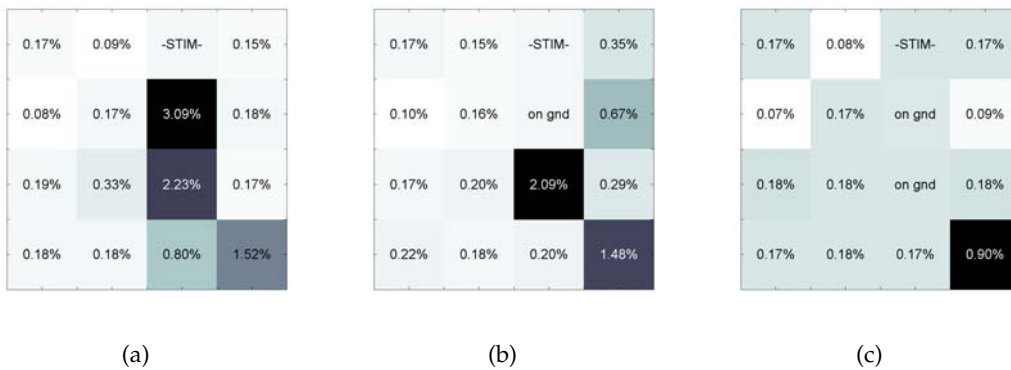


Figure 2.22: relative amplitude of different channels in an geometrical order for ch.3 stimulating with 10 Hz and 100 mVpp

The amplitude, which is recorded by the lowest electrode of the shank, decreases radically if the other electrodes are set to ground: In the first case the signal gets reduced from 15% to 1%, while on the third shank it decreases from 0.8% to 0.2%.

2.2.3 Discussion and Outlook for the Stimulation on the same MEA

The relative amplitudes were measured for a large spectrum of frequencies (section 2.2.2.1). In some cases, the effect of inner-shank-crosstalk reaches even values of 80 %. In general, the observed data is also typical for other multielectrodes. When varying the stimulation amplitude (section 2.2.2.2), there is no proportional relation of stimulation to the recorded amplitude. This amplitude behaviour is in contrast to experimental results when stimulating on another MEA (section 2.3.1.2) as well as with simulation results (section 3.6.2). A strong influence of the stimulation electrode position on the recorded signal of the remaining electrodes could be found (section 2.2.2.3). Especially high crosstalk exists if stimulating and recording electrode are on the same side of the Omnetics Adapter as well as on the same MEA shank. The influence of the latter can be reduced severely, by setting electrodes in between to ground (section 2.2.2.4). The same effect is expected when the grounded feedlines are not connected to electrodes and are just surrounding a stimulation electrode.

In summary, strong indications were found, that the recorded signal at the stimulating MEA has its source not in the propagation through the saline.

Concerning

- the spatial correlation
- the range of the amplitudes
- the frequency dependence

it is not what can be expected to be the stimulation signal. In particular the measured values on all electrodes are too high to see any signal of the expected range (another stimulating microelectrode (section 2.3) or biological signals). The variance of the collected data remains high. It might also be reconsidered, whether the crosstalk is limiting the geometrical resolution of microelectrodes in general, and especially when the electrodes are not sealed by biological tissue. For the future a procedure might be useful, which is investigating the crosstalk of an electrode by stimulating with amplitudes and frequencies in a large range (with a similar software as in section 2.1.6.1) and for all 16×15 combinations. Since the strength of the stimulated signals is depending on the stimulation frequency, a definition of physical/technical constants could be useful. If further investigations derive a kind of exponential dependence on the frequency this could be a constant ν with $amplitude \propto \exp(-\frac{f}{\nu})$. It might also be possible, that the ratio of the relative amplitudes, for example $\frac{rel.ampl.(ch9)}{rel.ampl.(ch17)}$ is more or less constant for all frequencies. In this case a ratio of 0.9 would indicate a strong, a ratio of 0.3 a weaker crosstalk. The amplitude dependence has to be further investigated also. If it can be described

by $rel.amplitude \propto (1 - \exp(-\frac{V}{V_0}))$ with V as the stimulation amplitude and V_0 a constant, the following procedure might be adequate: When the electrode rests in the neuronal tissue, a low stimulation amplitude is applied, so it is secured that neuronal tissue is not stimulated. The recorded crosstalk is extrapolated and subtracted from future data, which contains also spiking and other activities. Since a correlation of recorded amplitudes to the spatial distribution of the feed lines was found, great care has to be taken in designing future MEAs for stimulation **and** simultaneous recording purposes. It has to be asked, whether it is feasible to put the stimulation feedlines for example on the other side of the shank and -coming from the shank- separating them spatially very soon. Implementing additional grounding feedlines or plates with no contact to the bulk medium (not to influence the physical or biological system) might produce relief. By more direct channel assignments with fewer converters and adapters (from one and the same manufacturer) it would become easier to follow the signal way from the electrode geometry up the graphical display. In the future a model shall be developed to describe the measured crosstalk and to look for the best parameters for a low crosstalk.

2.3 Stimulation on a second MEA

In this section, the stimulation and recording is strictly separated (A small crosstalk was observed, when the plugs of the grounding wires were put too close together on the grounding socket, but this was far smaller than in section 2.2 and was not detected any more for an increased distance from each other.). A multielectrode of the four-shank-type (Fig. 2.3) is still recording, while the stimulation is transferred to a two-shank-type multielectrode (Fig. 2.4), which has electrodes of a higher diameter leading to a larger signal. In general, electrodes with larger surfaces are recommended for stimulation purposes¹. For all parts a sinusoidal stimulation was chosen. A possible temporal delay of the recording to the stimulation signal is not of particular interest in biomedical purposes. No pulse shape changing was observed, when applying pulses of a "normal" length (~ 1 ms) used in stimulation techniques (section 1.3.3). Since it is not possible in this setup to measure the current applied, the connection of current flow to the voltage pulse shape is done in the simulation part (chapter 3), where different pulse forms are investigated also.

2.3.1 Monopolar Stimulation

To increase the SNR and to get not too dependent on the electrochemical properties of one electrode, normally all stimulation channels are connected. The stimulation

¹product catalogue of Neuronexus: <http://www.neuronexustech.com/neuroscience-products>

series module (section 2.1.6.1) was considered to be a good tool to measure with equal recording times and directly one after another. This way, single data packages are comparable and a possible mismeasurement can be detected.

2.3.1.1 Frequency Dependence and Reproducibility

All channels of the stimulating multielectrode were set to a sine of 95 mVpp with frequencies ranging from 10 Hz to 3000 Hz. In this way a kind of impedance spectroscopy (section 2.1.3.2) was established, though not measuring the currents for an applied voltage, but the voltage dropping over an ohmic measurement resistance (see section 3.30). Because of this similarity, higher signals are expected for higher stimulation frequencies. The experiment was repeated ten times and the sample variance was calculated and plotted using errorbars.

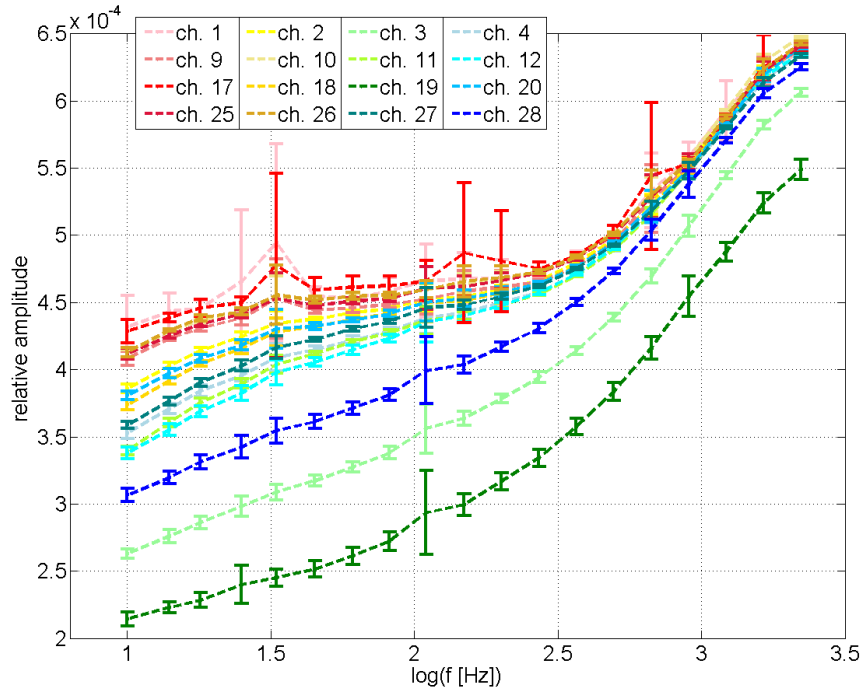


Figure 2.23: relative amplitudes (ratio of recorded to stimulated amplitude) measured on the multielectrode 112E for a sinusoidal stimulation with 95 mVpp and different frequencies

Fig. 2.23 shows, that the signal is increasing monotonically (almost an exponential increase) and the error bars are in a lower range. Thus they represent only the variances which occur when the experiments are done directly after another, especially without changing the electrode or disconnecting it from the DIL-socket (section 2.1.4 and 2.2). Some errorbars are exceptionally high. This comes from

gross errors, resulting in high peaks in the graph (the reason has not been cleared finally). Though this is not an double-logarithmically plot, it is in accordance with the Bode-plots of the impedance spectroscopy (section 2.1.3.2), where an exponential decrease of the impedance can also be seen. The amplitude range remains roughly in a shank-order: Highest amplitudes can be found at the electrodes of the first shank, followed by the second one, while signals of electrodes on the third and fourth shanks stay lower for all frequencies. From electrode to electrode, the measured signals differ up to a factor of 2 in low frequency ranges. Ch.28, ch.3 and ch.19 are recording particularly low amplitudes.

2.3.1.2 Amplitude Dependence

Is the recorded signal proportional to the stimulation? To answer this question, a sinusoidal stimulation was applied, varying the stimulus frequency and amplitude. For the next graph a frequency of $f = 110 \text{ Hz}$ is selected and the amplitudes of all channels is presented. For other frequencies, similar graphs could be presented.

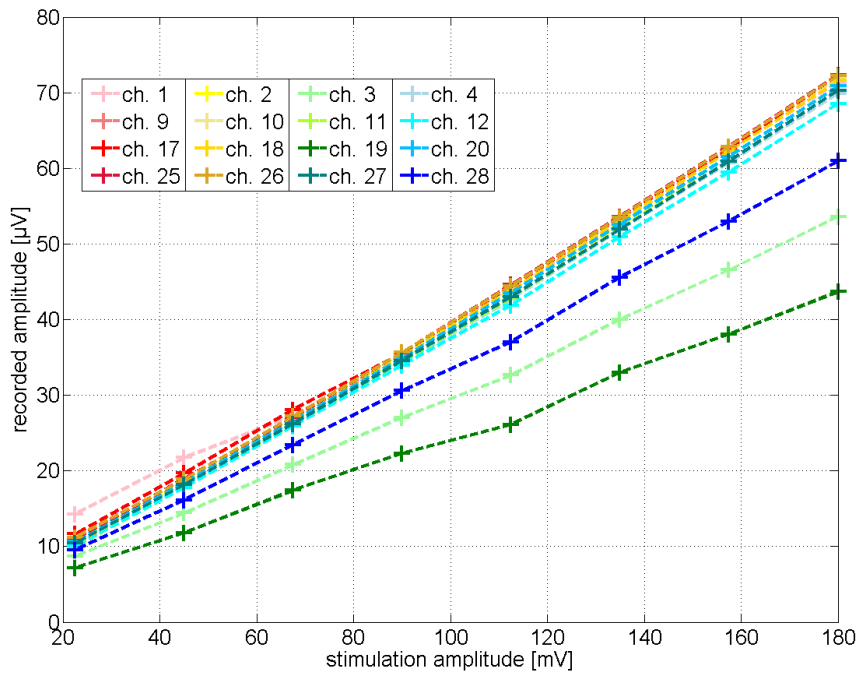


Figure 2.24: absolute amplitudes measured on the multielectrode 112E for a sinusoidal stimulation for various stimulus strengths and a frequency of $f = 110 \text{ Hz}$

A linear correlation between the stimulus and signal can be stated for nearly all channels. It therefore makes sense to take the relative amplitude as a parameter to

observe. On ch.28, ch.3 and ch.19 lower signals can be found again.

2.3.1.3 Dependence on the Number of Stimulating Channels

Again a stimulus of 95 mVpp was applied on a varying number of electrodes and the signal at the second MEA was recorded. All frequencies were measured, but for reasons of overview just $f = 126 \text{ Hz}$ is presented. Due to extremely sensitive automatic measurements, at many frequencies one or two values are non-physically high. Therefore the measurement for electrode 8 is not presented here. For other frequencies it has values as expected. Peaks can be observed at other frequencies, too .

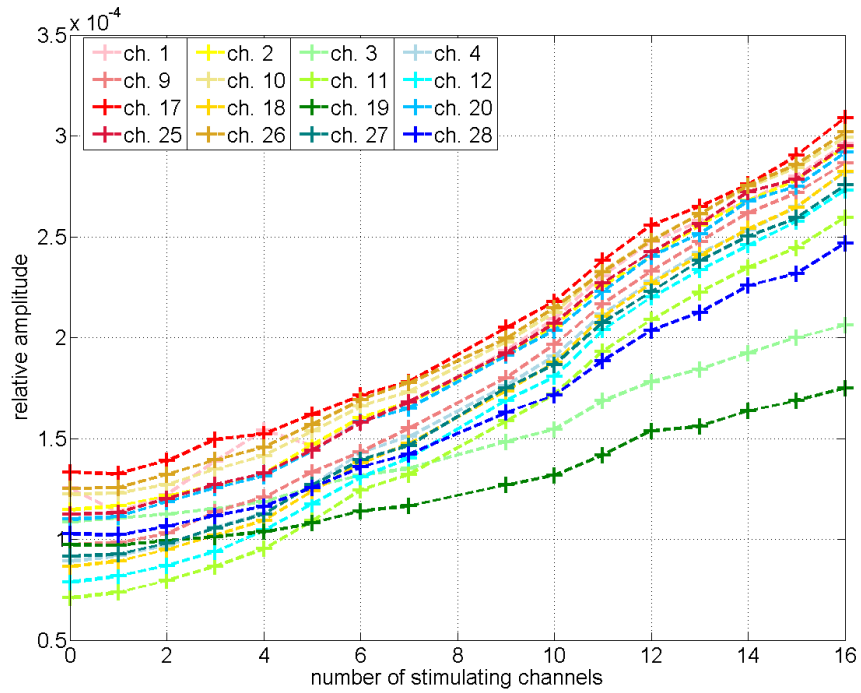


Figure 2.25: relative amplitudes measured on MEA 112E for a sinusoidal stimulation of $f = 126 \text{ Hz}$ and 95 mVpp varying the number of stimulating electrodes

“Zero channels stimulating” (very first) represents the level of noise. As expected, the signal level increases strictly and almost linear with the numbers of channels. When seen as a pure capacitor, the currents would go linear and with them also the voltage measured.

2.3.1.4 Spatial Dependence

Because of the electrode cages (see Fig. 2.5) the distance of stimulating to recording MEA can be minimized to only 15 mm. In this experiment the distance was varied up to 35 mm with a mm-screw in the setup (section 2.1.4) to investigate the spatial dependence. (In most of the experiments presented here the distance was around 20 mm.) A change of the lateral position was not done, so that the multielectrodes were facing each other, also with the same height. The stimulation was done with a sine using 180 mVpp and various frequencies. The data shown here was taken from channel 11. (On other channels some peaks are visible again.)

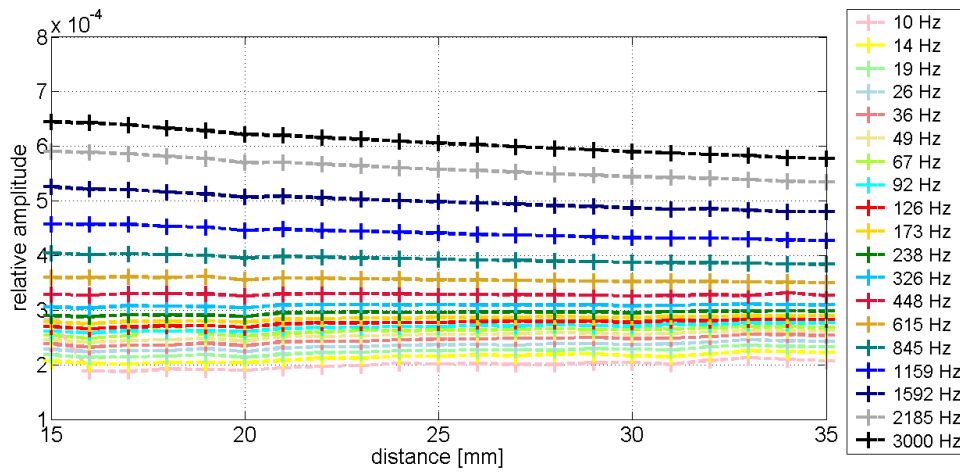


Figure 2.26: relative amplitudes at electrode 11 measured on the multielectrode 112E for a sinusoidal stimulation of 180 mVpp varying the stimulus frequency

The picture seems to be twofold: For low frequencies an increasing distance has almost no effect, while for higher frequencies ($f \geq 615$ Hz) the amplitude is clearly decreasing.

2.3.1.5 Dilution Series

To investigate the influence of the PBS concentration on the signal, the concentration was varied between pure water (MilliQ TM) and different concentrations of PBS. This was achieved by pipetting 500 μ l of a 10 \times PBS solution at a time into a pot with 60 ml water. The concentration in the graph is given in units of a 1 \times PBS solution. See section 1.2.2 for the recipe.

Up to a concentration of 0.3 PBS 1 \times there are extraordinary high amplitudes. For higher stimulation frequencies a maximum of the relative amplitude can be observed at ~ 1 PBS 1 \times .

EXPERIMENT

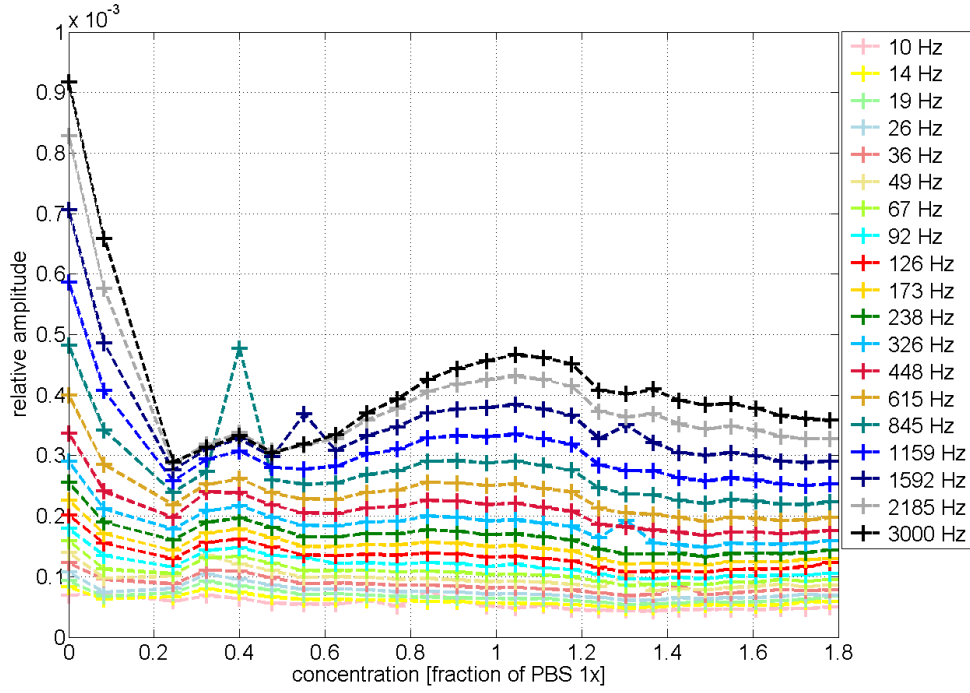


Figure 2.27: relative amplitudes at electrode 2 measured on the multielectrode 112E for a sinusoidal stimulation of 180 mVpp varying the stimulus frequency and the bulk concentration

2.3.2 Bipolar Stimulation

With the *dual pulse* module (Fig. B.2), two sine waves with 100 Hz and 100 mV were applied to two groups of 8 electrodes of a stimulating two-shank MEA (Fig. 2.4). The selection, which electrodes are stimulating to the first function, was taken arbitrarily. Indeed, the recording electrode's distance with $2 \times 10^4 \mu\text{m}$ is large in comparison to $2 \times 10^2 \mu\text{m}$ as the position differences of the electrodes. While all other parameters were held constant, the phase difference of the two stimulation functions was varied from 0° to 360° . Because of technical reasons it was just possible to stimulate for 450 ms with a 50 ms delay afterwards. The error this may have caused is systematic and is not depending on the phase difference. A minimum can be observed at approximately 180° and two maxima with the same height at 0° and 360° respectively. The signal amplitude of ch.19 remains low, what is apparent when looking at phase differences of 0° and 360° .

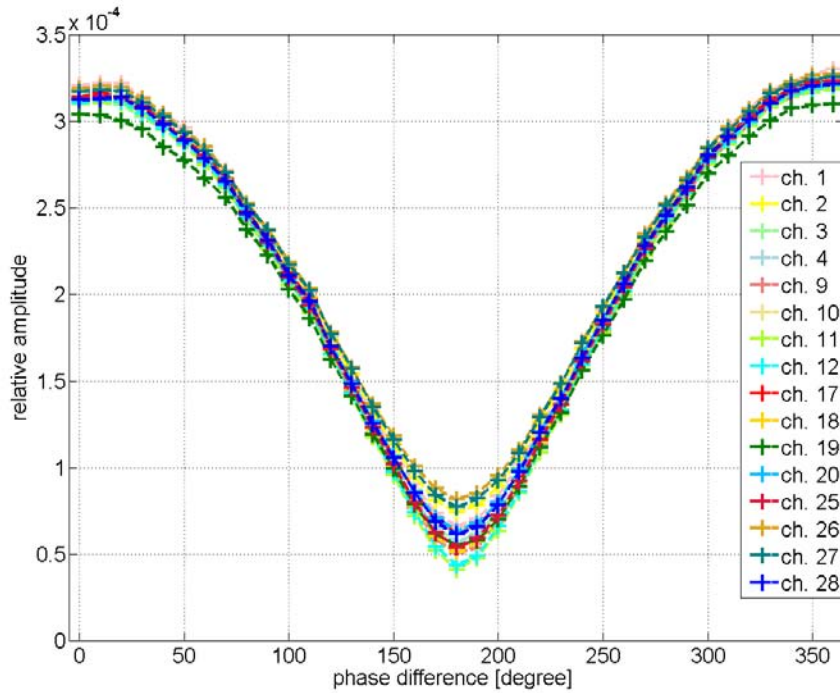


Figure 2.28: relative amplitudes measured on the multielectrode 112E for a bipolar sinusoidal stimulation of 200 mVpp for a frequency of $f = 100$ Hz varying the phase delay of half of the stimulating electrodes

2.3.3 Discussion and Outlook for the Stimulation on a second MEA

Stimulating with an additional MEA, the relative amplitudes observed drop remarkably from the range of $10^{-1}/10^{-2}$ to 5×10^{-4} (section 2.3.1.1). Due to a sensitive measurement system, it was possible to stimulate just with a few hundred millivolts leading to signals in the tens of microvolt range not far away from the noise level. Stimulation of neuronal tissue has to take place in the vicinity of the electrode also with higher stimulation amplitudes, which are most probably changing the electrode characteristics within seconds. As expected, larger signals could be detected for higher stimulation frequencies as well as for an increasing number of stimulating electrodes (section 2.3.1.3). Here, a few high peaks were measured which contrast with the continuous graph. The cause might be a measurement before the system is relaxed and some voltage peaks occur due to an unbalanced stimulation process. Another reason may be a drift of the voltage during recording. A prolonged measurement duration is diminishing the outliers. There is a linear correlation of stimulation and recorded amplitude (section 2.3.1.2). The spatial dependence is visible for higher frequencies only (section 2.3.1.4). An explanation for this behaviour might be the high impedances of the stimulation and recording

electrode for lower frequencies, so that the increasing resistances caused by greater distances have a smaller (or almost no) effect. (A very little increase is seen for lower frequencies, but is far smaller than the sample variance of the experiment.) In section 3.6.4 the graph is further interpreted with respect to a resistor and capacitor model. A stimulation in an aqueous solution with nearly no ions resulted in high recording amplitudes (section 2.3.1.5). This was probably caused by a lack of electrical charges, which are able to ground the recording electrode. Since both, the impedance of the electrode and of the saline should increase with higher ion concentrations (section 3.6.5), an explanation for the maximum of the amplitude at PBS1× has not been found yet. For a combination of two stimulation functions (section 2.3.2) constructive and destructive interference effects occur. In the latter case, the amplitude is limited by noise. Bearing the experimental results in mind (section 2.2) one can estimate that much of the interference is occurring within the feedlines already and the smaller part in the bulk solution. Taking the propagation time of a stimulus to a certain part of biological tissue into account, a focussing of a stimulus might be achieved by a bipolar stimulation. The variance of different electrode signals is far smaller here than in previous experiments (section 2.3). This might come from a longer recording time (10s instead of 2s) or from the 50 ms breaks in between of the stimulation pulses. For an investigation of an interference effect it might be useful to stimulate with two different microelectrodes, to prevent interference caused by crosstalk taking place already in the feedlines instead of the bulk solution. So that in total three microelectrodes and one reference electrode would be in the bath.

In general, the relative variances are smaller than in the case when recording and stimulation takes place on the same MEA.

2.4 Summary and Discussion of the Experimental Part

For investigating the behaviour of stimulating microelectrodes targeting neuronal tissue a new setup was established. It consists of a faraday cage, mainamplifier and a custom-designed preamplifier. For the software useful improvements were initiated, which already came into operation. The microelectrodes are commercially available and were characterised using cyclic voltammetry, impedance spectroscopy and electron microscopy. The main differences when stimulating on the same or on an additional microelectrode are displayed in a Table 2.2. Since these differences are so massive in nearly all parameters characterising a sinusoidal stimulation, this leads to the conclusion not to record a signal coming through the saline when stimulating on the same multielectrode. This means that different electrodes are needed when simultaneous stimulation and recording is demanded. The spatial

Table 2.2: difference between the signals of stimulating on the same or on a second MEA

category	stim. on same multielectrode	stim. on second multielectrode
dimension of relative signal	0.2% – 80%	$\leq 0.07\%$
behaviour when increasing frequency	decreasing	increasing
amplitude dependence	flattening for higher amplitudes	proportional
reproducibility	high variance (especially at low frequencies)	low variance
stimulating ch. dependence	high, depends on feedline position also	just on the number of stim. electrodes
recording ch. dependence	very high (differences of a factor of 100×)	lower (2×)

separation as well as the implementation of shielding of the stimulation feedlines by extra grounding parts may be a first step. In case, there is no cell on the electrode that is increasing the seal resistance, a fine spatial resolution is undermined by crosstalk effects. When doing analysis on these data, algorithms should be used to improve the resolution and to consider the electrochemical differences of each electrode. Furthermore, systematic and extensive investigations on the degeneration behaviour for a special, but widely used type of MEAs seem useful to clear the limits of frequency and amplitude when developing new stimulation pulse forms.

EXPERIMENT

Chapter 3

Simulations based on an Equivalent Circuit Model

The sections of this chapter can be separated into two parts. In the first part, three models are presented, which are used to describe the electrical properties of a microelectrode. For every model the influence of its specific electrode parameters is investigated. Reliable relations of voltage to current and vice versa are aimed. For an experiment, either a current or a voltage controlled system is used. One parameter is determined, but the other one is frequently not even measured (as in the case of chapter 2). For current controlled stimulation high voltages might occur, where electrolysis takes place or the electrode surface gets damage. In the case of voltage controlled stimulation, high currents are damaging neuronal tissue [1], while current controlled stimulation is able to built up voltages high enough to let to multiple reactions occur, including gassing (see Table 1.1). In the second part (section 3.6) only a R(RC)-model is used to describe experimental results, when a second multielectrode array (MEA) is used for stimulation. Here, also some parameters of the two MEAs are varied and effects on the signal are observed, as it appears at the main amplifier and is recorded. The influence of two parameters is investigated in detail: The capacitance of the recording or the stimulation electrode is varied, since in literature it is dealt as a key parameter for safe stimulations. The second parameter is the stimulation frequency. As mentioned in the introduction (chapter 1), stimulation pulse forms and frequencies are an ongoing topic of active research. The range of stimulation is not less than from 10 Hz to 10^4 Hz. This results in utmost different voltage drops or current flows at the very same surface.

3.1 Fundamentals

According to capacitive effects (section 1.3.3.4) and faradaic currents (section 1.3.3.5), it is not surprising that the electrode/electrolyte-surface shows qualities both of a capacitor and an (ohmic) resistor. Equivalent circuit models are therefore widely used [54] [55] [1] (Already in 1924, Otto Stern named the double layer a “molecular capacitor” [32]), especially if the dimensions of currents and voltage drops at the surface are more of interest than the spatial propagation of the stimulus. On the plus side of an equivalent circuit simulation stands, that it is quick, an empiric approach and effects on parameters like the electrode impedance can be varied in an arbitrary manner. On the minus side is clearly the fact, that all molecular processes cannot be described properly and have to be implemented by indirect parameters. Simulations using an equivalent-circuit model are done with MATLAB Simulink (mathworks, Natick, MA-USA). This is a graphical programming environment and combines the potential and effectiveness of MATLAB with the flexibility of a graphical user interface (this was especially useful for preliminary test, when models had to be adapted very quickly). Special benefit comes from the implementation of self-written MATLAB functions in the electrical circuitry simulation (see sections 3.3 and 3.4).

The common ohmic law $\vec{j} = \underline{\underline{\sigma}} \vec{E}$ links the current density \vec{j} with the electrical field \vec{E} by the conductance tensor $\underline{\underline{\sigma}}$. In an electric circuit it reduces to

$$i = \frac{1}{R} U = \frac{1}{R} \frac{d^0 U}{dt^0} \quad (3.1)$$

with the total current i , the resistance R and the potential difference U . On the other hand, the solution of Poisson’s equation (eq. 1.4) for an ideal capacitor $C = \frac{Q}{U}$ defining the capacitance C as the ratio of electrical charge Q to potential drop U can be differentiated to

$$i = C \frac{dU}{dt} = C \frac{d^1 U}{dt^1} \quad (3.2)$$

Also the law of an inductor $U = L \frac{di}{dt}$ with the inductance L can be written in a similar form:

$$i = \frac{1}{L} \int U dt = \frac{1}{L} \frac{d^{-1} U}{dt^{-1}} \quad (3.3)$$

A Constant Phase Element (CPE) can be considered as the generalisation of all these cases using

$$i = Y_n \frac{d^n U}{dt^n}, \quad -1 \leq n \leq 1 \quad (3.4)$$

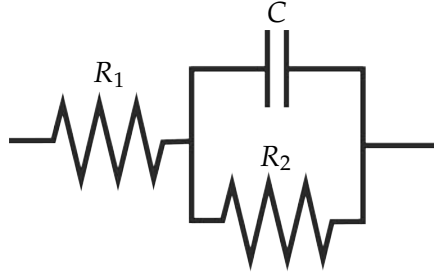
The constant Y_n has also the parameter n , since its dimension depends on n . To use this definition, the fractional order calculus is necessary as it is described in the mathematical methods in the appendix (sections A.1 and A.2). If $n = 0.5$ the CPE is also named Warburg element [56].

Table 3.1: Similarities in the description of different electrical elements

element	n	$i(U) =$	Z	$\theta(i) - \theta(U) =$
Inductor	-1	$\frac{1}{L} \int U dt = \frac{1}{L} \frac{d^{-1}U}{dt^{-1}}$	$L\omega e^{i\frac{\pi}{2}}$	$-\frac{\pi}{2}$
Ohmic resistor	0	$\frac{1}{R} U = Y_0 \frac{d^0 U}{dt^0}$	R	0
CPE	$\in (-1, 1) \setminus 0$	$Y_n \frac{d^n U}{dt^n}$	$\left(Y_0 \omega^n e^{\frac{\pi n}{2} i}\right)^{-1}$	$\frac{\pi n}{2}$
Warburg Element	0.5	$Y_{0.5} \frac{d^{0.5} U}{dt^{0.5}}$	$\left(Y_{0.5} \sqrt{\omega} e^{\frac{\pi}{4} i}\right)^{-1}$	$\frac{\pi}{4}$
Ideal capacitor	1	$C \frac{dU}{dt} = Y_1 \frac{d^1 U}{dt^1}$	$(C \omega i)^{-1}$	$\frac{\pi}{2}$

Z means the impedance and $\theta(U)$ and $\theta(I)$ the phase of the applied voltage and the current, respectively. To prevent confusion, the term “CPE” is used in this thesis just in the case $n \in (-1, 1) \setminus 0$ (zero excluded). Of particular interest is the case $n \lesssim 1$.

3.2 R(RC)-Circuit Model of a Microelectrode



$$I_{R_1} = \frac{1}{R_1} U_{R_1} - \text{bulk resistance}$$

$$I_C = C \frac{d}{dt} U_{R_2, C} - \text{capacitive fraction}$$

$$I_{R_2} = \frac{1}{R_2} U_{R_2, C} - \text{faradaic fraction}$$

3.2.1 Simulating Impedance Spectroscopy Data

The absolute value of the total impedance of an R(RC)-circuit can be derived analytically using Table 3.1:

$$\begin{aligned} |Z_{tot}| &= \left| R_1 + \left(\frac{1}{R_2} + i(2\pi f) C \right)^{-1} \right| \\ &= \sqrt{\left(R_1 + \frac{R_2^{-1}}{R_2^{-2} + (2\pi f C)^2} \right)^2 + \left(\frac{2\pi f C}{R_2^{-2} + (2\pi f C)^2} \right)^2} \end{aligned} \quad (3.5)$$

The parameter R_1 represents the saline resistance. R_2 for the faradaic and C for the capacitive currents have been fitted to the mean values of the impedance spectroscopy plot presented in section 2.1.3.2. After the fitting, experimental values and the fitted function are plotted logarithmically (Fig. 3.1). The errorbars in the red graph stand for the sample variance of the 16 observed electrodes.

The results of the fitting are

$C = 1.02 \pm 0.59 \text{ nC}$ $R_1 = 50 \text{ k}\Omega \text{ [fixed]}$ $R_2 = 8.89 \pm 2.26 \text{ M}\Omega$

[fixed] refers to the fact, that the resistance in parallel was not fitted numerically, but a guess of the impedance spectroscopy software proved to be reliable. In figure 3.2 R_1 is varied also. Taking the area of the electrode ($177 \mu\text{m}^2$) into account, leads to a relative capacitance of $580 \frac{\mu\text{C}}{\text{cm}^2}$, which is in accordance with literature (Table 2.1). Since the parameters have a range of $C = 10^{-9} \text{ F}$ and $R_1 = 10^6 \Omega$ (in strong contrast to Non-Micro-Electrodes and other systems which can be described by this equivalent-circuit-model), the fitting is numerically difficult and relies on precise starting points (even when fitting just the exponents). How does each fitting parameter influence the graph of the impedance spectroscopy? In the next three figures (3.2, 3.3, 3.4) one fitting parameter is varied, while the two others are

R(RC)-Circuit Model of a Microelectrode

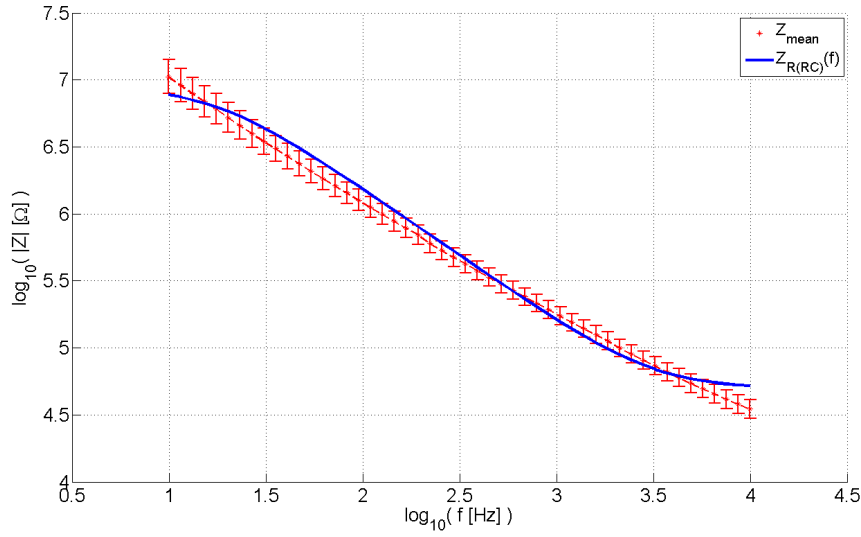


Figure 3.1: impedance spectroscopy: The experimental data presented in Fig. 2.8 is plotted in red (Z_{mean}) and was fitted by using a R(RC)-model ($Z_{R(RC)}(f)$).

fixed to the values of the fitting shown above. In each case, the red curve represents the original (fitted) value of the varied parameter. R_1 acts here as an offset,

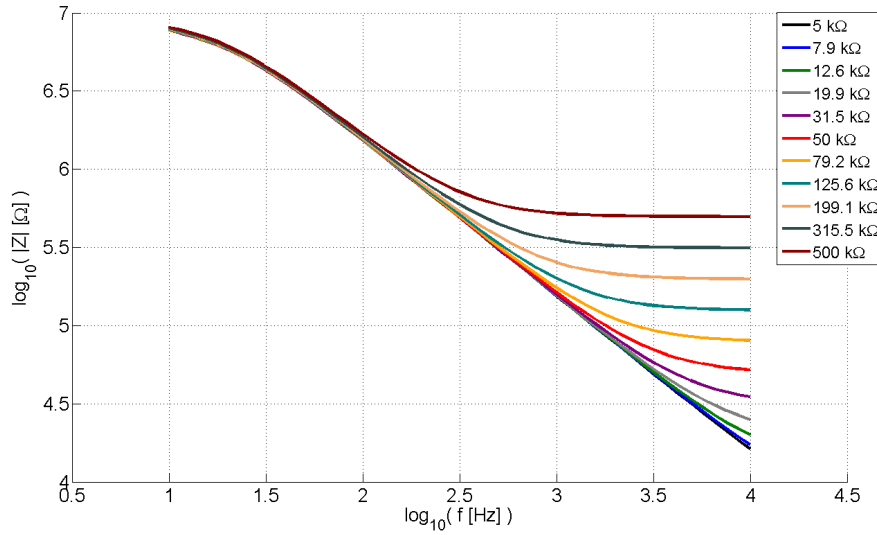


Figure 3.2: influence of R_1 on the impedance of a R(RC)-model

which is also apparent as the resistance is placed before the system of the second resistance and parallel capacitor. In other words: The low capacitor-impedance leads to a short-circuit of the (R_2C) -system, so that R_1 is the only resistance left. R_1 can therefore easily be derived as the limit of the total impedance Z_{tot} for high

frequencies (see eq. C.1 in the appendix).

The other limit is achieved for low frequencies (see eq. C.1 in the appendix). A variation of R_2 results therefore in different axis intercepts of the ordinate (total impedance). Since a capacitive stimulation is seen as the less harmful stimulation

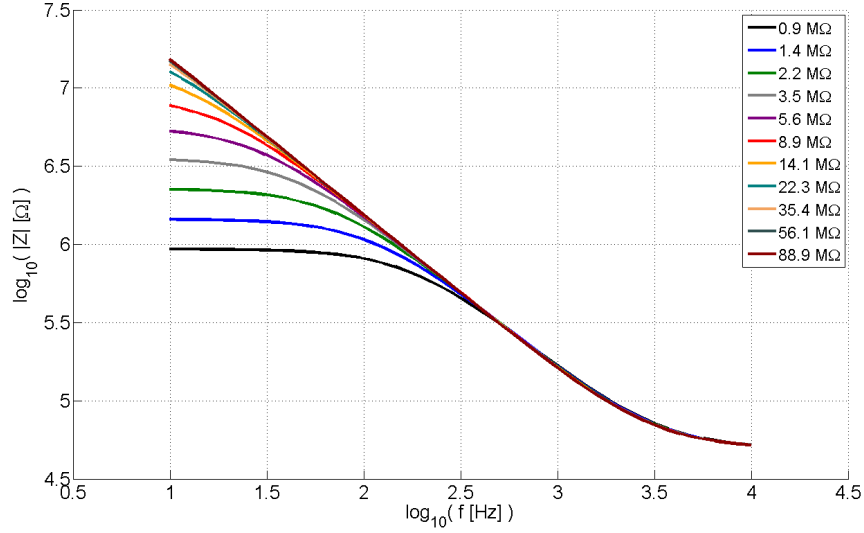


Figure 3.3: influence of R_2 on the impedance in a R(RC)-model

form (see section 1.3.3.4), the capacity turns out to be one of the most important characteristics of a microelectrode (see Fig. 3.4): Higher capacity correlates

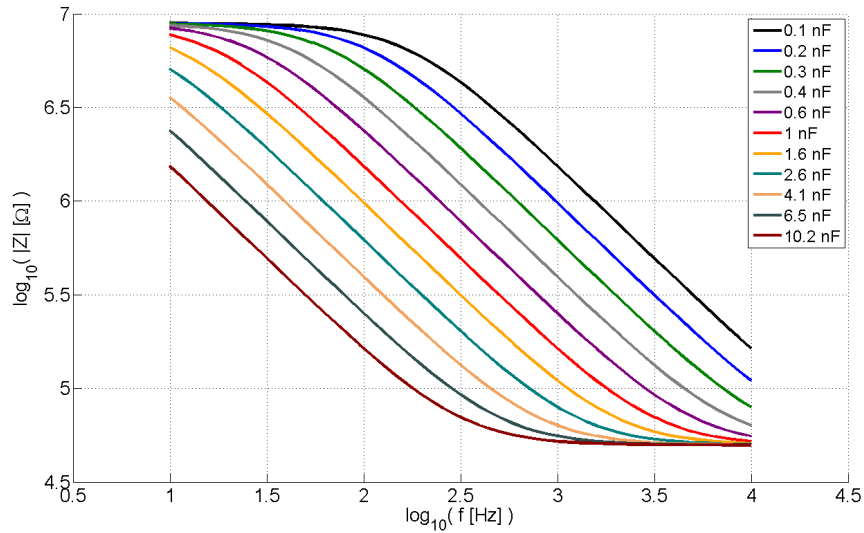


Figure 3.4: influence of the capacitance C on the impedance for a R(RC)-circuit

with a decreasing impedance in large frequency range. Especially for frequencies

between 100 Hz and 1000 Hz the capacitance is the dictating parameter for the total impedance. As seen in Fig. 3.1 the curvature of the graph leads to a constantly varying slope, while in the R(RC)-fitting the slope cannot be adapted with a directly influencing parameter. The fitting algorithm has therefore to adapt the capacitance carefully, balancing the parts where the fitted slope is greater and less than the experimental slope. This makes the R(RC)-model not easy to handle for the impedance spectroscopy.

3.2.2 Simulating Cyclic Voltammetry Data

The components of an equivalent-circuit based simulation are presented in Fig. 3.5. The voltage source is controlled by a stimulation function, creating a current which

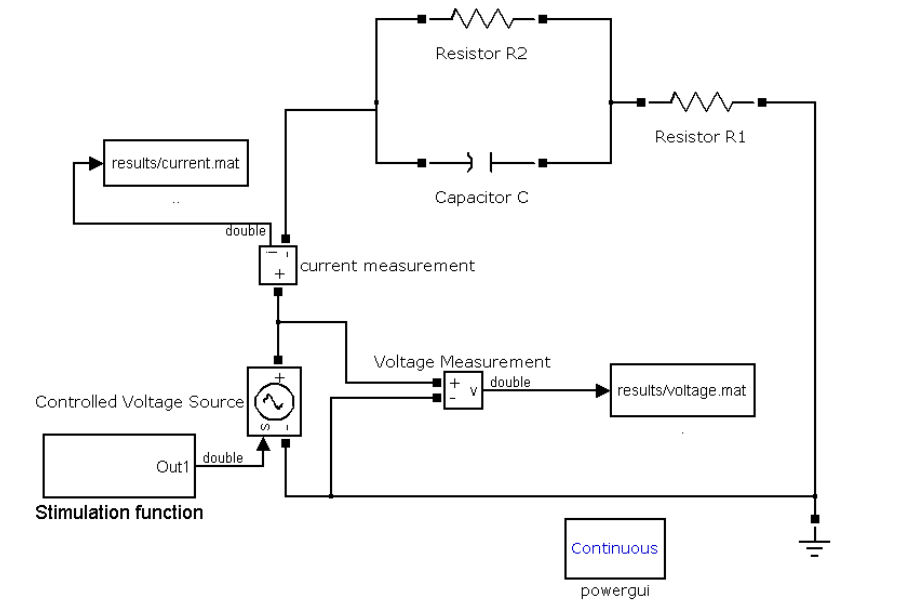


Figure 3.5: MATLAB Simulink simulation of an R(RC)-circuit

passes the resistors R_2 and R_1 and is charging and discharging the capacitor C . Current and voltage drops are measured permanently. The impedance of the reference electrode is assumed to be much lower than the electrode under investigation, due to its macroscopic surface area.

Is a $R(RC)$ -circuit able to reproduce cyclic voltammetry graphs as shown in the experimental part (section 2.1.3.2)? The values of R_1 and R_2 are held constant to $50\text{ k}\Omega$ and $8.89\text{ M}\Omega$ (section 3.2.1). The electrode area is fixed at $A = 177\text{ }\mu\text{m}^2$ (see section 2.1.3.1), but a special focus is put on the influence of the relative capacitance, which is varied from values of blank metal ($\sim 50\text{ }\frac{\mu\text{F}}{\text{cm}^2}$) to values $20\times$ higher than the actual data for activated IrOx [2] (see also Table 2.1). This is done in expectation of further improvements as well, e.g. with conducting polymers or the enhancement of surface roughness. For the stimulation function a triangular function is used (section A.3), which corresponds to the sweep rate used in the experiment (section 2.1.3.2). To keep track of the system, the simulation function is put into a subsystem (smaller system with defined input from and output to the higher-ranking system). It is not varied much in the coming simulations.

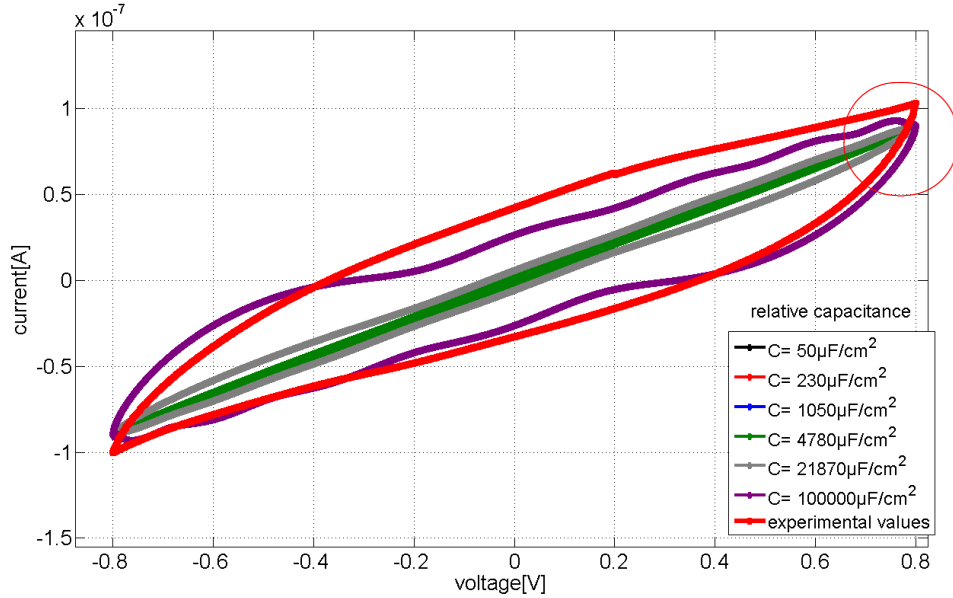


Figure 3.6: cyclic voltammetry simulation with an $R(RC)$ -circuit compared to experimental data, varying the capacitance from $50\text{ }\frac{\mu\text{F}}{\text{cm}^2}$ to $100\text{ }\frac{\text{mF}}{\text{cm}^2}$. The graphs up to $C = 1050\text{ }\frac{\mu\text{F}}{\text{cm}^2}$ are masked. In Fig. 3.7 the graph within the red oval is shown in more detail.

Almost all graphs in Fig. 3.6 have the same slope. This is due to the small sweep rate ($f \rightarrow 0$), which makes $|Z_{\text{Capacitor}}| \gg R_2$ for all relevant capacitances. The area between the curves increases with greater impedance, as it is seen in the definition of the maximal charge capacity (section 2.1.3.2). An exponential increase of current, as seen at extreme voltages and expected from theory (see eq. 1.32), is not reproduced by this model. The resistances R_1 and R_2 are slightly underrated, since the current of this quasi-steady-state is permanently lower than

the experimental graph. As mentioned in section 2.1.3.2, the experimental graph is dominated by a high capacitance, which is most probably not resulting from the physics directly at the electrode-electrolyte surface. When zooming in the "tip" of one of the simulated graphs, it is clear, that an R(RC)-circuit is not able to reproduce an exponential increase of current (which is seen more distinctive in literature [53] [34] [40]), instead a more elliptic behaviour appears (which can be also derived analytically): It is seen, that using an ohmic resistance in parallel to

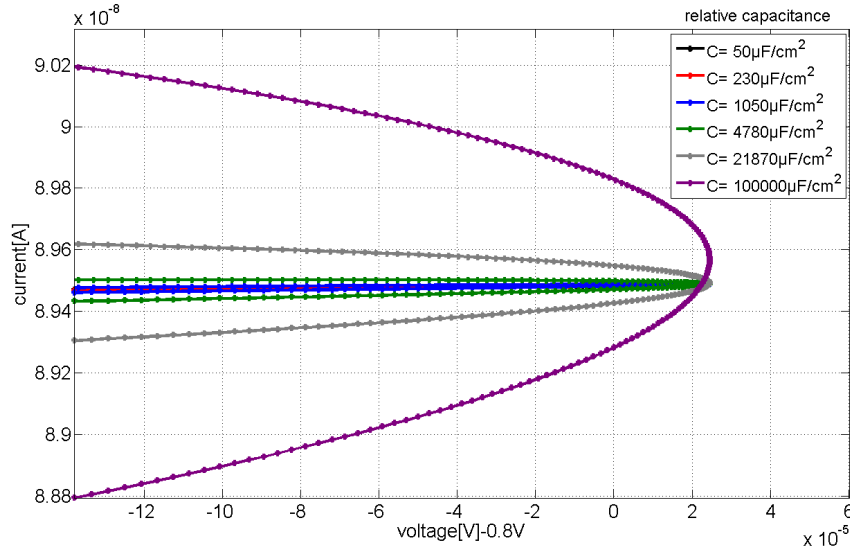


Figure 3.7: Figure 3.6 zoomed in on the voltage at $\sim 0.8 \text{ V}$ (|) influence of the capacitance on the cyclic voltammetry, simulated with an R(RC)-circuit ($C = 50 \frac{\mu\text{F}}{\text{cm}^2} \dots 100 \frac{\text{mF}}{\text{cm}^2}$), the graphs of $C = 50 \frac{\mu\text{F}}{\text{cm}^2}$ and $C = 230 \frac{\mu\text{F}}{\text{cm}^2}$ are masked

the capacitor is just valid for voltages within the water window (=no electrolysis of water, see Table 1.1), while for higher voltages the exponential increase is not reproduced.

3.2.3 Simulating Stimulation Pulses

3.2.3.1 Sinusoidal Stimulation

In this simulation, the voltage drop over the R(RC)-system is set as boundary condition (0.7 V) by the *stimulation function* subsystem (see Fig. 3.5). For frequencies $f > 1 \text{ kHz}$ the low impedance of the capacitor (Fig. 3.8) leads to a decrease of the faradaic current (I_{R_2}) (Fig. 3.9). To remain in this model: Shorter stimulation pulses will achieve a lower (harmful) faradaic current and greater capacitive currents. In the first two periods a transient state of oscillation can be observed. The sum of both currents, I_{R_1} , is increasing with frequency (the increase

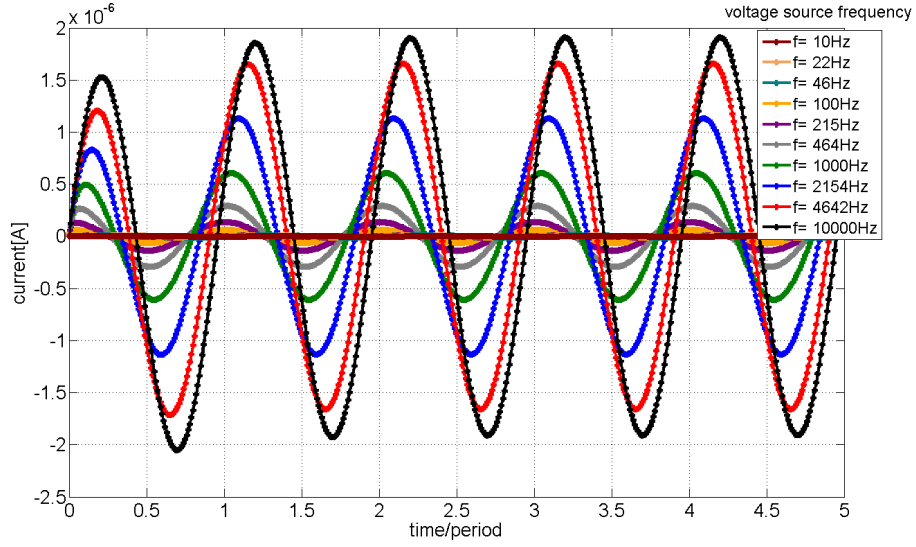


Figure 3.8: influence of the voltage frequency on the capacitive current ($f = 10 \text{ Hz} \dots 10 \text{ kHz}$)

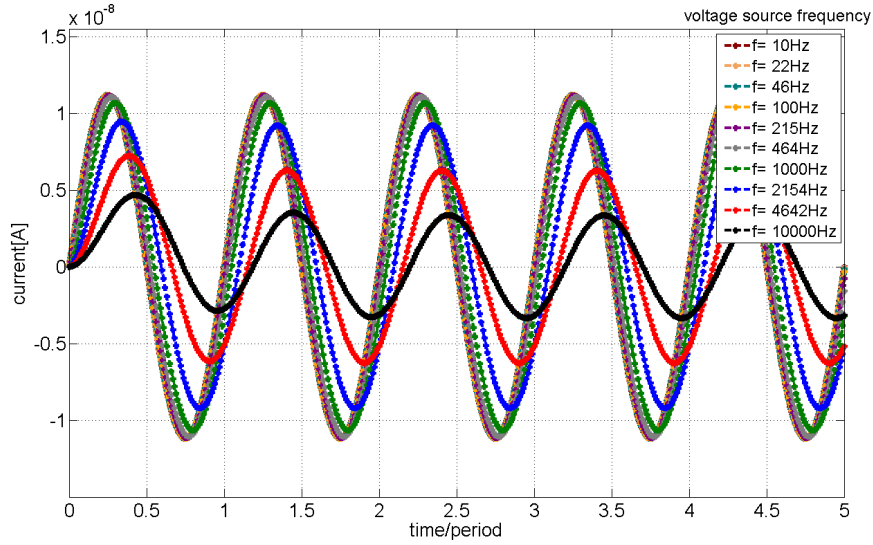


Figure 3.9: influence of the voltage frequency on the faradaic current ($f = 10 \text{ Hz} \dots 10 \text{ kHz}$)

of capacitive currents is in the range of 10^{-6} A , while the decrease of the faradaic current is about 10^{-8} A). This is in congruence to the (experimental) impedance spectroscopy (section 3.2.1). Since all equations in an R(RC)-circuit are linear and invertible (see Table 3.1), the simulations for current controlled sinusoidal stimulation have the same results. Although faradaic currents are two orders of magnitude smaller, they cannot be neglected in general. A small amount of evolved hydrogen in a period may lead to severe damage to the surrounding tissue within

hours.

3.2.3.2 Rectangular Stimulation

The voltage source (Fig. 3.5) is replaced by a current source, which is applying a current of an approximately rectangular shape (see the fourier series section A.3 in the appendix). As a maximal current $1\mu\text{A}$ is applied. Since, R_2 is an *ohmic*

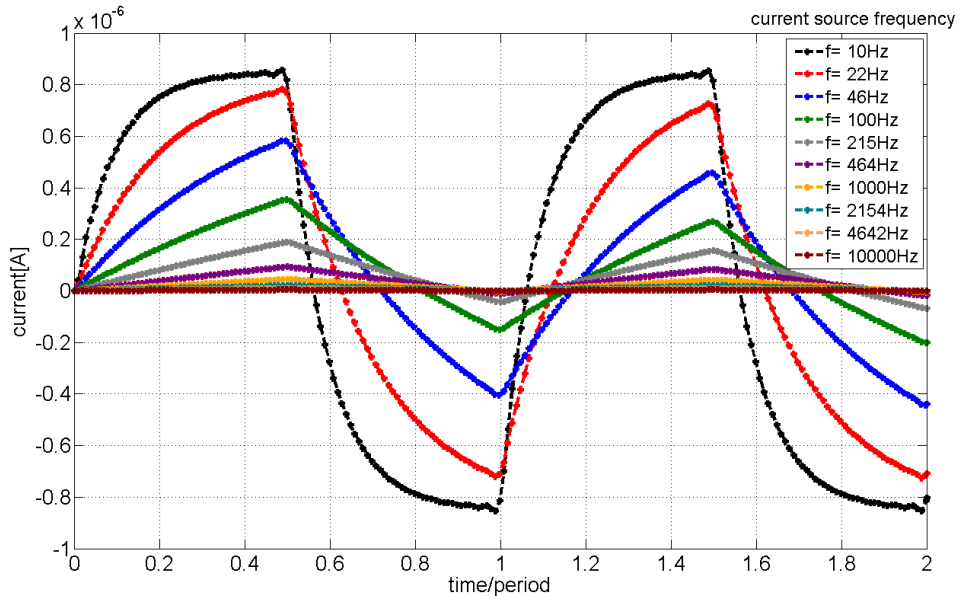


Figure 3.10: influence of the applied current frequency on the faradaic current (I_{R2}). maximal faradaic current $\sim 0.9\mu\text{A}$

resistor, the current is proportional to the voltage drop over both R_2 and C and has therefore a similar graph. At the beginning of one period, the faradaic current is small but increases while the capacitor is loaded and therefore is not able to collect current easily (see Fig. 3.11). Low stimulation frequencies lead to capacitive current peaks in negative and positive directions (if the time is considered in relation to the period). Contrary, the faradaic currents are getting a more and more rectangular shape for lower frequencies (see Fig. 3.10).

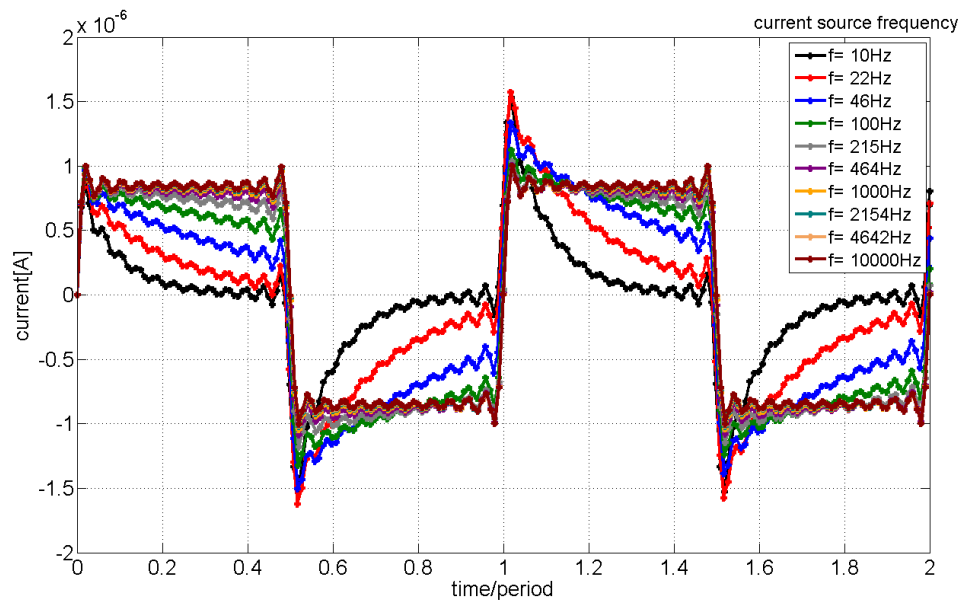
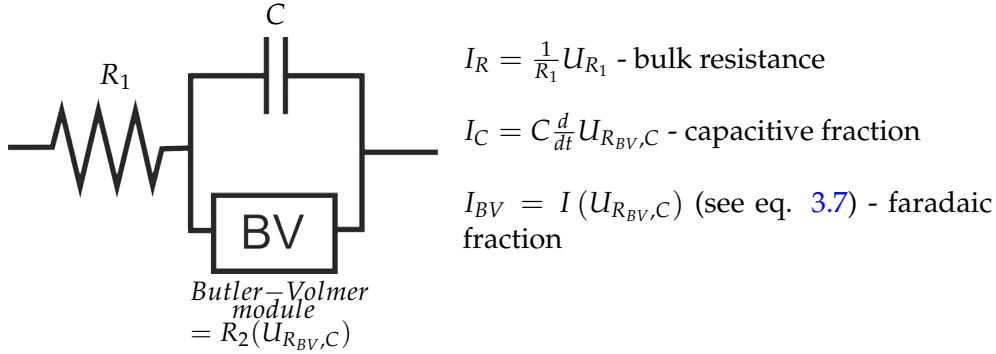


Figure 3.11: influence of the current frequency on the capacitive current (I_C).
maximal capacitive current $\sim 1.5 \mu\text{A}$

3.3 R(BV C)-Circuit Model of a Microelectrode



3.3.1 Butler-Volmer Model

One approach to do simulations for more extreme voltage ranges is to include the kinetics of chemical reactions (eq. 1.29). Hydrogen and oxygen evolution have both standard potentials, which are not extreme (on the contrary to potassium and sodium, e.g. Tabular 1.1). Furthermore, their educts' concentration is high compared to any ion sort ($55 \text{ M} \gg 100 \text{ mM}$) or even proteins [22].

As a first approximation, it is supposed that

$$C^*_{O/R} \approx C_{O/R}(0, t) \quad (3.6)$$

This means, that the concentration of one species at the surface is in the range of its concentration in the bulk medium. The accumulation of ions at the electrode of the opposite charge (mass-transfer) is therefore not taken into account. For this reason, the coming equation (eq. 3.7) seems to be valid just for short stimulation durations compared to the time the ions need to change their location. (E.g. for single pulse stimulations, see [16]). The transfer coefficient α (eq. 1.29) can range from zero to unity ($0 < \alpha < 1$) and is hard to derive for real surfaces [41] [57]. For the O_2 -reaction, values of $0.45 < \alpha < 0.51$ can be found [58], while for the H_2 -reaction it is $\alpha \gtrsim 0.46$ [59]. Because of that, $\alpha \approx 0.5$ is a reasonable assumption. So in total, the ohmic resistance R_2 of the R(RC)-circuit in section 3.2 is replaced by a clearly non linear ¹ resistor of the type

$$i = I_{BV} = \hat{i}_0 A \left[i_{O_2} \sinh \left(\frac{e}{2kT} (U - U_{O_2}) \right) + i_{H_2} \sinh \left(\frac{e}{2kT} (U - U_{H_2}) \right) \right] \quad (3.7)$$

A is the electrode area and U_{O_2} and U_{H_2} stand for the standard potentials of the electrolysis of water (see section 1.3.3.5). The exchange current densities can be found in literature:

¹means: not proportional to (with or without an offset)

$$i_{O_2} = 2.8 \times 10^{-7} \frac{A}{cm^2} \text{ (a value for platinum [58])}$$

$$i_{H_2} = 9.8 \times 10^{-4} \frac{A}{cm^2} \text{ (also for Pt [60])}$$

The only quantity which is still undetermined, is the dimensionless parameter \hat{i}_0 . With this parameter, the difference between the systems Pt and Ir/IrOx is considered and also the influence of H_2SO_4 as a promoter. \hat{i}_0 is adapted once by the cyclic voltammetry data and then fixed for the impedance spectroscopy and for all other simulations. At first sight, the hydrogen evolution seems negligible because of $i_{O_2} \gg i_{H_2}$, but this is fully compensated by the exponential term for negative potentials U :

$$\frac{2.8 \times 10^{-7}}{9.8 \times 10^{-4}} \ll \exp\left(\alpha \frac{e}{kT} \times 2V\right) \quad (3.8)$$

When the only one parameter is fitted, the so built Butler-Volmer “module” has to reproduce the outcomes of the cyclic voltammetry (section 2.1.3.2) and the impedance spectroscopy (section 2.1.3.2). It then will be used to simulate some results in higher voltage ranges, which cannot be measured in experiment, because of the danger of electrochemical damage. In the next simulation parts, the former ohmic resistance R_2 is replaced by a subsystem, which contains the simplified Butler-Volmer-equation (eq.3.7).

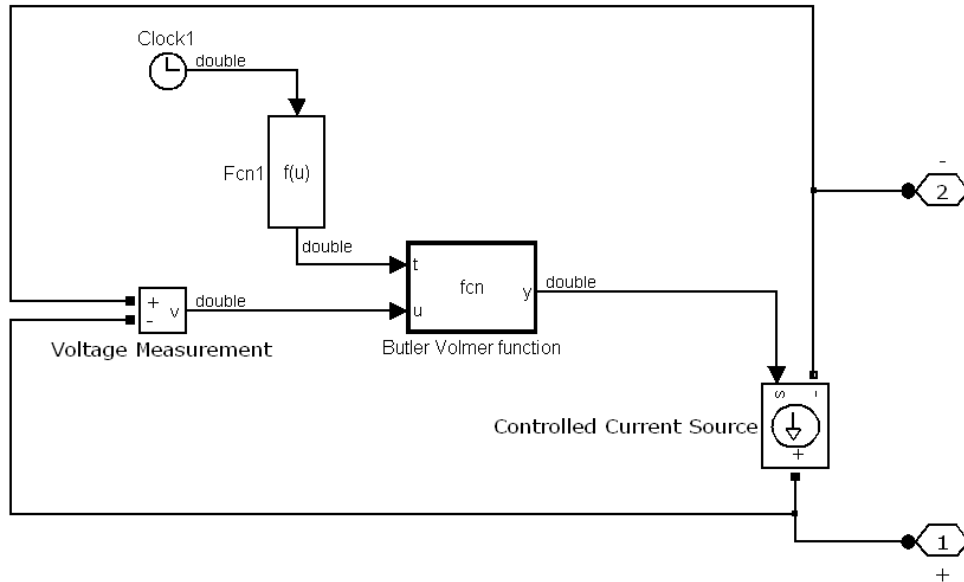


Figure 3.12: butler-volmer subsystem (nonlinear resistance) in the simulation based on an equivalent circuit model, replacing the former ohmic resistance R_2 (Fig. 3.5)

The subsystem (see Fig. 3.12) is measuring the voltage drop between the two points 1 and 2, which is equivalent to the voltage before and after the capacitor, since the capacitor is in parallel to this subsystem. It then injects a current according to eq. 3.7. The parameter t is introduced for numerical stability. It is starting from 0 on and reaches 1 in the first simulation steps and is multiplied at the argument of the hyperbolic sine.

3.3.2 Simulating Cyclic Voltammetry Data

The cyclic voltammetry data is used to derive an acceptable value of \hat{i}_0 . For this reason this section is put before the simulated impedance spectroscopy. The same capacitance and serial resistance was used as in the R(RC)-simulation (Fig. 3.7). The stimulation function is again a triangular function approximated by a finite fourier series with an amplitude of 0.8 V and a sweep rate of $100 \frac{\text{mV}}{\text{s}}$ leading to a period of 32 s.

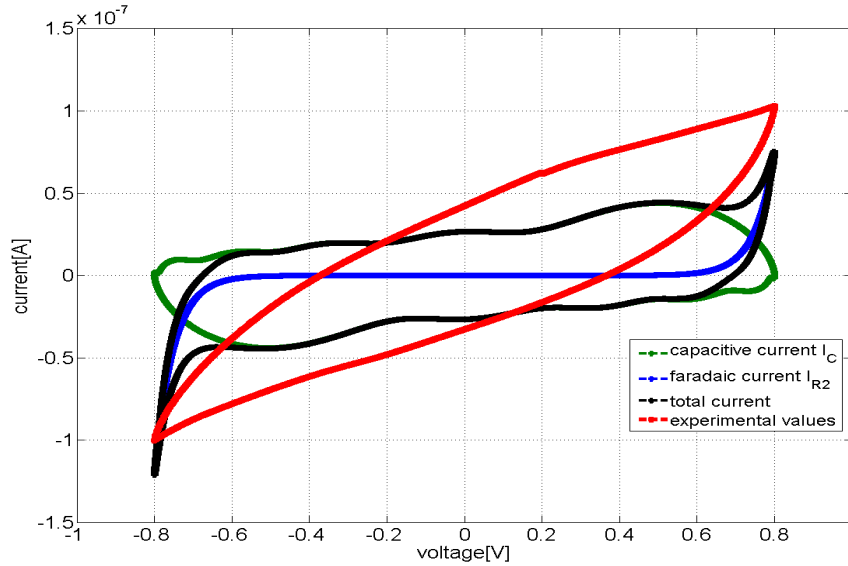


Figure 3.13: cyclic voltammetry simulated with a Butler-Volmer equation compared to experimental data

As seen in Fig. 3.13, the simulation describes this single experimental data not precisely. Though, it reproduces the exponential increase of the current which is seen on many cyclic voltammetry graphs in literature [50] [52] [51] instead. The capacitance remains to be adapted as well. The only parameter which has to be fitted is fixed at $\hat{i}_0 = 2.7 \times 10^{-12}$. A variation of \hat{i}_0 leads to higher or lower peaks at the extreme voltage ranges:

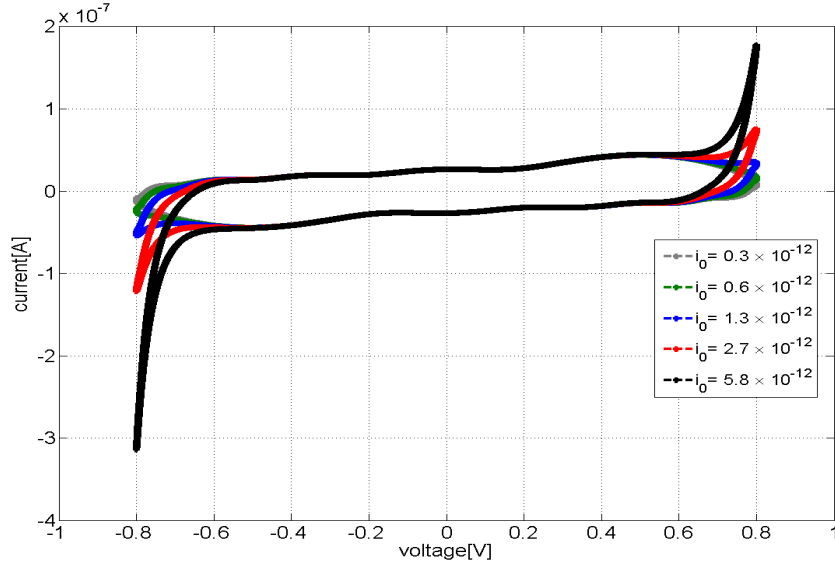


Figure 3.14: cyclic voltammetry simulated with a Butler-Volmer equation varying the current constant \hat{i}_0

3.3.3 Simulating Impedance Spectroscopy Data

In eq. 3.7 a function $i(U)$ is given, which can be converted into an ohmic law:

$$i = i(U) = \underbrace{\frac{i(U)}{U}}_{=R_2(U)} U \quad (3.9)$$

The graph of an impedance spectroscopy plot is not just varying with frequency but also with the amplitude and has the same effect as varying R_2 (see Fig. 3.3). With eq. 3.7 an analytical solution can be obtained and plotted (Fig. 3.15).

First, it can be stated, that the effect of faradaic currents cannot be neglected for potentials $U \gtrsim 0.8 \text{ V}$ and slow frequencies $f \lesssim 300 \text{ Hz}$. Furthermore, as seen also in section 3.3.2 the impedance is not symmetric in respect to the voltage. Stimulation function that fulfil condition $|\int U_- dt| = |\int U_+ dt|$ can anyhow cause an accumulation of electric charges (“unbalanced pulses” see section 1.3.3.1 and 1.3.3.5).

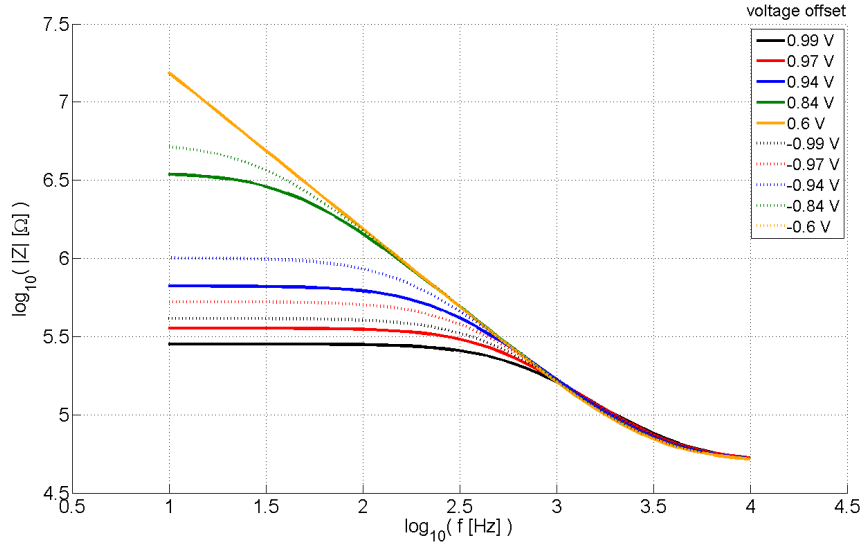


Figure 3.15: influence of the voltage offset on the impedance spectroscopy graph simulated analytically with a simplified Butler-Volmer equation

3.3.4 Simulating Stimulation Pulses

3.3.4.1 Voltage Controlled Stimulation

Like in the case of the R(RC)-simulation (see section 3.2.3.1) the sinusoidal stimulation is taken as an example for the voltage controlled stimulation. The amplitude is fixed at 0.7 V and the frequency of the stimulating voltage is varied.

As seen in Fig. 3.16, the faradaic current is again in the range of 10^{-8} A, but in contrast to the R(RC)-simulation (Fig. 3.9), not a sine can be seen. The maximal faradaic current depends on the frequency. It converges to a certain limit for slow frequencies and diminishes for high frequencies. For these stimulation frequencies, the capacitive currents are so high, that the resulting increase of the potential drop over the resistance in series (R_1) reduces the voltage over the Butler-Volmer module remarkably. Moreover, there are sharp peaks for high voltages (not shown), while for lower voltages the current diminishes rapidly. This is typical for a function $f : t \mapsto \sinh \circ (a \cdot \sin(t))$, $a \gg 1$ like the simplified Butler-Volmer equation (eq. 3.7). In accordance with the impedance spectroscopy and the cyclic voltammetry, the absolute value of the current for negative voltages (H_2 -evolution) is greater than for positive ones (O_2 -evolution). The amplitude dependence of the impedance (see section 3.3.3) of the R-(BV C)-circuit is also seen for a sine and varying the stimulation amplitude (Fig. 3.17). In the case of an ohmic resistor, the faradaic current would increase proportional to the voltage applied (so $2\times$). The increase is apparently much higher.

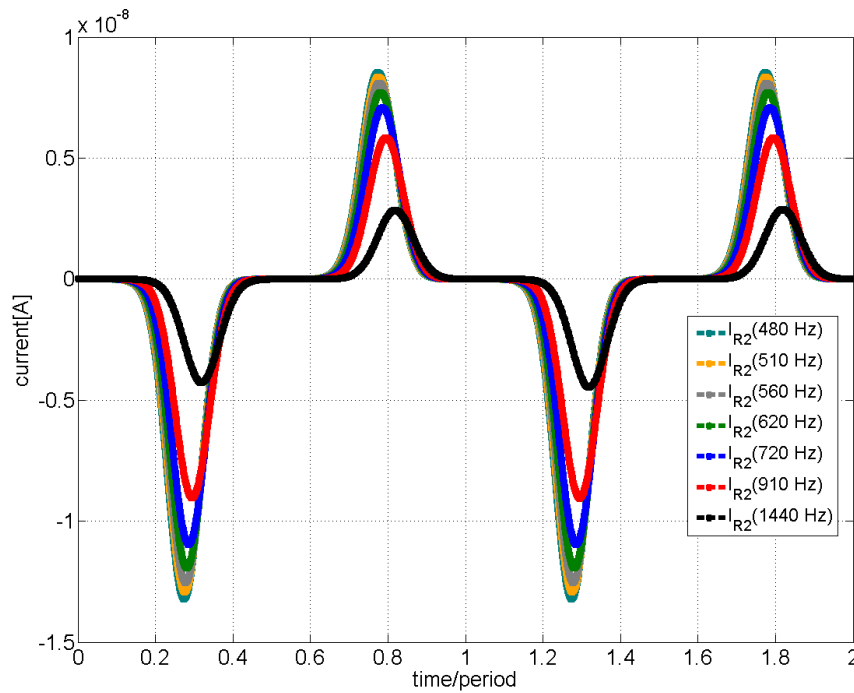


Figure 3.16: faradaic current simulated with a simplified Butler-Volmer equation 3.7, varying the frequency of the sinusoidal voltage applied with an amplitude of 0.7 V

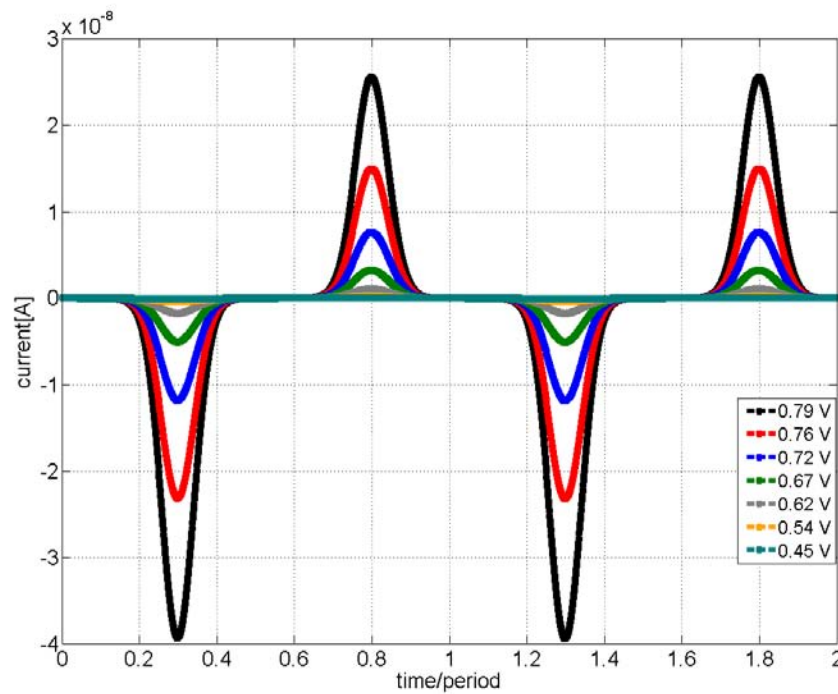


Figure 3.17: influence of the amplitude of the applied sinusoidal voltage on the faradaic current simulated with a simplified Butler-Volmer equation

3.3.4.2 Current Controlled Stimulation

A current-balanced stimulation is mainly used to prevent damage from the sensitive and complex neuronal tissue [16] [27], because it assures that after one cycle the sum of currents brought into the system is zero (section 1.3.3.1). How much of the products of the electrochemical reactions is left after one cycle, taking the hydrogen and oxygen evolution (Table 1.1) into account?

As seen in section 3.3.2 the simplified Butler-Volmer equation is bijective and therefore invertible. It reads

$$U(i) = \left(U_{H_2} + \frac{kT}{e} \ln \left(\frac{i + \sqrt{i^2 + i_{O_2}^2 i_{H_2}^2 + i_{O_2} i_{H_2} 2 \cosh(\Delta U)}}{i_{H_2} + i_{O_2} \exp(\Delta U)} \right) \right) \cdot (-1)^{1-\theta(i)} \quad (3.10)$$

The abbreviation $\Delta U := \frac{e}{kT} \cdot (U_{H_2} - U_{O_2})$ and $i_{O_2} = i_0 A i_{O_2}$ are used and $(-1)^{1-\theta(i)}$ with the Heaviside function θ is just changing the sign if i does. So, this function consists mainly of two logarithmical functions. The voltage source for stimulation is replaced by a current source and in the Butler-Volmer (BV) subsystem the current source is replaced by a voltage source. The subsystem is now measuring the current that is needed to fulfil the boundary condition given by the current source and sets a calculated voltage drop over the BV-system and the capacitor. For numerical rea-

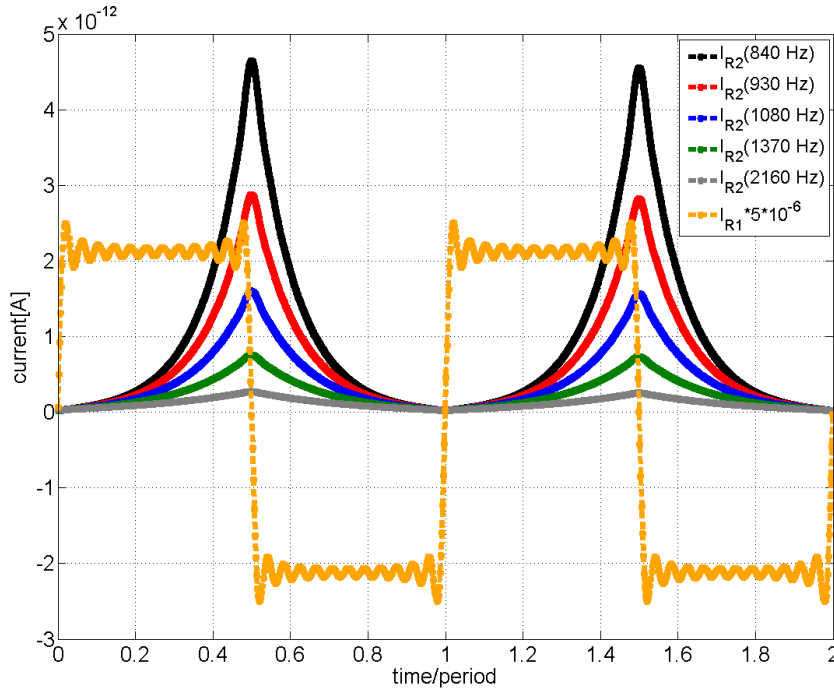


Figure 3.18: simulated current through the Butler-Volmer subsystem ($I_{R2} = I_{BV}$) in dependence of the frequency of the current controlled stimulation

sons a small ohmic resistor (1Ω) had to be connected in series with the capacitor. The capacitance and the bulk resistance was taken from section 3.2.1, while for the amplitude of the current a value of $0.5\mu\text{A}$ was chosen, it has an rectangular shape (f_{23} , section A.3). It is apparent in Fig. 3.18 that the current flowing through the Butler-Volmer (BV) subsystem is not changing its sign during stimulation. This is due to a (relatively) high capacitance, which leads to $U_{BV} = UC < 0$ for all times, when loaded. Starting from $i = 0$, $U = 0$, electrical charge is applied on the capacitor (in the anodic phase e.g.) which is subtracted in the cathodic phase afterwards. When changing the stimulus function $i(t) \leftrightarrow -i(t)$ the graph is below the x-axis. This is non-physical, because the graph depends strongly on the initial conditions concerning whether the capacitor is first loaded with a negative or a positive charge. For higher currents not all of the charge applied remains on the capacitor, which is therefore not able to “deliver” the required amount of charges in the following phase, causing chemical reactions to gain the rest. As expected from

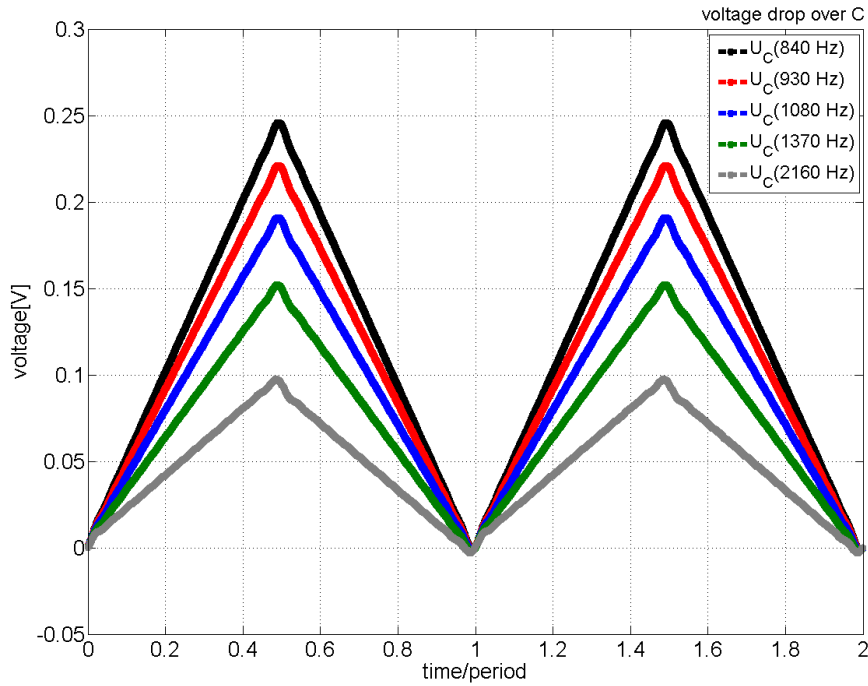



Figure 3.19: simulated voltage which drops over the capacitor in dependence of the frequency of the current controlled stimulation

Fig. 3.15, the voltage drop at the surface diminishes in Fig. 3.19 with increasing stimulation frequencies, because the impedance of the capacitor is decreasing.

3.3.5 Summary and Outlook

An equivalent circuit model using capacitor and ohmic resistances was modified, taking electrolysis of water with the evolution of hydrogen and oxygen gas into account. By implementing a simplified Butler-Volmer equation, it becomes evident that the faradaic current is very sensitive to the applied voltage and the impedance of microelectrodes is therefore changing for different voltages. Because of that an effective “charged balanced” pulse is not easy to achieve. To improve this approach first a precise knowledge of the transfer coefficients for IrOx is necessary. Second, the mass transfer of reactants shall be taken into account with the introduction of a leaking capacitor. Its charge represents then a certain chemical reactant and the leakage stands for the diffusion rate.

3.4 R-CPE-Circuit Model of a Microelectrode



$$I_R = \frac{1}{R} U_R$$

$$I_{CPE} = Y_n \frac{d^n}{dt^n} U_{CPE}$$

3.4.1 Simulating Impedance Spectroscopy Data

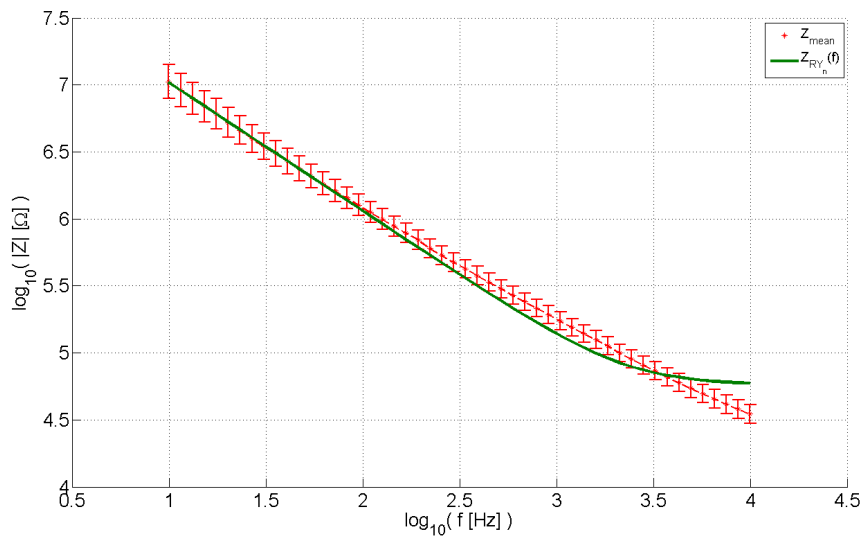


Figure 3.20: impedance spectroscopy: fitting data from electrode 112E (Z_{mean}) with a Constant Phase Element ($Z_{RY_n}(f)$)

In Fig. 3.20 the impedance spectroscopy data (section 2.1.3.2) is averaged and compared to an analytical solution of the system of capacitor, CPE and ohmic resistor using Table 3.1.

The results of the fitting of the experimental data to the parameters of the analytical solution are:

$$\begin{aligned} R &= 5.8 \pm 3.5 \times 10^4 \Omega \\ n &= 0.958 \pm 0.009 \\ Y_n &= 1.81 \pm 0.05 \times 10^{-9} \frac{s^{0.958}}{\Omega} \end{aligned}$$

Because of the fractional order derivative (section A.1), the dimension is changing also in a “fractional” way, leading to $\frac{s^{0.958}}{\Omega} \neq \frac{s^1}{\Omega} = F$. The influence of each parameter to the graph of the impedance spectroscopy is investigated by varying the parameters within wide limits. Similar to the R(RC)-circuit (see Figure 3.2) the bulk resistance R yields an offset of the impedance for high frequencies (figure in the appendix, see C.6). The effect of Y_n is comparable to the capacitance (see Figure 3.4 for the R(RC)-circuit and the appendix C.7 for the CPE simulation). A changing of the derivative order n is seen directly both in the slope and in the impedance for low frequencies.

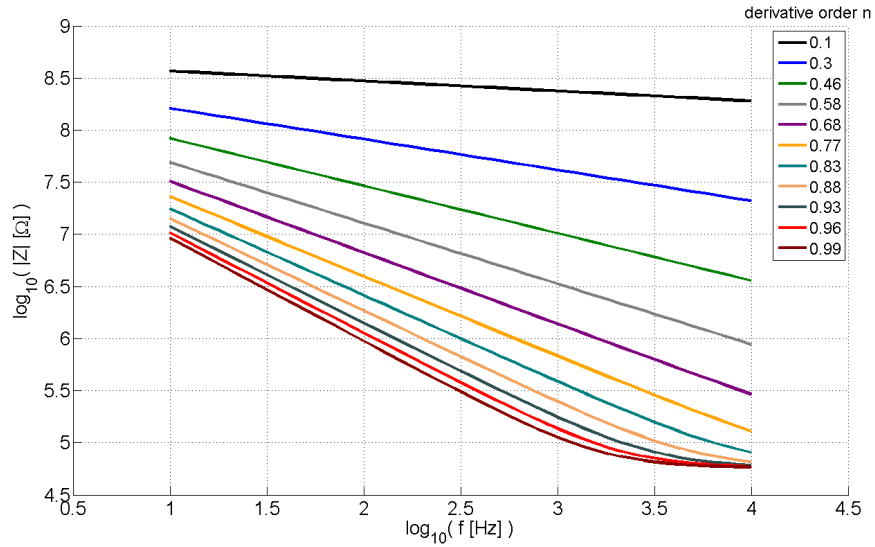


Figure 3.21: influence of the differentiation order n on the impedance of the fitted $RCPE$ -circuit

Even though it is mathematically no problem to simulate for $n > 1$, this behaviour would exceed an ideal capacitor ($n = 1$), which was never seen in an experiment nor found in literature. The CPE fitting emerges as a kind of R(RC) fitting, where the slope of the logarithmical impedance can be adapted instead of the absolute values of the impedance for direct current.

3.4.2 Simulating Cyclic Voltammetry Data

For the simulation the capacitor (C) and the resistor in parallel (R_2) are both replaced by a CPE subsystem:

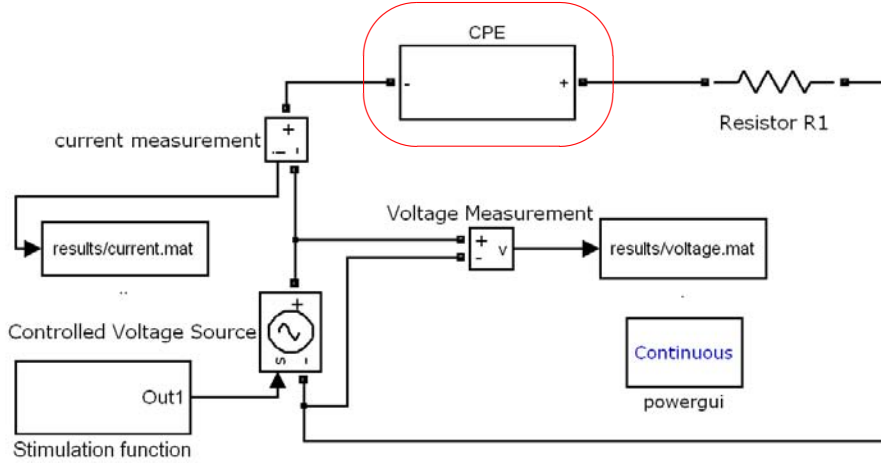


Figure 3.22: equivalent circuit simulation using a Constant Phase Element subsystem (I)

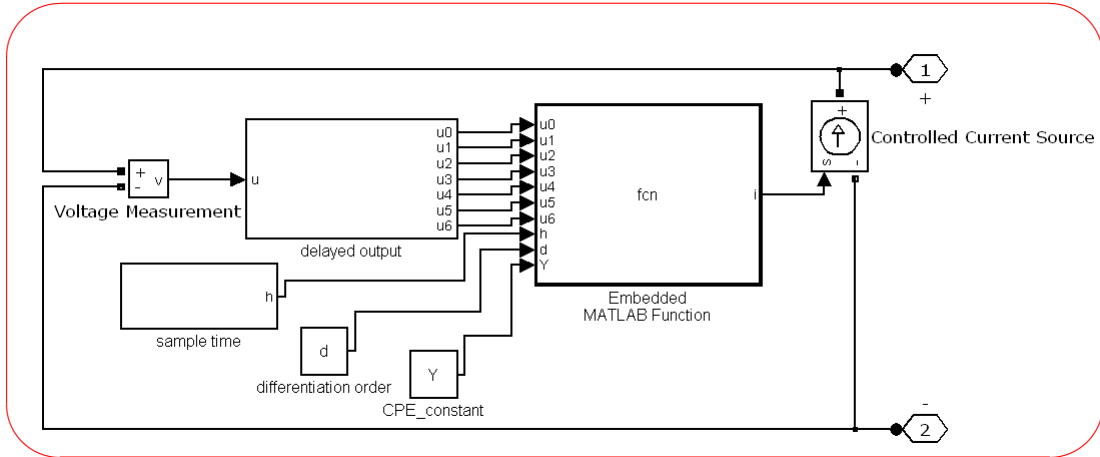


Figure 3.23: equivalent circuit simulation: Constant Phase Element subsystem

Like in the case of Butler-Volmer (Fig. 3.12), a voltage is measured and a calculated amount of current is injected into the system. In the “delayed output” box the voltage signal is stored for up to 100 simulation steps (in Fig. 3.23 just 6 steps are shown). In such a way u_5 in Figure 3.23 contains the voltage five sample times before the actual simulation step. The number of stored simulation steps varies from simulation to simulation and is discussed in section 3.4.4. The sample rate h is calculated as the difference of the actual time and the time of the last step, whereas the differentiation order d can be chosen by the Matlab script, which is running the

simulation. The "Embedded MATLAB Function" is calculating the fractional order derivative (eq.A.1) with the actual and the saved voltage values in the past. To make use of eq. A.1, the simulation runs with fixed time steps, while the current is calculated with $i = Y_n \frac{d^n U}{dt^n}$ (eq. 3.4) and $d = n$ ¹. Six preceding voltage values proved to be sufficient to reproduce the cases of the ohmic resistor ($n = 0$) and the ideal capacitor ($n = 1$). Due to numerical reasons (it turned out to be difficult to simulate the full 32 s for a cycle) the ohmic resistance in series is put to 0Ω . Since the electrode impedance in these frequency ranges (section 2.1.3.2) is much higher ($> 10^8 \Omega$) than the bulk resistance ($50 \text{ k}\Omega$), this simplification can be made. The constants of the impedance spectroscopy fitting (section 3.4.1) are taken and the CPE-constant Y_n is varied. It is seen in Fig. 3.24, that a fitting of the CPE-constant

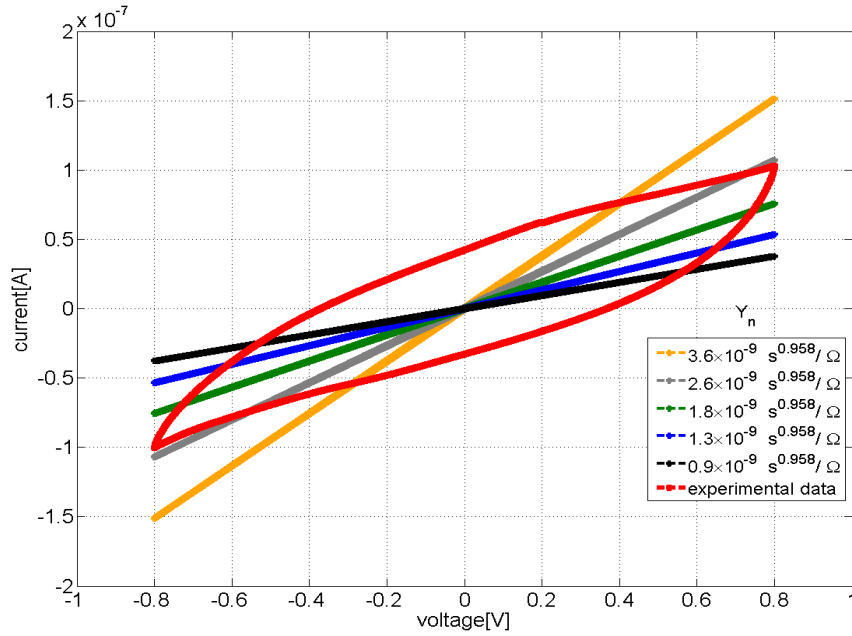


Figure 3.24: cyclic voltammetry simulated with a CPE for different Y_n in comparison to experimental data

is not easily achieved. Though there are some minimal capacitive effects in a range of 10^{-9} A (not demonstrated here), the hysteresis effect cannot be manipulated as easy as in the R(RC)-model (section 3.2.2) by fitting just one parameter. To see major capacitive effects, a differentiation index of ~ 1 is apparently necessary. So, it is varied in Fig. 3.25 from $d = 0.99997$ to $d = 0.99757$, while all other parameters remain the same as before.

Because of numerical artefacts in the case of a fourier series stimulation func-

¹To be in congruence with literature the CPE index is not defined as d

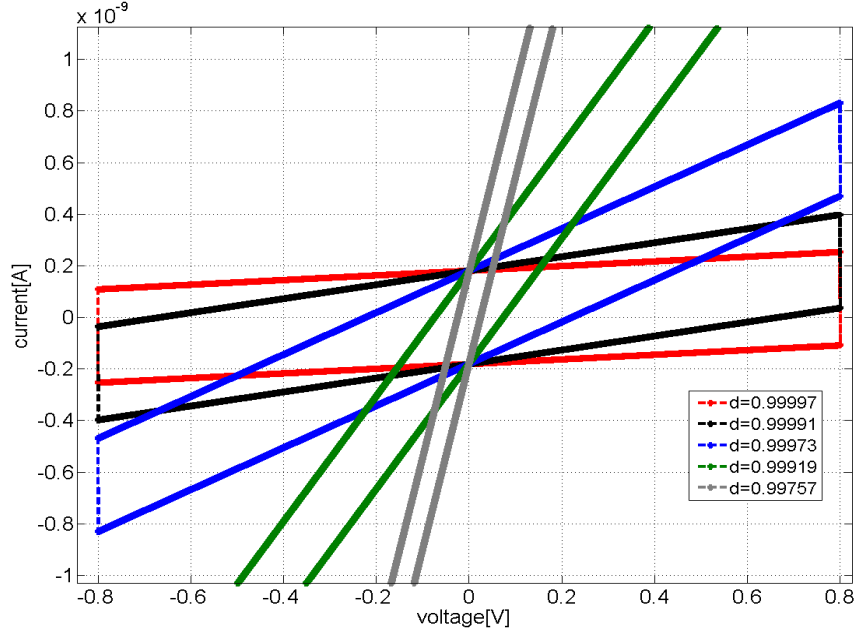


Figure 3.25: influence of differentiation index $n = d$ on the cyclic voltammetry simulated with a CPE ($Y_n = 1.81 \times 10^{-9} \frac{s^n}{\Omega}$)

tion, the triangular function was achieved by a piecewise definition. In this case, the function is not differentiable at its maxima, therefore a gap appears when the current (proportional to the fractional order derivative) is calculated (3.25). As soon as the differentiation index has a finite difference which is not one, the character of the ohmic resistance part gets evident and the current is proportional to the voltage applied. The changes made to the amount of hysteresis are relatively small, especially it is not feasible to adapt the capacitance effect directly, as it is in the $R(RC)$ model with the capacitance. However, the influence of the number of considered previous simulation steps has to be investigated further: Because the fractional order derivative is calculated just from 6 voltage steps, a small sample time leads to a negligence of voltages different from the actual voltage. It seems that the ohmic character (current proportional to the actual voltage) is emphasized too much (see also section 3.4.4), though a whole-number derivative is also just taking two values with infinitesimal distance into account.

3.4.3 Simulating Stimulation Pulses

3.4.3.1 Voltage Controlled Stimulation

The CPE is set at its original values (section 3.4.1), but the bulk resistance remains $0 \text{ k}\Omega$. A sine with an amplitude of 0.7 V is applied and the stimulation frequency

of the sinusoidal stimulus is varied. As also seen in section 3.4.1 there are greater currents for smaller frequencies. Because the CPE is in series with the bulk resistance and there are no additional elements, there is just the total current. In

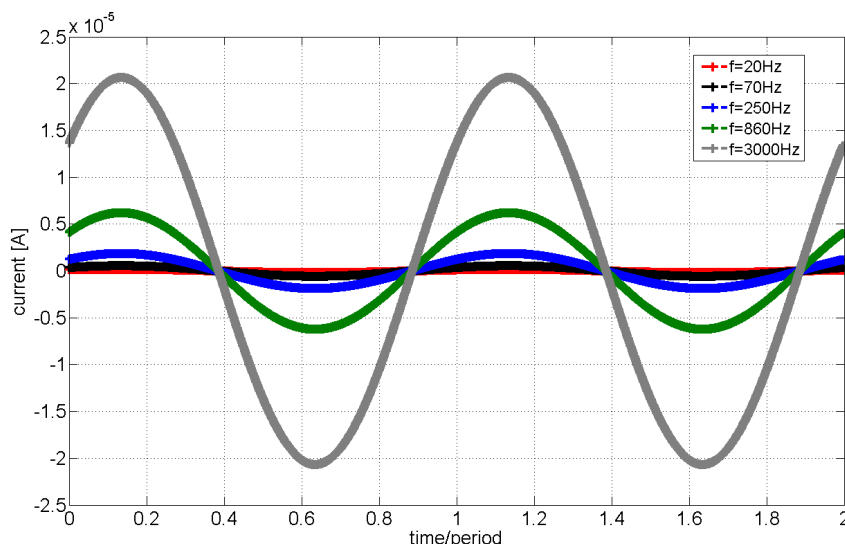


Figure 3.26: simulated currents through a CPE for a sinusoidal voltage of 0.7 V and different frequencies

general, this kind of frequency dependence is similar to the capacitor ($0.958 \approx 1$) and could also be expected from the impedance spectroscopy (section 3.4.1). For lower differentiation indices the currents are becoming more and more independent of the applied frequency (not shown here). To demonstrate the phase delay caused by different differentiation indices $n = d$, all graphs in Fig. 3.27 are plotted in relation to their maximum. A phase delay of the current in relation to the applied voltage of $\frac{\pi}{2}n$ is expected. The usual 6 terms of the fractional order derivative are considered. The voltage is applied using a sine of 100 Hz and is calculated with a sampling rate of just 3 kHz. For numerical stability the ohmic resistance representing the bulk solution is set to 0Ω . As seen, the phase varies between 0° (for $d = 0$) and 90° (for $d = 1$). Especially the case of an ohmic resistor and an ideal capacitor can be reproduced by this simulation of an CPE. The form remains a sine, the phase delay is correct and the amplitude is just a question of a factor multiplied in the equations (a direct comparison seems not to be reasonable with respect to the varying dimensions of Y_n). Though, this simulation seems not to be stable: Numerical problems occur if an ohmic resistor is connected in series and for other (especially for “finer”) relations of the sampling rate to stimulation frequency a tendency is seen, that most of the sine have a phase which is close to the $d = 0$ graph. A picture of this can be seen in the appendix (Fig. C.4.1).

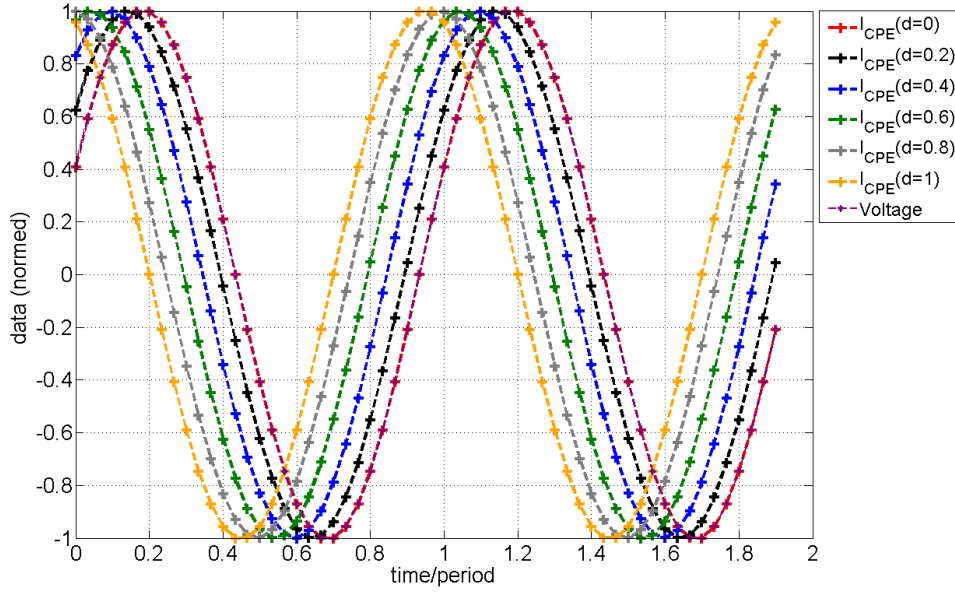


Figure 3.27: phase of currents in a CPE-simulation in relation to the applied voltage for different differentiation orders $d = n$

3.4.3.2 Current Controlled Stimulation

The current controlled system is using the fractional order integration according to Weyl in the CPE-module (shown in section A.2). Since the convergence of the equation is just linear and not proportional to a binomial coefficient (section A.1), 16 previous steps were taken into account. The parameters are selected according to the results of section 3.4.1, especially the bulk resistance is not selected 0Ω but $58\text{ k}\Omega$. A current of $1\mu\text{A}$ is applied in a rectangular pulse shape (approximated by a finite fourier series).

In Fig. 3.28 the sum of the voltage drop over the CPE and the ohmic resistance is plotted. The voltage is increasing proportional to the integral of the current. This is similar to the capacitor, what can be explained by $0.958 \approx 1$. For higher stimulation frequencies lower voltages are necessary again (see section 3.4.1).

To investigate the transition of an ohmic resistor to a capacitor, the differentiation index is varied in Fig. 3.29. To establish comparability between the graphs, the voltages are normed to their maximal values. Since the constant Y_n is depended on the fitted parameter n both in its value and in its dimension, the voltages cannot be compared without adapting Y_n . For the capacitor ($n = d = 1$) the voltages decrease proportional to the electrical charge. Because $\Gamma(0)$ is undefined, the Weyl integral is not explained for $d = 0$, but the signal of a capacitor is clear: the voltage is directly proportional to the applied current and therefore has the same

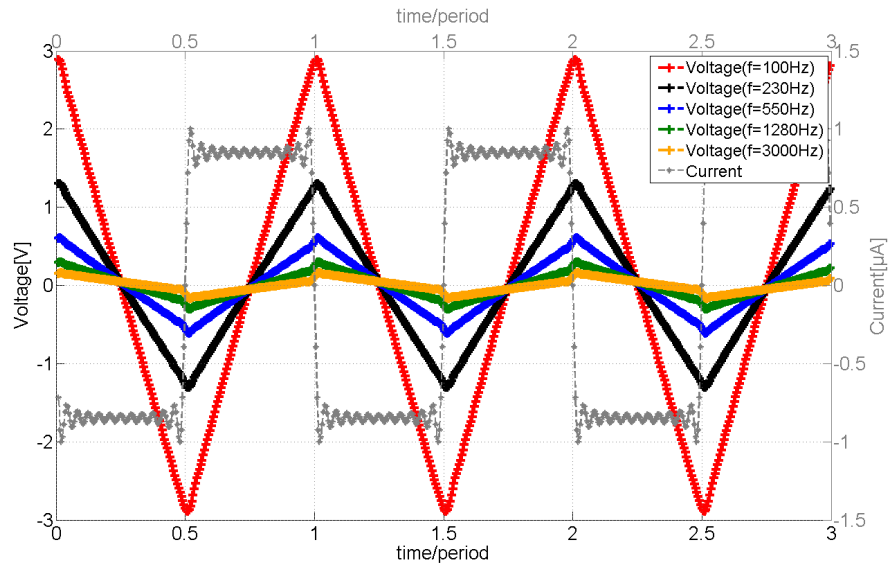


Figure 3.28: simulated voltage drop over the CPE and the bulk resistance in series with a current controlled rectangular stimulation for different stimulation frequencies ($d=0.958$)

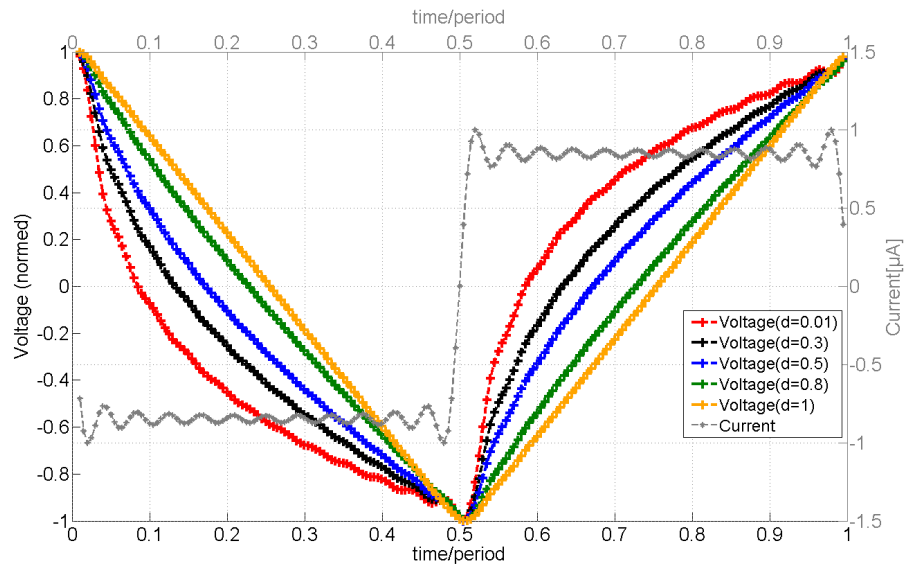


Figure 3.29: influence of the differentiation index $n = d$ on the voltage drop simulated with a current controlled equivalent circuit

pulse shape. So a transition of the resulting voltage shapes with varying $d = n$ can be seen as the changing of a triangular to a rectangular function. Since the rectangular pulse form is created by a sum of sine, the phase delay cannot be verified at first sight in this picture. For sinusoidal stimulation, calculation of the correct phase remains to be a problem. It is also problematic in the current controlled

stimulation (not demonstrated here).

3.4.4 Summary and Outlook

In this section, the system of capacitor and resistor was replaced by a Constant Phase Element, which represents a composition of both in one subsystem. Its character (ohmic or capacitive) can be varied with the differentiation index. The measured graph in the impedance spectroscopy could be described easier than in a R(RC)-model by directly fitting the slope in the double-logarithmic plot. The resulting voltages and currents are in the same range as in previous stimulations and seem reasonable. Also the resulting phase difference of voltage and current, as well as the behaviour of an ohmic resistor and capacitor was reproduced. However, numerical and technical problems persist. The simulation with an ohmic resistor in series failed in the case of the fractional order derivative. For the calculation of the fractional order derivative or integration, just a finite number of previous simulation steps is saved. The outcome of the fractional order derivative is influenced by the ratio of stimulation frequency to sampling frequency. The saved simulation steps are directly coupled to the sample time. Therefore a high sample frequency considers solely values in the vicinity. In the fractional order derivative definition, given by Grünwald and Letnikov, the sample time h is fixed (see section A.1). This might be enhanced to varying sample times, so that a “dynamical” choice of step sizes can be taken. For the current controlled stimulation it is essential, that the simulation steps for a whole period are taken into account. In this case, the fractional order integration subsystem worked accurate and stable.

Also the changing of the dimension of the proportionality constant Y_n for different derivative indices n is counterintuitive. It shall be investigated whether there exist some constants \hat{R} and \hat{C} with dimensions of a resistor and a capacitor, so that $Y_n = \frac{(\hat{R}\hat{C})^n}{\hat{R}}$. In this case different Y_n could be compared to each other using \hat{R} and \hat{C} .

3.5 Summary and Outlook of the considered Electrode Models

An equivalent circuit model turned out to be a proper tool to get an idea about the dimensions of the parameters which are not given by the experiment. The stimulation with ohmic resistors and ideal capacitors proofed to be the most stable simulation, with a description for medium frequencies and stimulation amplitudes. For higher voltage ranges, a simplified Butler-Volmer equation was used to replace

the ohmic resistor leading to an exponential increase of currents for increasing voltages (seen at the cyclic voltammetry). The parameters of the CPE are relatively easy to fit at the impedance spectroscopy graph. The CPE is the only model, which allows the adjustment of the phase of current to voltage by a direct parameter. For one of these models or their combination one might think of a program written in C++ or Python. This program would be able to calculate the resulting current or voltage in real time or at least, when the stimulation function is set. The user is then informed *before* the simulation about the possible damage to neuronal tissue and the microelectrode. For every cycle, the net injected charge could be calculated and compared to a limit of solubility for H_2 and O_2 in water to predict the evolution of hydrogen and oxygen bubbles. Preconditions for this are a precise knowledge about the physical and electrochemical properties of the MEAs used. Especially the changing of these characteristics due to stimulation shall be investigated. If the dominant chemical reactions occurring with faradaic stimulations are understood, the normal ohmic resistor can be replaced by other systems. For stimulation frequencies in a wide range, the combination of a CPE and the Butler-Volmer equation is useful. Special benefit is achieved, when not more than two or three parameters have to be adapted for this system. The RC-element, the BV-C-element and the CPE imply just two parameters each.

3.6 Simulation of a two Microelectrode System based on a $R(RC)$ -Model

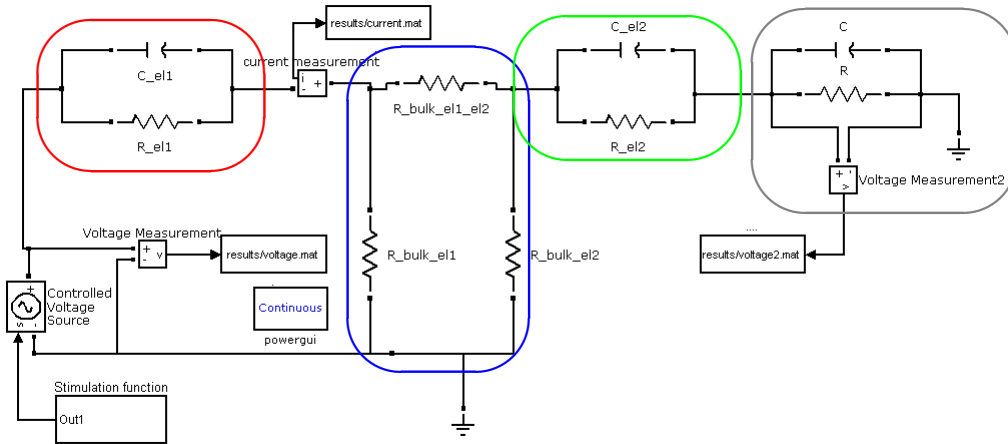


Figure 3.30: simulation setup with implemented stimulating (I) and recording electrode (I), bulk resistances(I) and measurement system (I)

A system of a stimulating and a separated recording electrode is considered. The bulk resistance between these two electrodes ($R_{bulk_el1_el2}$) was estimated using the impedance spectroscopy: In the case, one electrode is used as working electrode and the counter electrode is on the same MEA, a bulk resistance of around $22\text{ k}\Omega$ is measured (distance: $50\text{ }\mu\text{m}$, not demonstrated here). If the resistance is taken linear with space, for the distance stimulating MEA to recording MEA ($\sim 30\text{ mm}$), a resistance of $13\text{ M}\Omega$ is derived. The parasitic capacitance was estimated 10 pF by the electronic workshop of the institute, while the measurement resistance of $1\text{ G}\Omega$ was taken from the construction plans of the main amplifier (section 2.1.1). The capacitance and resistance values of both electrodes were taken from section 2.1.3.2. In the case of the stimulating electrode the capacitance and resistance is adapted (see section 3.6.3), when all 16 electrodes are stimulating. Since the diameter of each electrode of the Two-Shank-MEA is different from the electrodes of the Four-Shank-MEA, the impedance was calculated linearly in the first case. The only parameter which has to be adapted, is the R_{el1} and R_{el2} respectively: Though, for the impedance spectroscopy (section 3.2.1) they were fixed at around $50\text{ k}\Omega$ (due to a guess of the *AutoLab* frequency response analyser software), they are now set to $10\text{ k}\Omega$. One reason for this is, that in the impedance spectroscopy a chlorinated silver-wire was used, while in the experiments an Ag/AgCl -pellet with a porous an therefore larger surface was employed. In this section, the influence of the characteristics of a recording electrode on the

measured signal is simulated. Because phase delays are not considered and the same low amplitudes like in the experiment were applied, a $R(RC)$ model is used. Experimental and simulated data are compared and it is discussed, whether the simulation is therefore able to reproduce the experimental results. In each part the reference to the experimental counterpart is given. It is therefore recommended to have a look on the graphs there, especially to bear in mind also the variances of the single electrodes.

3.6.1 Stimulation Frequency Dependence

How much of the applied signal is transferred to the recording system? To compare simulated with experimental data (section 2.3.1.1) a sinusoidal stimulation was applied with an amplitude of 95 mVpp and various frequencies. The experimental graph was taken as a mean for all recording electrodes, while the errorbars stand for the square root of the sample variance. In Fig. 3.31, both simulated and recorded

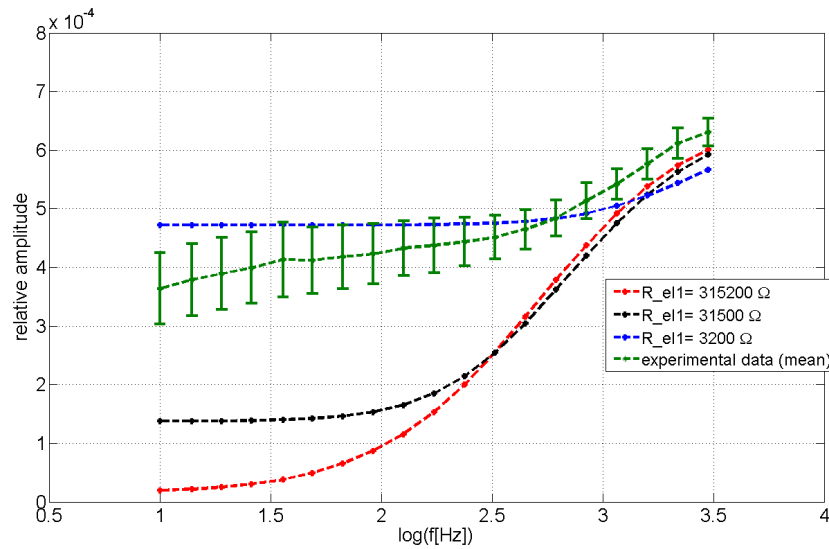


Figure 3.31: simulated ratio of recorded to stimulation amplitude for a sinusoidal stimulation with 95 mVpp varying the frequency. For the ohmic resistance of the stimulating electrode the values $\sim 320 \text{ k}\Omega$, $\sim 32 \text{ k}\Omega$ and $\sim 3.2 \text{ k}\Omega$ are taken.

graphs show a relative amplitude in the same range, increasing with the stimulating frequency. For frequencies $f \leq 400 \text{ Hz}$ the difference is much higher. Better results for this range can be achieved by lowering the parallel resistance of the stimulating electrode by the factor of $\frac{1}{100}$. In this case the impedance is low even for slow stimulations and the relative amplitudes remains high. Though, this low parallel

resistance then does not fit to the results of the impedance spectroscopy. A decreasing parallel resistance of the recording electrode leads to a similar but far smaller effect (not demonstrated here). The influence of its impedance is investigated later.

3.6.2 Amplitude Dependence

Is the recorded signal proportional to the stimulation strength? In the experiment, this question is clearly confirmed (section 2.3.1.2). Since, in the equivalent circuit simulation, just the operations whole number-differentiation, integration (capacitor) and division (resistor) are taking place, a constant is not effected and the system is clearly linear. (This was also done, but not demonstrated here.) In the case of the Butler-Volmer simulation, the proportionality is not given, because of the exponential conductance for higher voltages. If the fractional order derivative or integration is used, the results are also proportional to the applied boundary conditions.

3.6.3 Dependence on the Number of Stimulating Electrodes

In order to vary the number of stimulating electrodes, the capacitor and the resistance in parallel have not to be replaced by n identical ones, but can change values in the way $C_n = n \times C$ and $R_n = \frac{R}{n}$ with the number of stimulating channels n for a given capacitance C and resistance R of a single electrode. Here a simulation is done for a sinusoidal stimulation of 95 mVpp and 126 Hz. For comparison, the

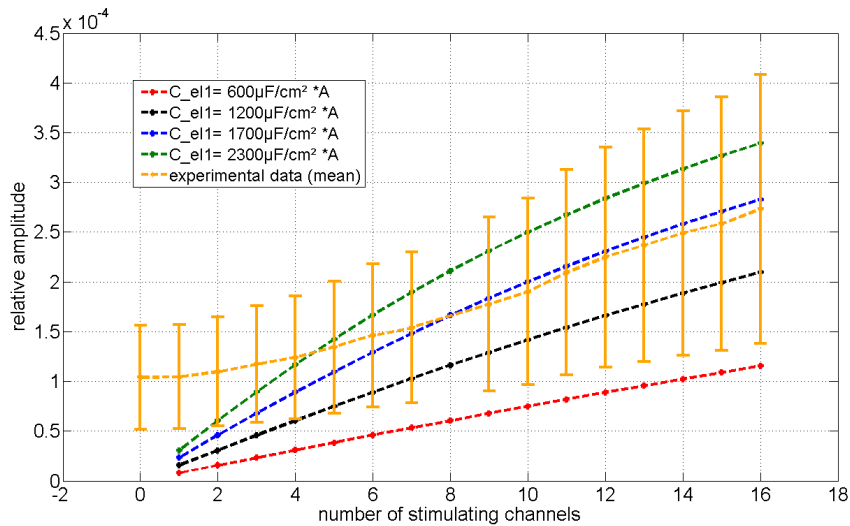


Figure 3.32: simulated ratio of recorded to stimulation amplitude for a sinusoidal stimulation with 95 mVpp and 126 Hz for different numbers of stimulating channels and their capacitance per area

experimental data (section 2.3.1.3) is also plotted in Fig. 3.32. The errorbars stand for the square root of the sample variance of the different recording channels. To give additional information, the relative capacitance of the stimulating electrode is varied. The graphs show a good congruence of the recorded and the simulated data. Since the stimulation amplitude was just around 50 mVpp, a relative amplitude of 1×10^{-4} refers to a difference of just 5 μ V which is in accordance to the noise (in the experiment the data of “no channels are stimulating” marks the noise level, indeed). No matter, whether the impedance is increased by the number of stimulating electrodes (experiment and simulation) or by increasing the relative capacitance (simulation), it is seen that a rise of the total capacitance is effecting the measured signal directly.

3.6.4 Spatial Dependence

In the equivalent circuit model the ohmic resistance between two microelectrodes is commensurate with their spatial distance. Hence, the resistance is increased linearly to a value consistent with 15 mm to 35 mm. This is the spatial distance used in the experiment (see section 2.3.1.4). The same parameters as in the experiment were used (sine of 180 mVpp) and the stimulation frequency was varied. It can be

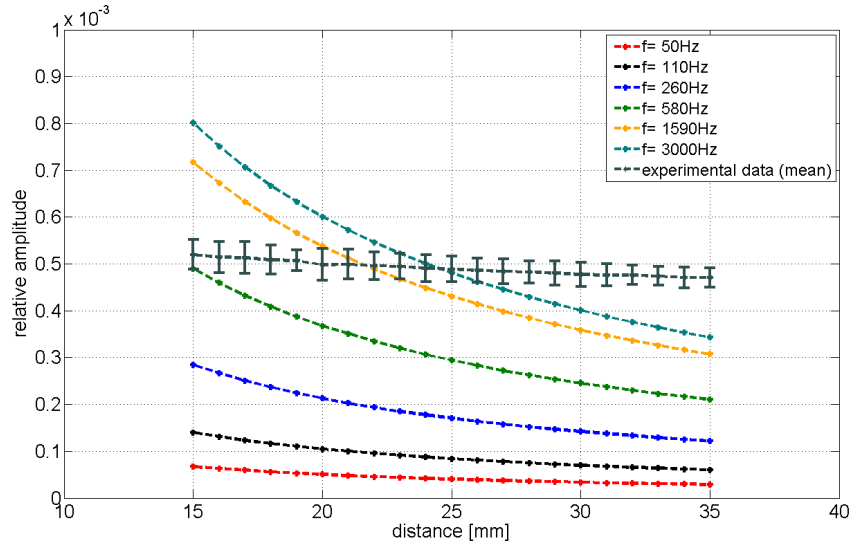


Figure 3.33: simulated ratio of recorded to stimulation amplitude for a sinusoidal stimulation with 180 mVpp. The distance from stimulating to recording MEA and the stimulation frequency is varied. For comparison the experimental results for a stimulation frequency of 1600 Hz are plotted.

seen, that the small and linear decrease of the recorded signal is not reproduced by the model correctly. Indeed, it's behavior is similar to far smaller stimulation

frequencies, where the relative amplitude is lower in general, though. This may be due to the fact, that the ohmic resistance between the two electrodes is taken as a resistor, which is increasing linearly with distance. However, for greater distances the conductive cross-section is increasing and is lowering the resistance in this way. For lower distances - not in the mm/cm but in the μm range the linear extrapolation might work, though.

3.6.5 Concentration Dependence

Two parameters are changing in the actual model, when the ion concentration is increasing: The bulk resistance is decreasing continuously, since $R \propto \frac{1}{c(\text{ions})}$ [30]. The debye-length λ_D (see eq. 1.10) is decreasing and therefore the capacitance is continuously increasing (see section 1.3.2 and [33]). These two effects lead to a higher relative amplitude for higher concentrations (not demonstrated here) and do not describe the maxima found in Fig. 2.27 for higher frequencies ($f \gtrsim 500 \text{ Hz}$).

3.6.6 Dependence on the Capacitance of the Recording Electrode

The capacity per area of the microelectrode is varied and the relative amplitude is calculated for a sinusoidal stimulation of 100 mV and different frequencies. According to the scheme of the simulation (Fig. 3.30) it is clear, that the ca-

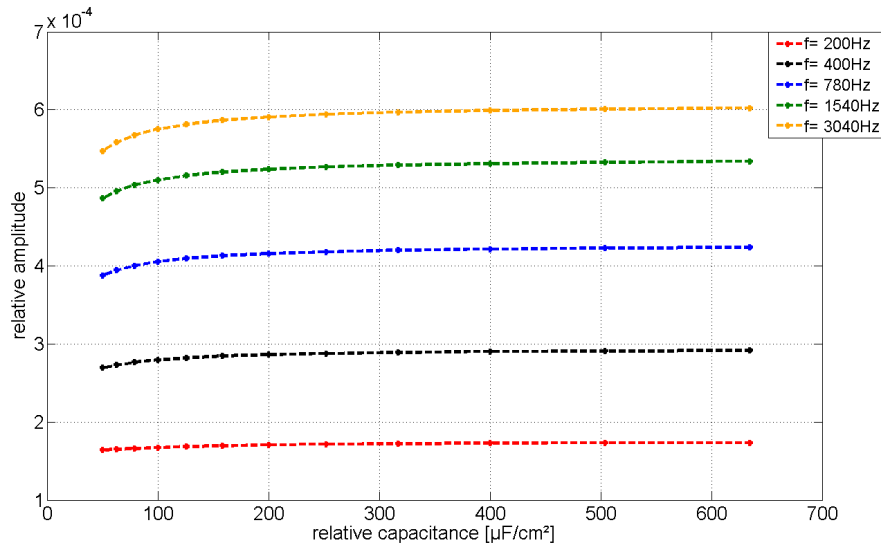


Figure 3.34: influence of the capacitance per area of the recording electrode and the stimulation frequency simulated on the ratio of recorded to stimulation amplitude for a sinusoidal stimulation with 100 mV_{pp}

pacitor and resistor of the recording electrode are blocking the currents with their

common impedance, which are then flowing over the $1\text{ G}\Omega$ resistance. Since the voltage is measured over an ohmic resistance, the voltage drop would be a direct measure of the currents. This is not the case due to a frequency dependence of a small parasitic capacitance. For a small electrode impedance in relation to the measuring resistance, electrode capacitance has only little influence on the results. The results shown in eq. 3.34 are therefore different, when using a $100\text{ M}\Omega$ measurement resistance instead. For each frequency, the amplitude increases according to a $1 - e^{-C/C^*}$ function (C^* stands for a fixed capacitance). Beyond a capacitive per area of $300 \frac{\mu\text{F}}{\text{cm}^2}$ even for small frequencies no major changes in the recorded amplitude occur. Differences of the measured amplitudes of different electrodes (see Fig. 2.23, 2.24, 2.25) cannot be explained by varying capacitances only.

3.6.7 Parasitic Capacitance Dependence

“Parasitic capacitance” refers to the ability of a measurement system to store electrical charges. This attribute is not intended in the design of electrical devices but comes as a side effect when feedlines become long and systems more and more complex. What is the impact of the parasitic capacitances of the measurement system on the data recorded? To investigate this effect, the capacitance C of the model system (Fig. 3.30) is varied, while a sinusoidal stimulation of an amplitude of 100 mV and various frequencies is applied. For all frequencies, a linear decrease

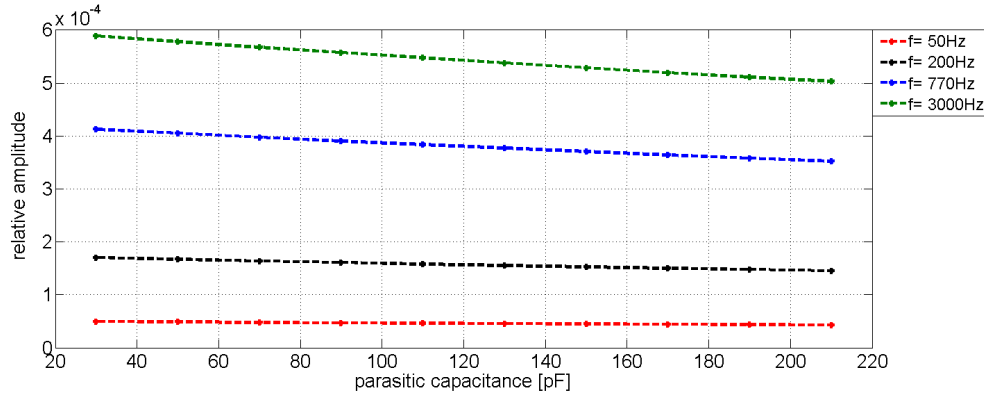


Figure 3.35: simulated ratio of recorded to stimulation amplitude for a sinusoidal stimulation with 100 mV and different frequencies. The influence of the parasitic capacitance of the recording system is investigated.

of the recorded amplitude can be stated. For higher frequencies this decrease ($\frac{d(\text{relative amplitude})}{dC}$) of the relative amplitude is higher than for slower stimuli, but remains low. In summary, the parasitic capacitance has no decisive influence on the measured results.

3.6.8 Summary and Outlook

In this section, a system of stimulating and recording electrode with an idealized measurement unit was simulated. The simulation yields relative amplitudes in the range of 10^{-4} which is in congruence to the experimental results. However, there are major differences in the behaviour for smaller frequencies and for varying distances of stimulating to recording electrode. When increasing the number of stimulating electrodes, this shows to be equivalent with the linear growth of the capacitance and conductance of a single electrode. The dependence of the signal to the ion concentrations could not be explained so far. The ohmic resistances representing the bulk solution turned out to be important. A proper analytical solution and more precise data which is not overridden by huge electrode impedances is needed. To take one electrode in the experiment as the working electrode and the other as the counter **and** reference electrode results in unreliable data, since a solid grounding with a low impedance electrode is necessary. As seen in the experimental part (section 2.3) one and the same physical potential disturbance will cause different amplitudes on the various electrodes. It might be an idea, to characterize each electrode using impedance spectroscopy and cyclic voltammetry and then to weight every signal according to the known characteristics.

Chapter 4

Finite Element Simulation

4.1 Motivation and Overview

The fork-like design of both MEAs (Fig. 2.3 and Fig. 2.4) is not unintended. The sharp tips shall penetrate neuronal tissue and stimulate while every electrode is in a defined position in the organism. First, this leads to a case where a measurement between the electrodes is not possible without changing and disturbing the system. Second, the neuronal tissue in the very near of each shank is going to be destroyed at the implantation process. A question therefore is how much a cell in between the electrode shanks is effected by the potential disturbance of the stimulation function. In literature, many simulations can be found, that approximate neuronal tissue as an isotropic ohmic resistor. The distribution of the applied potential V_{ext} is calculated with Laplace's equation in the form $\nabla^2 V_{ext} \cdot \sigma = 0$ [35] [3] [61] [62]. The diffusion constants of the electrical charges and the influence of the cell membranes are averaged using the conductivity σ , which is determined empirically. Values between 0.2 S/m and $\sim 0.8 \text{ S/m}$ are obtained. By this method, a quick and stable simulation of the electrical field distribution is possible.

There are two key points in the simulation: The first one is the potential drop in the medium due to the electrolytic double-layer (see chapter 1.3.2). The second one is the amount of faradaic to capacitive currents. *Laotaveerungrueng et. al* [63] placed an additional ohmic resistance layer onto the electrode surface with a conductivity of just 0.05 S/m to get in congruence with experimental data. For the amount of injected electrical charges, *S. Joucla and B. Yvert* [31] used a combination of boundary conditions (see section 1.3.2). Though, many simulations do not take the exponential drop of the applied voltage into account. In all cases much of the temporal behaviour of the system is lost, since the conductivity of neuronal tissue is held constant. Resulting capacitive effects are neglected and all simulated currents are purely ohmic (what is not intended as a gentle stimulation (section

1.3.3.5)). Also the changing of differences in the electrode surface geometry cannot be calculated using FEM-techniques so that empirical or fitted parameters are necessary.

4.2 Simulation Settings

Here a new approach for a finite element model is tested. Like in the experimental part, PBS is used as a model system (section 1.2.2). For every ion sort the concentration at each time step is calculated. Since all ions do need time to migrate corresponding to their diffusion constants, a temporal component is introduced. This allows a prediction of the activation of neuronal tissue according to the Goldman-Hodgkin-Huxley equation (section 1.2.1). In general, a study of the double layer capacitance and a simulation of the faradaic currents following the Butler-Volmer equation (eq. 1.29) are also possible. (For the later a precise knowledge of the concentration of all reactants directly at the surface is needed.) A meshing in the range of the debye-length (10^{-9} m) turned out to be technically impossible in the three-dimensional case. Therefore the exponential decrease of the potential and the resulting concentrations were studied in the one-dimensional case (not demonstrated here, see also Fig.1 in [64] and eq. (10) and (11) in [65]) and the simulation was run for a capacitive stimulation (~ 1 V). This approach contrasts therefore with the equivalent circuit simulation in chapter 3. There, models of the electrode-electrolyte surface were tested, simplifying the spatial distribution by an ohmic resistor, summarizing the ion movements as a flow of electrons and neglecting the mechanical inertia of the ions.

For the geometry, two shanks were implemented in two dimensions according to the Neuronexus four-shank electrode (Fig. 2.3) and extruded for $15\text{ }\mu\text{m}$. Then the electrode sites were created with a radius of $7.5\text{ }\mu\text{m}$ and were placed as flat disks onto the shanks. Finally, a box was created with $200\text{ }\mu\text{m} \times 3400\text{ }\mu\text{m} \times 100\text{ }\mu\text{m}$ (width \times length \times depth), marking the borders of the simulated space.

4.2.1 Equations to solve

The electric field is thought as the superposition of two single fields: The first one ($-\vec{\nabla}V_{ext}$) is caused by the presence or absence of free electrons at the electrode surface made of metal. So there are no loads in the bulk medium and the Laplace's equation can be solved using the Dirichlet boundary conditions (setting one electrode surface to a certain potential, see section 1.3.2). The second electrical field ($-\vec{\nabla}V_{int}$) stems from the distribution of electrical loads *within the bulk medium*. These two fields in the sum act as the potential, with the gradient directing the ions' movements.

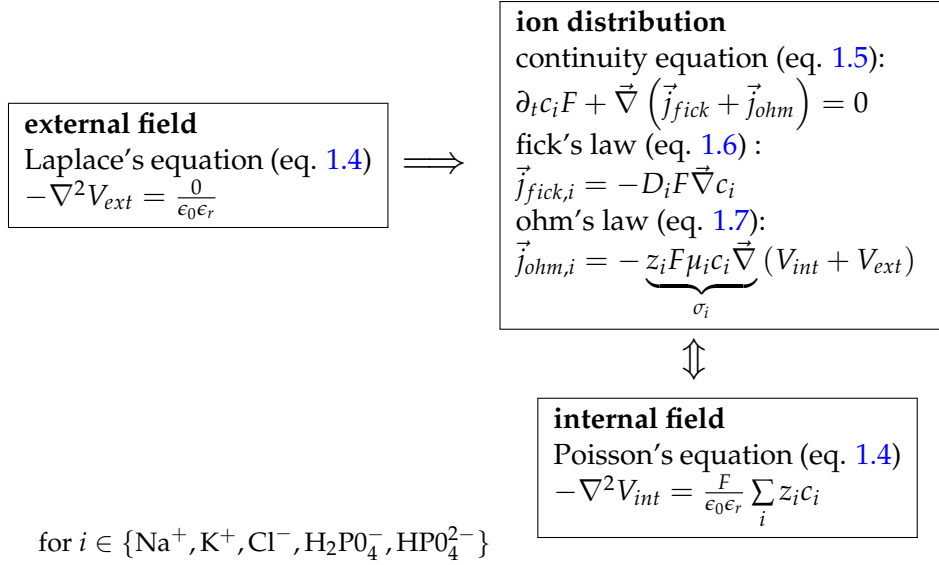


Figure 4.1: scheme of the working algorithm of the Finite Element simulation

In Fig. 4.1 $F = e \cdot N_A$ stands for the product of elementary charge and the Avogadro constant (called *Faraday constant*). D_i and μ_i refer to the isotropic diffusion and mobility constant, which are linked by Einstein's formula $\mu_i = \frac{q_i}{kT} D_i$.

4.2.2 Boundary Conditions

Table 4.1

geometry	ext. potential	int. potential	ion flux
box	ground	ground	no influx
shank	zero charge/symmetry	ground	no influx
stimulating el.	stimulation potential	ground	no influx/ BV poss.
recording el.	zero charge/symmetry	ground	no influx

Table 4.2: Boundary conditions of the finite element simulation. *BV poss.* refers to a possible implementation of the Butler-Volmer equation (eq. 1.32) as a boundary condition of the influx (not done in this simulation)

There are four different groups of boundaries. The outer limits of the simulation are determined by the dimensions of the box (section 4.2). Here both potentials as well as any transfer of mass or electrical charge has to vanish. For the shank material (made of silicone) as well as for the non-stimulating electrodes a zero surface charge was selected. On the one hand these electrodes are connected to ground potential

in the experiment, on the other hand these connections are interrupted by a $1\text{ G}\Omega$ resistance. A changing of the boundary condition to “ground” has no a major effect. At the recording electrodes an external potential was applied, following the stimulation function. In principle, an influx of ions can be selected here, representing faradaic currents. However, this is limited by extremely fine meshing of the surface (see sections 4.2 and 4.2.3). Within the very first layer of each solid surface there is no accumulation of charges leading to an internal potential. Because of consistency reasons, the internal potential was set to ground for each electrolyte-solid-surface.

4.2.3 Meshing

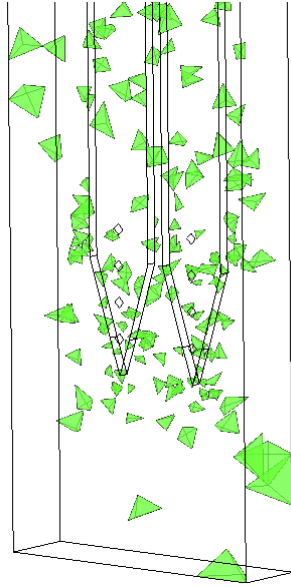


Figure 4.2: COMSOL meshing as it is done in the simulations. For reasons of overview just 1% of the mesh elements are shown

Fig. 4.2 shows a typical meshing of the finite element simulations done with about 55 000 mesh elements in total. The choice of quadratic Lagrange shape functions resulted in 11 degrees of freedom (dof) for every mesh element that had to be solved. With parameters like the *Element growth rate* or *Resolution at narrow regions*, the mesh can be selected to be finer at the boundaries or edges within certain limits. Though, in a steady state the potential drop is in a range of the debye-length [64] [65]. The number of mesh elements adequate to this rapid change can be estimated. The number of mesh-element directly at the surface of one single electrode would be at least $\text{number_of_mesh_elements} = \frac{A_{\text{electrode}}}{\lambda_{\text{Debye}}^2} = \frac{177 \times 10^{-12} \text{m}^2}{(7 \times 10^{-10} \text{m})^2} \approx 4 \times 10^8$.

With at least 3 layers in this range and 16 electrodes in total, this high number of mesh elements is just impracticable with respect to computing time.

4.3 Pretests

Before the simulation of this type was successful, various preliminary simulations were done. Starting with a one-dimensional capacitor with dimensions normed to one debye-length and two ion sorts, the model was transferred to SI-units and the distance of the two electrodes was enlarged to a range, which is conform with the multielectrode geometry. One of the major advantages of this model is, that it can be solved analytically in many cases and that the mesh-size can be selected finely enough, to come down to the debye-length to study also the potential drop at the boundaries. For reasons of simplicity, the first three dimensional geometry was selected to be a sphere in a box. Here the limits of meshing size and of unphysiological high concentrations of ions for a static state could be observed. This is implemented in the Poisson-Nernst-Planck equations (sections 1.2.2 and 4.2.1), which are neglecting the volume of the ions including their hydration layer (like in the equations for an ideal gas). Also the shape functions had to be adapted from *linear* to *quadratic* to prevent numerical artefacts, though leading to a higher computation time because of the rise of the degrees of freedom. When introducing the multielectrode geometry, two shanks of the four-shank multielectrode (see Fig. 2.3) were taken. This type of electrode was used in the cases where stimulation had to take place at the same MEA (see section 2.2), and also as a recording multielectrode with external stimulus (see section 2.3). Though it takes a longer computation time, the whole shank was simulated. As a last step the number of ion sorts was increased from 2 to 5 (see section 1.2.2) and the concentration of each sort was calculated more accurately (including the ratio of H_2PO_4^- to HPO_4^{2-}). The Goldman-potential (section 1.2.1) is seen as one criterion for the stimulation capabilities of a certain pulse. Therefore, an infinitesimal small excitable cell is thought with fixed intracellular ion concentrations. For a given concentration of Na^+ , K^+ , Cl^- , the Goldman potential can then be calculated for each point. At rest, the potential is about -70 mV (here around -66 mV), while for a successful stimulation it shall rise at least to -60 mV ([20] and section 1.2.1).

4.4 Results

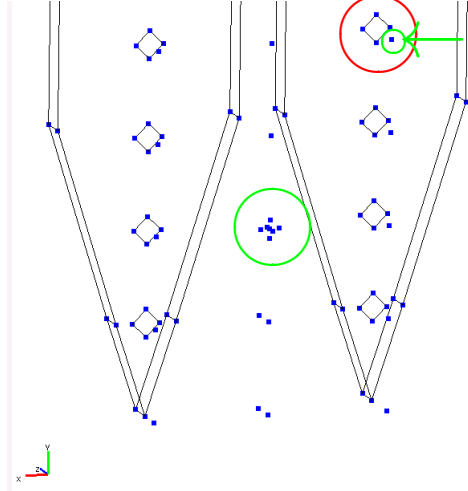


Figure 4.3: special points of interest in the finite element simulation

How fast can the ions react to a changing of the external potential? Since the upper limit for stimulation pulses found in literature is 0.1 ms (section 1.3.3), a sinusoidal simulation of 10^4 Hz with 1 V of amplitude was applied at one of the electrodes (○). As two examples the ion concentrations are plotted for a point in the vicinity of the stimulating electrode (←) and in the middle between the two electrode shanks (○). Because the ion concentrations are very different from each other (e.g. $c(\text{Na}^+) = 153 \text{ mM}$, $c(\text{K}^+) = 4.5 \text{ mM}$ (see section 1.2.2)), their values are displayed in relation to the starting or mean concentration.

The ion concentrations and the resulting internal potential are plotted for a point in the middle of the two shanks (far from the stimulating electrode):

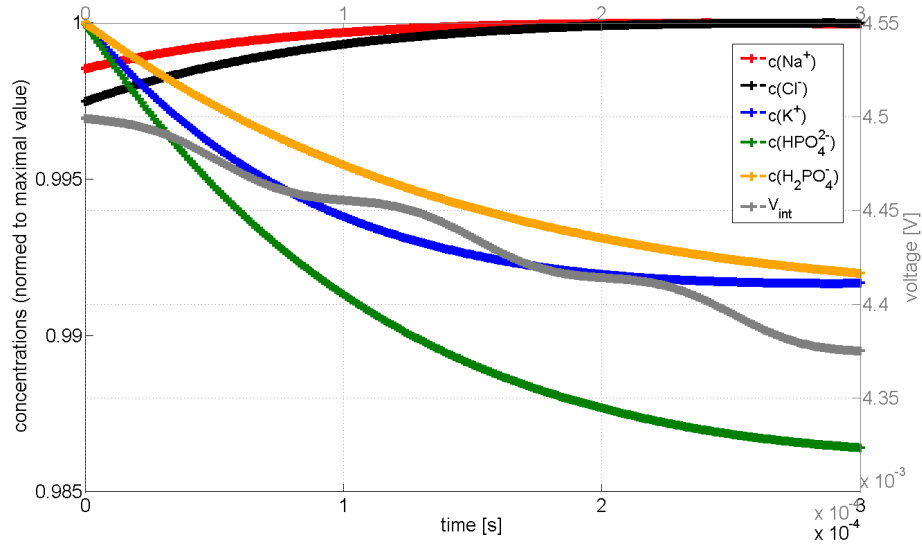


Figure 4.4: concentrations of all included ions and the resulting internal potential at a distance of $120 \mu\text{m}$

The external potential at the same point is a pure sine with the same frequency

Results

as applied (10 kHz) and an amplitude of ~ 1.6 mV. It is clear from this point that this is not enough to stimulate any tissue. It is seen in the graph, that the ion concentrations do not follow nor the external potential (no periodic behaviour), neither their electrical charge (Na^+ and Cl^- both raise in their concentration). Moreover, it seems to be relaxation effects and diffusion driven processes (as a start condition all loads are equally distributed). Just the internal potential behaves like a combination of drift and the periodic stimulus. In this case, the external

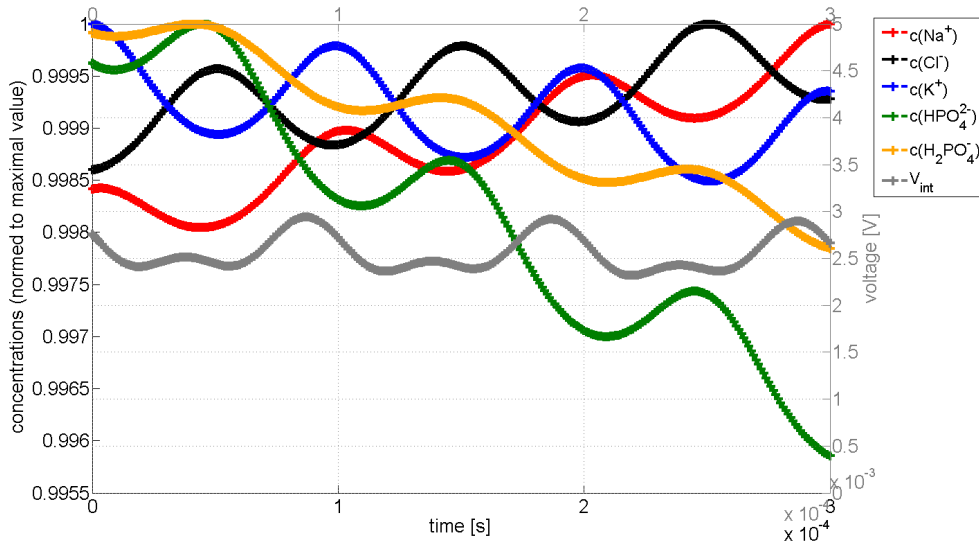


Figure 4.5: concentrations of all included ions and the resulting internal potential at a distance of $20 \mu\text{m}$

potential has an amplitude of still 120 mV (out of the 1 V applied). (This is in congruence with *Laotaveerungrueng et al.* [63] who simulated a potential drop from 1 V to 63 mV within the first $100 \mu\text{m}$ for a 1000 Hz biphasic pulse.) It can be seen, that within one half-period the concentrations of all negative charged ions are decreasing while the concentrations of the positively charged sodium and potassium are increasing. Apart from that, the relative concentration changes remain extremely low; the calculated Goldman-Potential also stays at -65 mV, varying just little (not shown here). So this high stimulating frequency is not able to influence the ions effectual.

The stimulating frequency is lowered to 500 Hz, while the amplitude continues to be 1 V (applied at the upper right electrode as before). Although for the Goldman potential extreme values of -230 mV and 30 mV are calculated, these values can be found just at the closest distance of the stimulating electrode and are therefore not reliable. The changes for the Goldman potential in Fig. 4.6 are far too small for a successful stimulation. In the middle of the two shanks minor changes are occurring

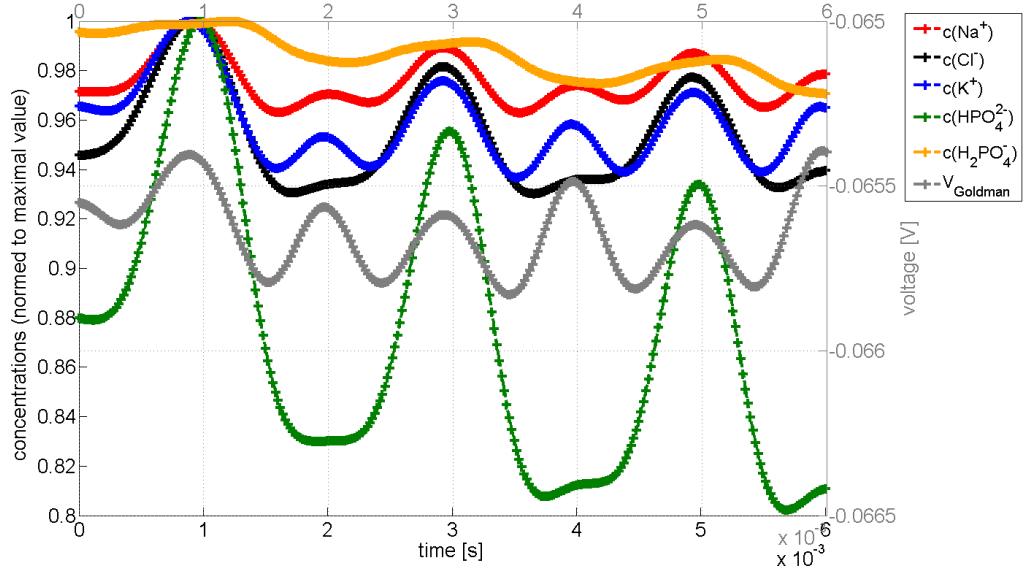


Figure 4.6: Ion concentrations (normed to their maximum) and the resulting Goldman potential when stimulating with a sine of 500 Hz and 1 V amplitude at a distance of $20\ \mu\text{m}$ from the stimulating electrode.

in the first two milliseconds due to relaxation from the starting conditions. After that, both the concentrations and the Goldman potential remain stable (see C.9 in the appendix). For this point (in the middle of the two shanks), the Activation function is calculated: Its value is primarily depending on the external potential. The "goal" of $940\ \frac{\text{V}}{\text{cm}^2}$ (see section 1.3.5) is not reached.

4.5 Summary and Outlook

The type of finite element simulation presented here is able to compute ion concentrations and the resulting electrical fields in the surrounding of a stimulating MEA. Introducing the Goldman potential and the Activation function, two tools are created to investigate the spatial distribution of neuronal excitation in PBS. Applying a sinusoidal stimulation of 10 kHz and 500 Hz comes to the result, that a pure capacitive stimulation by a single electrode is not considered to be sufficient. This simulation (and it's predecessor in 1-D) is also qualified for an understanding of the impact of time, diffusion constants and electrical charges. These parameters are not included in the equivalent circuit simulation (see chapter 3), where currents consist of electrons and are immediately flowing when voltages are applied.

Though, this simulation can be seen just as an approach for a new and more precise simulation. The achievement of a proper and much finer meshing persists to be a problem. The computation time and the numerical stability need to be improved. A

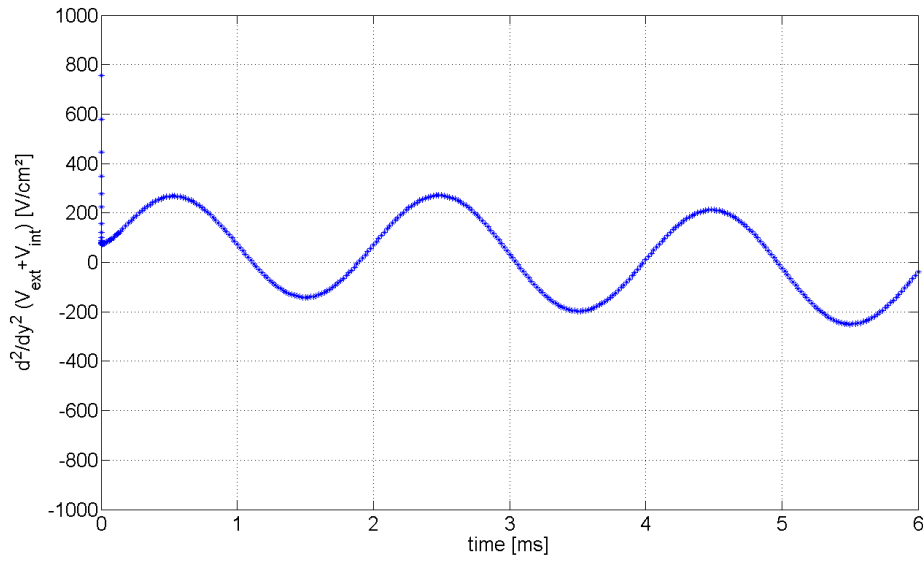


Figure 4.7: The Activation function calculated for a position between the shanks in a direction parallel to the shanks (y-axis)

ban on calculating with negative concentrations is also necessary. An idea might be the combination of a three-dimensional model with an one-dimensional simulation of this type or an equivalent circuit model for the electrode-electrolyte surface. By this method, also slower frequencies with greater perturbations in the saline could be investigated. If the concentrations of the reactants directly at the surface are known, the implementation of the Butler-Volmer equation is reasonable. A further alternative might be the simulation of the charged particles using C++ or python, as it is done in plasma physics.

Appendix A

Mathematical Methods

In this section two concepts of the analysis are presented, which are widely used in this thesis. The fourier series (section A.3) as a summation of sinuses and cosines is used in the generation of triangular and rectangular pulses, without running into problems when these functions are derived. The fractional order calculus (sections A.1 and A.2) is needed in the Simulation of the Constant Phase Element (see section 3.4).

A.1 Fractional Order Derivation

One model for describing the surface of electrode and saline is the *Constant Phase Element*. In chapter 3 it is shown, that for this element a wider concept of the derivation and integration is necessary.

Especially for numerical applications a definition of the fractional order derivative is given by Grünwald and Letnikov [66]

$$D_-^d f(t) = \lim_{h \rightarrow 0+} \frac{1}{h^d} \sum_{k=0}^{\infty} (-1)^k \binom{d}{k} f(t - kh) \quad (\text{A.1})$$

$$D_+^d f(t) = \lim_{h \rightarrow 0+} \frac{1}{h^d} \sum_{k=0}^{\infty} (-1)^k \binom{d}{k} f(t + kh) \quad (\text{A.2})$$

where d is the order of fractional differentiation. In amplification of the case where differentiation orders are integers, one can define the binomial coefficient as

$$\binom{d}{k} := \frac{\Gamma(d+1)}{\Gamma(k+1)\Gamma(d-k+1)} \quad (\text{A.3})$$

with the Gamma function [67]

$$\Gamma(z) = \int_0^{\infty} t^{z-1} e^{-t} dt, z \in \mathbb{C}, \text{Re } z \geq 0 \quad (\text{A.4})$$

It is clear at this point, that $\Gamma(d+1)$ is not defined for $d \leq 1$ and so the definitions A.1 and A.2 are not useful in finding a way of fractional order integration.

The Gamma function has the identities

$$\Gamma(z+1) = z\Gamma(z), \Gamma(1) = 1 \quad (\text{A.5})$$

which leads in the case of integer arguments to

$$\Gamma(n+1) = n! \quad (\text{A.6})$$

So, it is clear that definition of the binomial coefficient known from combinatorial analysis is fully reproduced by eq. A.3 :

$$\binom{d}{k} := \frac{\Gamma(d+1)}{\Gamma(k+1)\Gamma(d-k+1)} \quad (\text{A.7})$$

$$\stackrel{d,k \in \mathbb{Z}}{=} \frac{d!}{k!(d-k)!}$$

Though, this is not a mathematical estimation, the values of the generalized binomial coefficient for different values show a strong convergence to zero. For all the calculated differentiation orders d the binomial coefficient is less than 10^{-6} for $k > 6$. This leads to the assumption that it will be accurate enough to calculate the fractional order derivative with only a few preceding data points to the actual one (For this issue see also chapter 3.)

A.2 Fractional Order Integration

There are many expressions for the fractional order integration, which differ not too much. In this thesis the "Left side Weyl integral" [66] is used:

$$D_-^{-d} f(t) = \frac{1}{\Gamma(d)} \int_{-\infty}^t f(\tau) (\tau - t)^{d-1} d\tau \quad (\text{A.8})$$

This can be approximated for numerical purposes by

$$D_-^{-d} f(t) = \frac{1}{\Gamma(d)} \sum_{k=0}^{-\infty} f(t - kh) (k \cdot h)^{d-1} \cdot h \quad (\text{A.9})$$

where again $0 < d < 1$ Because of the proportionality $\frac{1}{k^{1-d}}$ this formula derives a not so fast convergence than in the case of fractional derivation.

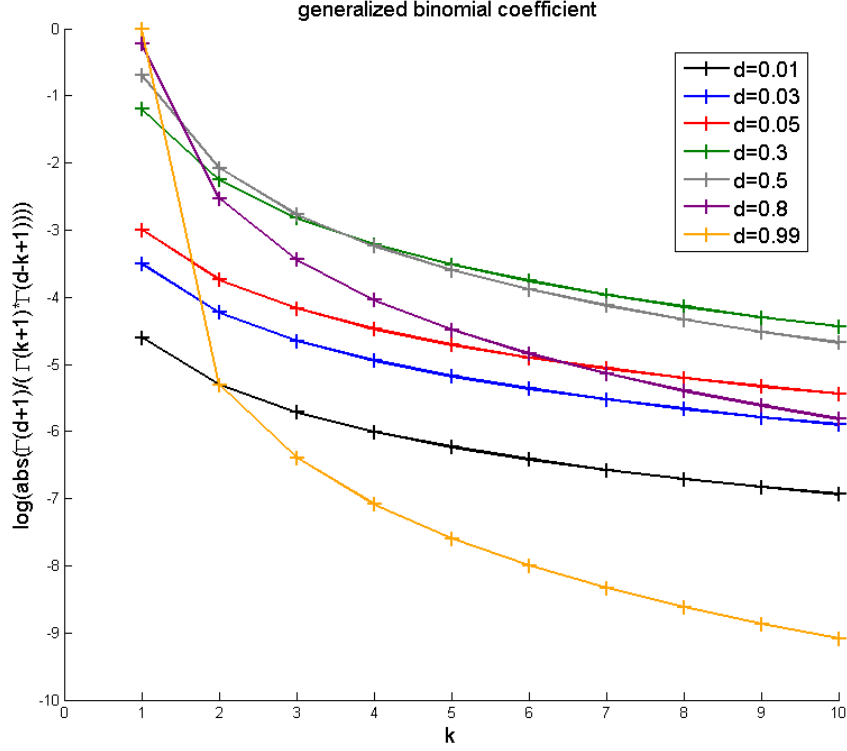


Figure A.1: The convergence of the general binomial coefficient $\binom{d}{k}$ as defined in eq. A.7 for different diffraction orders d

A.3 Selected Fourier Series

For generating the pulse forms in the simulations, sometimes a combination of trigonometric functions is used to create rectangular or triangular stimulation functions. An rectangular function of amplitude A can be described by a Fourier series of sinus (adapted from [68])

$$\begin{aligned}
 f_{rect} &= A (\Theta(\text{mod}_T t) - 2\Theta(\text{mod}_T (t - T))) \\
 &= A \lim_{n \rightarrow \infty} \frac{4}{\pi} \sum_{m=1}^n \frac{\sin((2m-1)t)}{2m-1} \\
 &= A \lim_{n \rightarrow \infty} f_n
 \end{aligned} \tag{A.10}$$

$T = \frac{1}{f}$ is the period, Θ the Heaviside step-function and mod_T means the modulo function to T . f_n is then called the n -th approximation function of f_{rect} .

The triangular function is used in the cyclic voltammetry (section 2.1.3.2), it can be described as a series of cosine [68]:

$$\begin{aligned}
 f_{\text{triang}} &= 1 - \left| 2 \frac{\text{mod}_T t}{T} - 1 \right| \\
 &= A \lim_{n \rightarrow \infty} \frac{8}{\pi^2} \sum_{m=1}^n \frac{\cos((2m-1)t)}{(2m-1)^2} \\
 &= A \lim_{n \rightarrow \infty} f_n
 \end{aligned} \tag{A.11}$$

Appendix B

Software

B.1 Recording Software

The software is able to present (and to save) the data of 64 recording channels (just 18 used for this thesis) at the same time or one selected in detail.

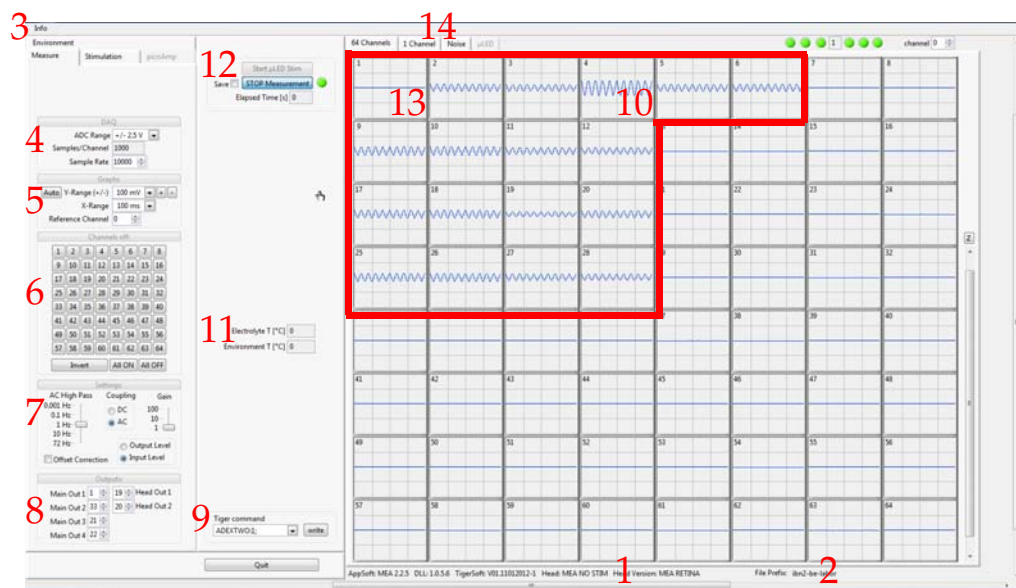


Figure B.1: graphic user interface and recording data display of the BioMAS-software

Before the measurement is possible, the correct headstage has to be recognized by the system (1), whereas a simulated head is also available to software development reasons. The name of the logged in user is taken for a measurement file prefix (2) and can be switched via the "info" dialog (3). A measurement range can be chosen (4) out of $\{\pm 2.5\text{ V}, \pm 5\text{ V}, \pm 10\text{ V}\}$ with the expected maximal voltage (4096 bits resolution). The X- and Y-range can be chosen and one channel out

of the 64 is able to be set as a reference channel (5) (since the signal is saved as displayed this modus for measurement is not recommended in general). Also some of the channels can be selected or deselected for measurement (6). 7: Here are the setting for the main amplifier (section 2.1.1), like the hardware high pass filter (the time constants are transferred to frequencies for easier handling), the AC or DC coupling and the gain. It has to be emphasized, that the headstage gain is independent of these settings. In the case of the preamplifier used (section 2.1.2), the total gain can be selected from $10\times$ up to $1000\times$ (a maximal error of the gain factors is 2% and systematic). For easier understanding the gain can be added out to an *input level*. If the *offset correction* is activated the data for each channel is subtracted by the mean of its data of the last 1 s. In the *Main out* (8) menu a maximum of 4 out of the 64 channels can be selected, which are then able to record externally using a LEMO-Adapter. With *Tiger command* (9) some direct commands can be sent to the micro controller, which works as an interface of software and hardware. The Variables *ADEXTONE* and *ADEXTWO* can be set either to 0 or 1. In the *ADEXTWO:1*; case, the channels 3 and 4 are recording from two channels at the backside of the main amplifier, instead taking the headstage signal. In the measurements presented in section 2.2.2 this function is used to record the stimulation signal on channel 4 (10) which comes from the main amplifier and is divided into two cables. Channel 3 which is also taking its signals from the backside of the main amplifier, is not connected. Its data is abolished in the further analysing process. One has to bear in mind, that the described signals **are not affected by the gain**, neither of the main amplifier, nor -of course- of the headstage and therefore have to be treated separately. The saving of further parameters 11, like the temperature of an incubator system is under development. Data measurement and display starts with a click on a *START* and *STOP* measurement button 11, whereas recording has to be started separately. It is automatically ceased, when the *STOP* measurement is activated.

The principle idea of the channels assignment (boxed in red) comes from a mapping the geometry of the four-shank-type multielectrode (Fig. 2.3) onto the recording channels of the system to assign changes in the data intuitively to change of the electrode geometry or a localized stimulation source. So each column stands for one shank with four electrodes. Each row represents the collectivity of electrodes of the same height. This symmetry is broken by the assignment of two main-amplifier channels (*ADEXTWO*) to channels 3 and 4. Because of that, the according recording channels of the headstage are put to Ch. 5 and 6. The data is renamed in the analysing software. To prevent cross talk in the headstage and preamplifier, the connections of the stimulating channel are grounded. In this case, on Channel 1

no signal can be seen (13). For a detailed view, just one channel can be display instead of all 64 at the 1 Channel mode (14), while at *noise* a live Fast-Fourier-Transformation of the signal is displayed. Originally developed for a close control especially of 50 Hz-noise, it was in this thesis to detect a stimulation frequency in preliminary tests when $SNR < 1$.

B.2 Developments in Stimulation Control

B.2.1 Dual Pulse Stimulation

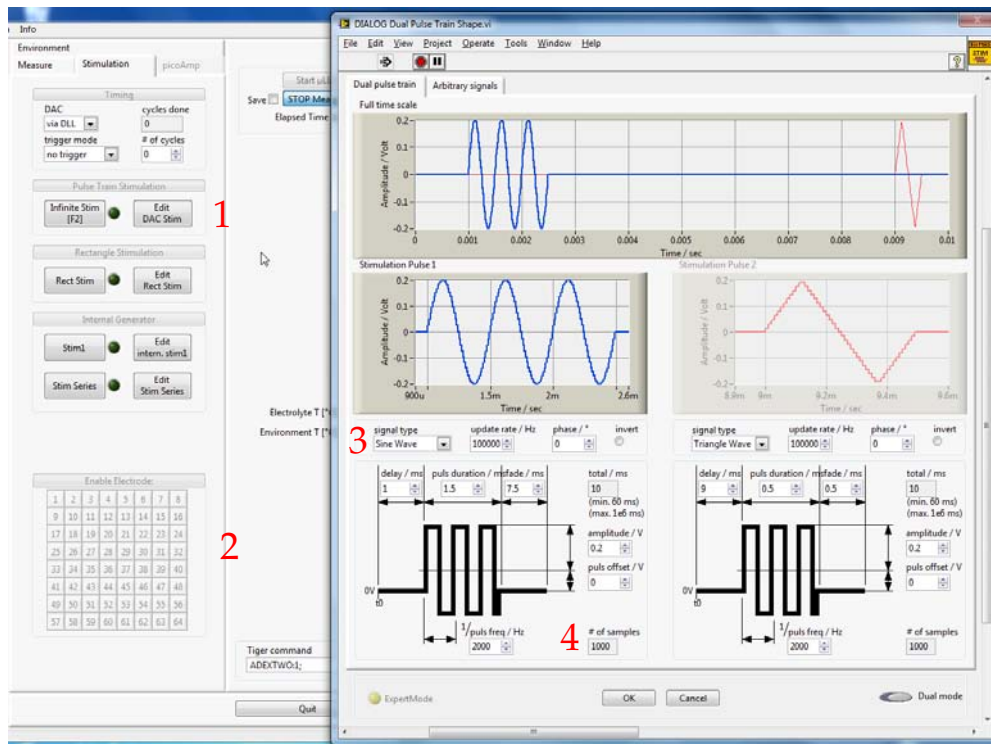


Figure B.2: graphic user interface of the developed dual pulse stimulation

After entering the pulse editing mode (1), a dialogue window opens (right half of the picture). On an arbitrary number of stimulation channels (2) one out of two stimulation functions can be applied. The signal type is limited to a sinus, triangular or rectangular function (3), but a wide range of parameters like amplitude, frequency, offset and time before and after each pulse can be chosen from a wide range of values. With # of samples (4) a determined number of pulses can be applied. An automatic synchronous saving of recorded data for the stimulation time cannot be achieved in this mode.

B.2.2 Arbitrary Pulse

To prepare for developments of future stimulation pulse forms (section 1.3.3.2), a modus was developed which enables the user to stimulate with arbitrary pulse forms at his own discretion.

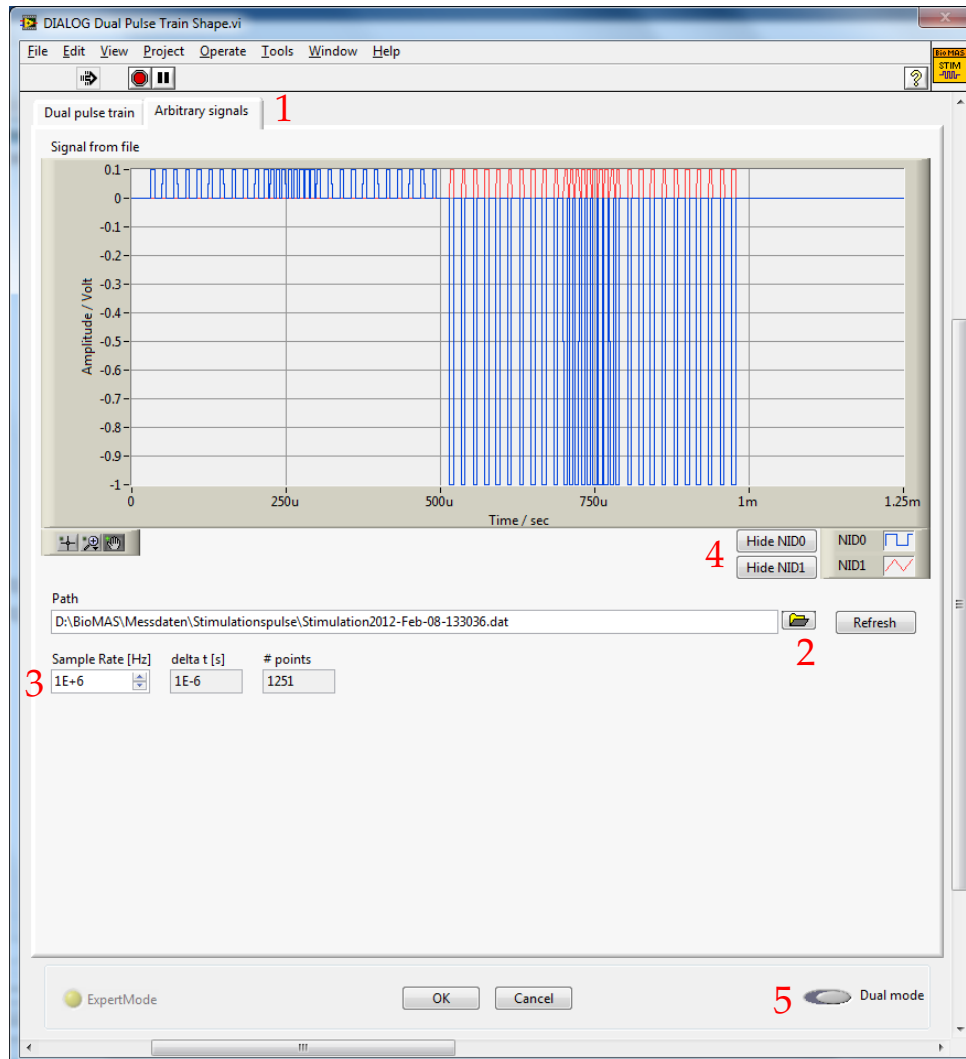


Figure B.3: graphic user interface of the developed arbitrary pulse stimulation module

When the *Arbitrary signals* tab (1) is selected in the *Edit DAC stim* mode (Fig. B.2), a stimulation file can be loaded (2). This file must be written in the Ascii-Format using *Doubles* with two columns separated by a tabulator and an additional tabulator afterwards. Since there is no additional column, the time has to be calculated with the *Sample Rate [Hz]* which can be adjusted via (3). The standard is set to 10^6 , which ends in a sampling time of $1\ \mu\text{s}$, but it can be

adapted from 1 Hz to 1.25 MHz. With this function, the same stimulation pulse data can be used for stimulation on different time scales. To get an overview of the stimulation shape, both pulses can be displayed separately (4). It is possible to stimulate with one stimulation function (first data column) or with both, depended on whether the *Dual mode* button is activated or not (5) .

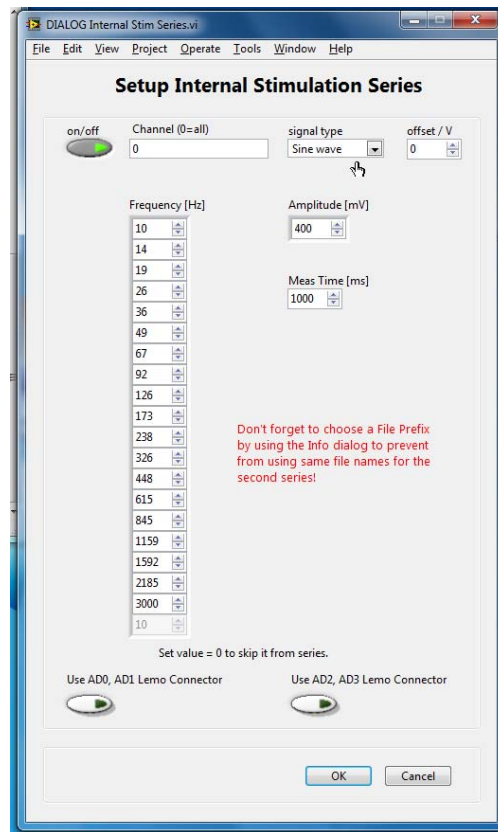


Figure B.4: Stimulation series module

SOFTWARE

Appendix C

Supplements to previous Chapters

C.1 Informal/Unpublished Literature

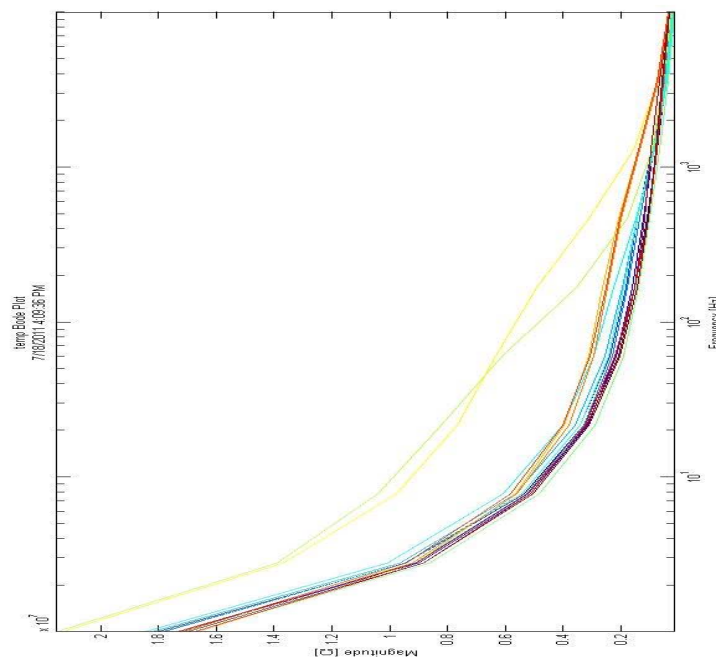


Figure C.1: impedance spectroscopy data of a $177 \mu\text{m}^2$ electrode (Neuronexus Technologies)

Intracortical Microstimulation (ICMS) with Microelectrodes

A common request we get from customers is on the parameters of safe microstimulation. The major issues are discussed below:

Back Voltage and Electrolysis

Via Ohm's Law: $I = V/R$, the amount of current that can be delivered with a given voltage is inversely related to the resistance of the charge-carrying material. Thus, the ideal stimulating electrode would have an infinitely low resistance. If resistance is too high, large voltages will be needed to drive appropriate current, which can result in the electrolysis of cerebrospinal fluid, causing oxygen and hydrogen bubbles to accumulate in the brain. The voltage required for electrolysis of brain fluid is 0.6 V and -0.8 V with our iridium oxide electrodes. We recommend the monitoring of back voltage during stimulation in your experiments to check whether your electrode is exceeding the electrolysis values, and using low impedance probes (50-300 k Ω). The two ways NeuroNexus lowers the impedance of its electrodes are through 1) fabricating probes with larger site sizes ($> 1000 \mu\text{m}^2$), and 2) increasing the charge capacity of existing probes by "activating" the electrodes to create an iridium oxide layer.

Capacitive/Faradaic Charge Delivery

Ideally, you want microstimulation to be capacitive, that is, you merely want an accumulation of charge on your electrode site, which results in an accumulation of counter ions near the electrode site, a change in the extracellular field potential, and thus depolarization or hyperpolarization of neurons. When charge delivery becomes faradaic, metal species leave the electrode material and may not redeposit back on the electrode during the counter phase. The value where microstimulation becomes faradaic is often called "charge capacity" and varies as a function of metal material. Calculated via cyclic voltammetry (CV), the charge capacity of iridium is 100-150 $\mu\text{C}/\text{cm}^2$, whereas iridium oxide is 1200 $\mu\text{C}/\text{cm}^2$. Thus, if you have an iridium oxide electrode site with a site size of 1250 μm^2 , the maximum current that can be delivered with a 200 μsec phase is:

$$\frac{\text{current} \cdot \text{time}}{\text{area}} \leq \text{capacity} \quad 1200 \mu\text{C}/\text{cm}^2 \cdot 1.250\text{E-}5 \text{ cm}^2 / 200\text{E-}6 \text{ sec} = 75 \mu\text{A}$$

In this case, note that any value higher than 75 μA may damage your electrode over time due to non-reversible faradaic reactions, and cause the charge carrying capacity to drop.

Tissue Damage

Other investigators [1] have empirically determined the relationship between charge delivery and tissue damage, and have developed the equation below:

$$\log\left(\frac{Q}{A}\right) = k - \log(Q) \quad \text{Which simplifies to:} \quad Q = \sqrt{A10^k}$$

Where Q is charge per phase in μC , A is surface area in cm^2 , and k is an empirically determined constant. If k exceeds 1.7, then tissue damage can occur. Thus, with a site size of 1250 μm^2 (or 1.250E-5 cm^2), the max charge that can be delivered is 0.025 μC . With a phase of 200 μsec , that yields a maximum current of 125 μA , regardless of electrode material.

[1] Merrill DR, Bikson M, Jefferys JG. Electrical stimulation of excitable tissue: design of efficacious and safe protocols. J Neurosci Methods. 2005 Feb 15;141(2):171-98.

Feedback/discussion can be e-mailed to: marzullo@neuronexustech.com

Please reference this document as: Marzullo T, Intracortical Microstimulation with Microelectrodes. Report Briefs. 2008 NeuroNexus Technologies.

NeuroNexus Technologies, Inc.

© 2008

3985 Research Park Dr, Suite 100 Ann Arbor, Michigan 48108
Tel: 734.913.8858 | Fax: 734.913.8859 | URL: www.NeuroNexusTech.com | Email: Support@NeuroNexusTech.com



C.2 SEM-Pictures

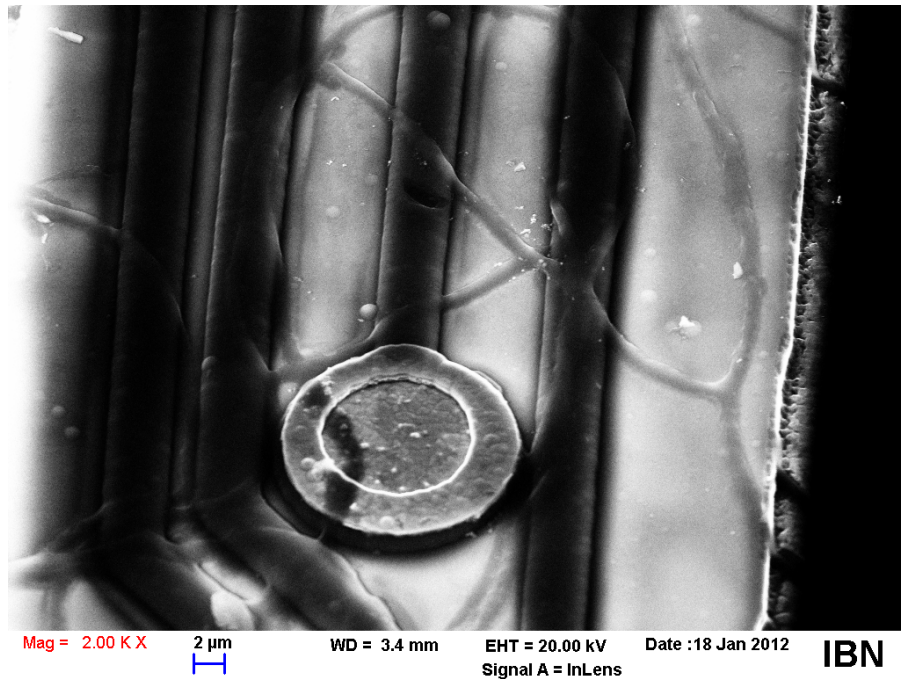


Figure C.2: SEM picture of the four shank multielectrode

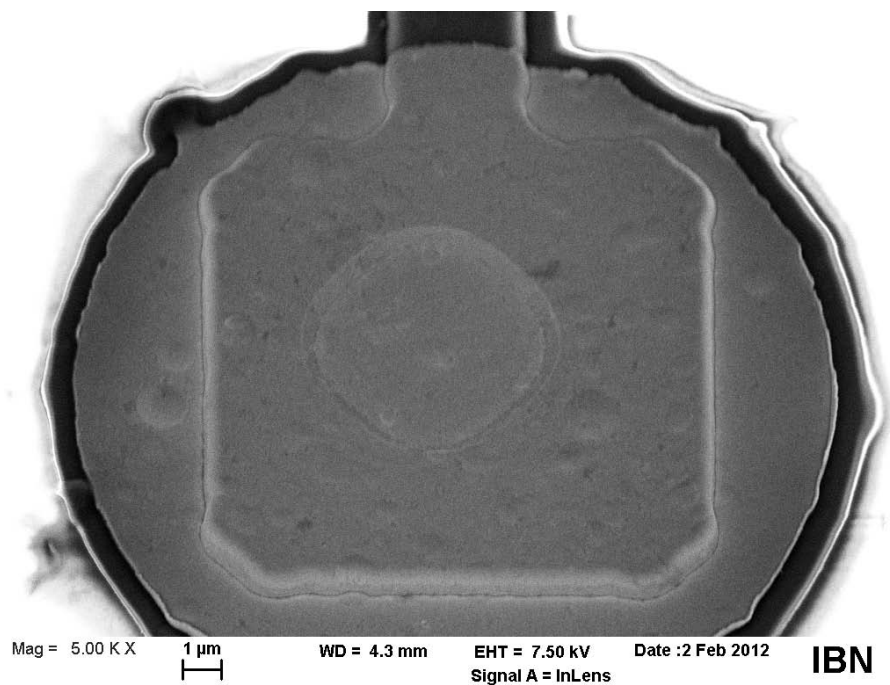


Figure C.3: SEM picture of a fresh electrode of the two-shank type

C.3 Previous Setups

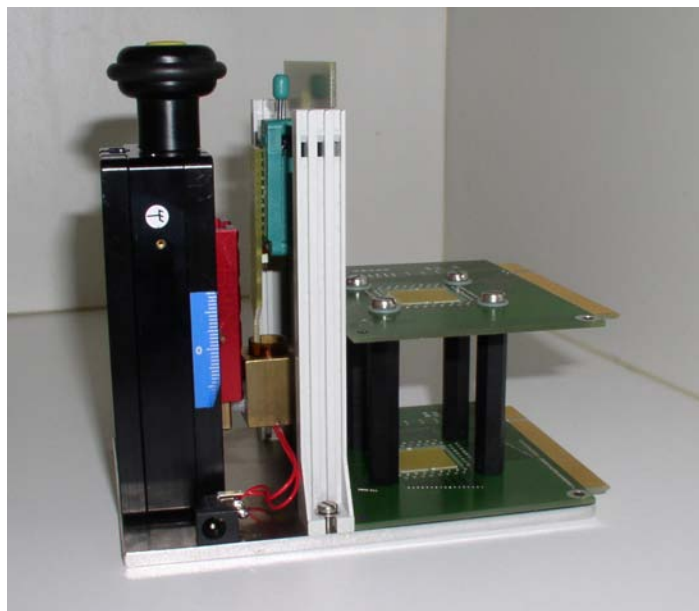


Figure C.4: first setup, yet without cables to the DIL-socket. It turned out, that the small glass for PBS is limiting the space for grounding electrode and does not allow to put neither a reference electrode nor a second multielectrode in

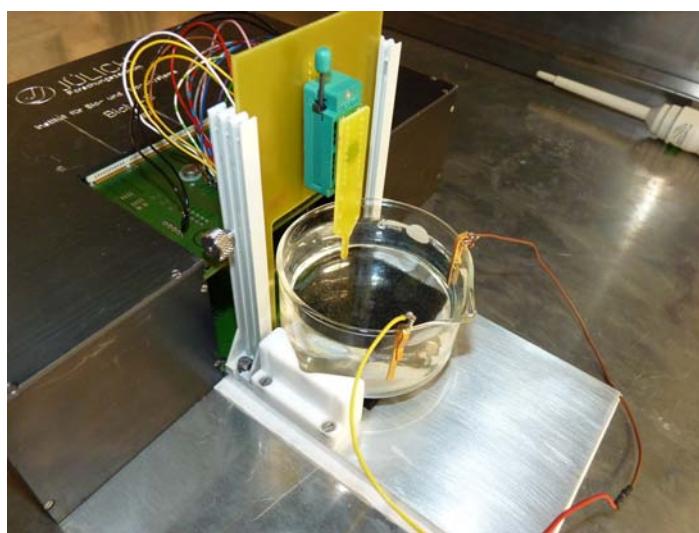


Figure C.5: second setup, with bigger pot for PBS. The unused channels are put to ground. But still extreme long feedlines to the DIL-socket.

C.4 Simulation based on an Equivalent Circuit Model

C.4.1 Impedance Spectroscopy R-CPE

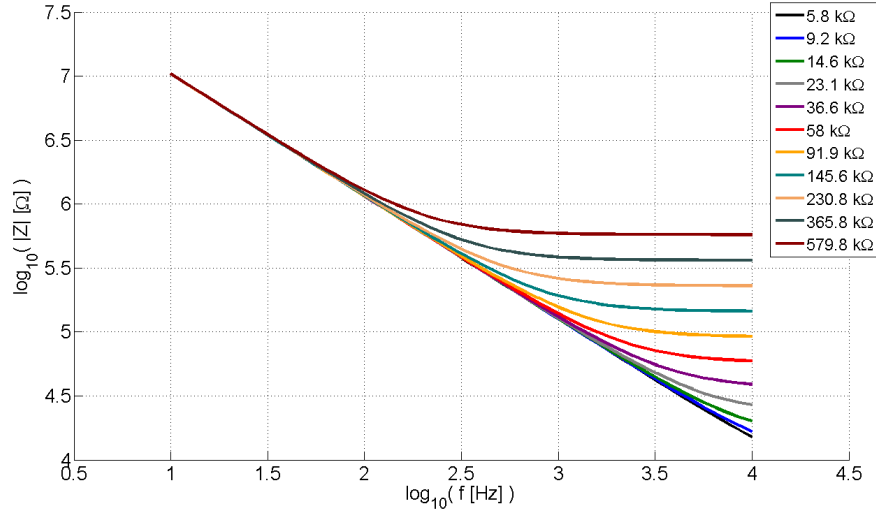


Figure C.6: influence of R on the impedance of the fitted $R Y_n$ -circuit

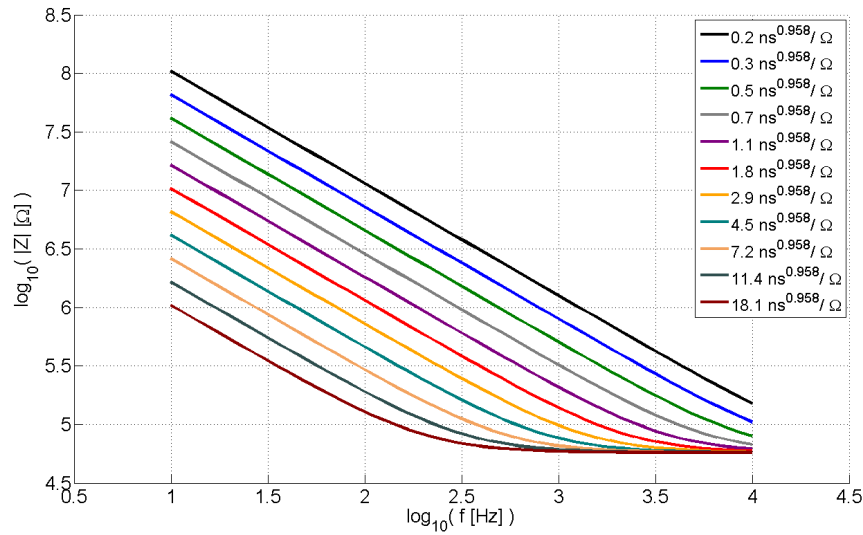


Figure C.7: influence of Y_n on the impedance of the fitted $R CPE$ -circuit

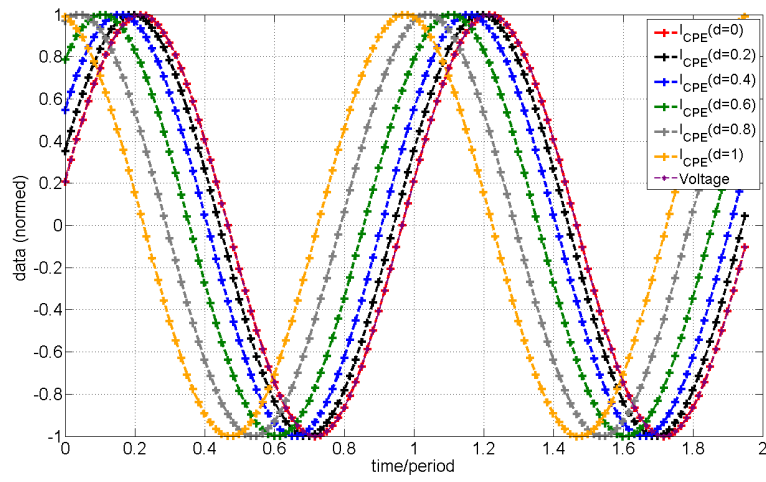


Figure C.8: phase of currents in a CPE-simulation in relation to the applied voltage vor different differentiation orders $d = n$

C.4.2 Limits of a R(RC)-circuit for high and low Voltages

$$\begin{aligned}
 \lim_{f \rightarrow \infty} |Z_{tot}| &= \lim_{f \rightarrow \infty} \left| R_1 + \left(\frac{1}{R_2} + i(2\pi f) C \right)^{-1} \right| \\
 &= \left| R_1 + \left(\frac{1}{R_2} + \lim_{f \rightarrow \infty} i(2\pi f) C \right)^{-1} \right| \\
 &= |R_1 + 0|
 \end{aligned} \tag{C.1}$$

$$\lim_{f \rightarrow 0} |Z_{tot}| = \lim_{f \rightarrow 0} \left| R_1 + \left(\frac{1}{R_2} + i(2\pi f) C \right)^{-1} \right| = \dots = |R_1 + R_2| \tag{C.2}$$

C.5 Finite Element Simulation

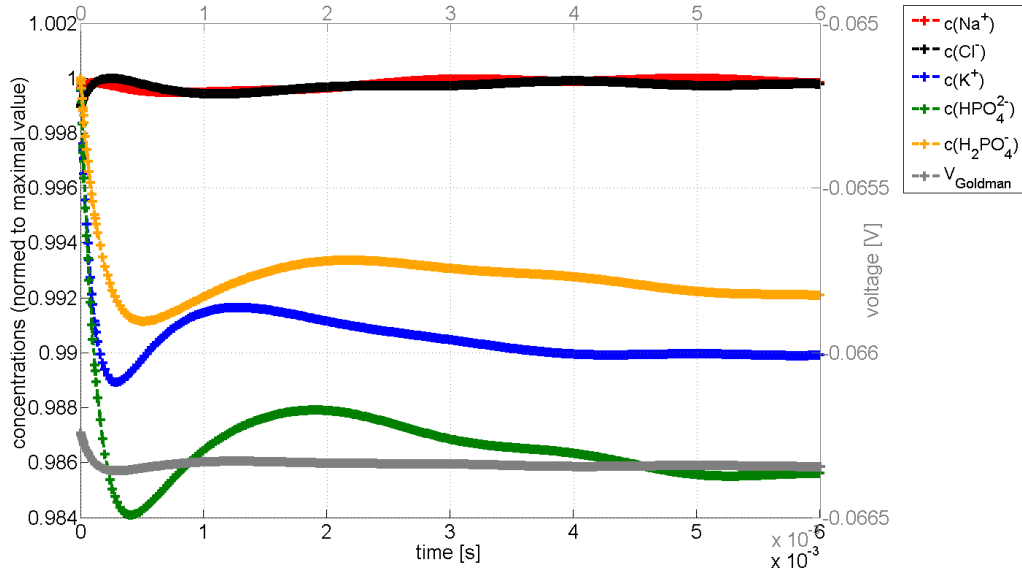


Figure C.9: Simulated ion concentrations (normed to their maximum) and the resulting Goldman potential when stimulating with a sinus of 500 Hz and 1 V at the middle of the two shanks

SUPPLEMENTS TO PREVIOUS CHAPTERS

Nomenclature

C_O	concentration of the oxidized reactant
C_R	concentration of the reduced reactant
E_{eq}	Equilibrium Potential, Nernst-Potential
$I(t)$	current into/from the electrode
I_{thr}	threshold current
R	universal gas constant
T	absolute temperature
$U_{+,-}$	the positive, negative part of a real function U
Z_{tot}	total impedance
α	transfer coefficient
\bar{r}_s	axon's resistivity
ϵ_r	dielectric constant
η	overpotential
\mathbb{Z}	set of integral numbers
V_{pp}	Voltage range peak-to-peak in V (in case of an ideal sine double the amplitude)
k^0	standard rate constant
∇^2	Laplace operator
ν_{sweep}	sweep rate
ρ	axoplasmic resistivity

SUPPLEMENTS TO PREVIOUS CHAPTERS

f	stimulation frequency
i_0	exchange current
l	length of an axon
r	radius of an axon
A	area, area of the electrode
AC	Alternating Current
AMD	age-related macular degeneration
BC	boundary conditions
BV	Butler-Volmer
ch.	channel
CPE	Constant Phase Element
DBS	Deep Brain Stimulation
DC	directive current
DIL	Dual In-line
dof	degree(s) of freedom
e	exponential function, electrical charge of an electron
ECF	extracellular fluid
eq.	equation
F	Faraday constant
Fig.	Figure
i	imaginary number with the identity $i^2 = -1$, summation index
IrOx	iridium oxide
k	Boltzmann constant
LED	light-emitting diode
LEMO-Adapter	Adapter type invented by Léon Mouttet

lg	logarithm to base 2, $\lg(2)=1$
ln	logarithm to base e, $\ln(e)=1$
log	logarithm to base 10, $\log(10)=1$
MEA	multielectrode array
n-D	n-dimensional
PBS	Phosphate Buffered Saline
PNP	Poisson-Nernst-Planck equation
RP	retinitis pigmentosa
SEM	Scanning Electron Microscope
SEM	scanning electron microscopy
SNR	signal-to-noise-ratio

Acknowledgments

Many thanks to **Prof. Dr. Andreas Offenhäusser** for the opportunity to work at this interesting field of research and for the supervision of this thesis.

I am also grateful to **Prof. Dr. Jörg Fitter** for his kind acceptance to be the second referee of this thesis.

My gratitude shall be expressed to **Prof. Dr. Bernhard Wolfrum** for the idea to go on for an equivalent-circuit model and discussions about the impedance spectroscopy data.

Many thanks to **Dr. Michael Pabst** for many passionate discussions in theoretical physics and for his advices in the Finite-Element model.

I am also thankful to **Janis Brusius** for his continuous practical help and his large efforts in reading the preversions of this thesis.

I am much obliged to **Jan Schnitker** for the SEM-pictures and his many ideas in the experiments.

The preamplifier has been designed by **Norbert Wolters**. I appreciate his help and his large expertise in electronics.

Many thanks to **Dieter Lomparski** for his patience in uncounted afternoons when improving and extending the BioMAS software for my purposes and to **Dieter Strobl** and his team for constructing the Faraday cage and many many smaller improvements of the mechanical devices.

I am grateful to **Mario Schloesser** and **Dr. Michael Schiek** for electronics specialised in the Neuronexus electrodes and their adapters.

I would also like to thank my mother, **Dr. Ruth Aichele**, and my twin sister, **Susanne Wehrse**, for the great support over the years. I look forward to the studies of human medicine together with Susanne for the next years in Aachen.

Bibliography

- [1] D. R. Merrill, M. Bikson, and J. G. R. Jefferys, "Electrical stimulation of excitable tissue: design of efficacious and safe protocols.," *Journal of neuroscience methods*, vol. 141, pp. 171–98, Feb. 2005. [cited on page 1, 7, 8, 9, 10, 12, 14, 27, 51, 52]
- [2] S. F. Cogan, "Neural stimulation and recording electrodes.," *Annual review of biomedical engineering*, vol. 10, pp. 275–309, Jan. 2008. [cited on page 1, 9, 12, 23, 24, 25, 58]
- [3] J. Buhlmann, L. Hofmann, P. A. Tass, and C. Hauptmann, "Modeling of a segmented electrode for desynchronizing deep brain stimulation," *Frontiers in Neuroengineering*, vol. 4, no. 00015, 2011. [cited on page 1, 10, 13, 14, 15, 89]
- [4] L. Wojtecki, C. Colosimo, and R. Fuentes, "Deep brain stimulation for movement disorders - a history of success and challenges to conquer.," *Frontiers in integrative neuroscience*, vol. 6, p. 6, Jan. 2012. [cited on page 1]
- [5] A. Sartorius and F. a. Henn, "Deep brain stimulation of the lateral habenula in treatment resistant major depression.," *Medical hypotheses*, vol. 69, pp. 1305–8, Jan. 2007. [cited on page 1]
- [6] A. Sartorius, "Remission of Major Depression Under Deep Brain Stimulation of the Lateral Habenula in a Therapy-Refractory Patient," *Biological Psychiatry*, vol. 67, no. 2, p. 2010, 2010. [cited on page 1, 3]
- [7] R. Carron, S. Chabardès, and C. Hammond, "Les mécanismes d' action de la stimulation cérébrale à haute fréquence. Revue de la littérature et concepts actuels," *Neurochirurgie*, vol. 469, p. 9, Mar. 2012. [cited on page 1]
- [8] J. D. Weiland, W. Liu, and M. S. Humayun, "Retinal prosthesis," *Annual review of biomedical engineering*, vol. 7, pp. 361–401, Jan 2005. [cited on page 1, 2]

BIBLIOGRAPHY

- [9] D. Bouccara, I. Mosnier, D. Bernardeschi, E. Ferrary, and O. Sterkers, "Cochlear implant in adults.," *La Revue de médecine interne / fondée ... par la Société nationale française de médecine interne*, vol. 33, pp. 143–9, Mar. 2012. [cited on page 1]
- [10] E. Kandel, J. Schwartz, and T. Jessell, *Principles of neural science*. New York: McGraw-Hill, 4th ed., 2000. [cited on page 1, 4]
- [11] F. Rattay, "Analysis of Models for External Stimulation of Axons," *IEEE Trans. Biomed. Eng.*, vol. 33, no. 10, pp. 974–977, 1986. [cited on page 1, 14]
- [12] F. Rattay, "High frequency electrostimulation of excitable cells.," *Journal of theoretical biology*, vol. 123, pp. 45–54, Nov. 1986. [cited on page 1]
- [13] S. A. Boven K-H, Fejtl M, Möller A, Nisch W, "On Micro-Electrode Array Revival," in *Advances in Network Electrophysiology Using Multi-Electrode Arrays* (M. Baudry and M. Taketani, eds.), pp. 24–37, New York: Springer Press, 2006. [cited on page 1]
- [14] D. Braeken, R. Huys, D. Jans, J. Loo, S. Severi, F. Vleugels, G. Borghs, G. Callewaert, and C. Bartic, "Local electrical stimulation of single adherent cells using three-dimensional electrode arrays with small interelectrode distances.," *Conference proceedings : ... Annual International Conference of the IEEE Engineering in Medicine and Biology Society. IEEE Engineering in Medicine and Biology Society. Conference*, vol. 2009, pp. 2756–9, Jan. 2009. [cited on page 1]
- [15] H. Kolb, "How the retina works," *American Scientist*, vol. 91, no. 1, p. 28, 2003. [cited on page 2, 3]
- [16] D. Harnack, C. Winter, W. Meissner, T. Reum, A. Kupsch, and R. Morgenstern, "The effects of electrode material, charge density and stimulation duration on the safety of high-frequency stimulation of the subthalamic nucleus in rats," *Journal of Neuroscience Methods*, vol. 138, no. 1-2, pp. 207–216, 2004. [cited on page 3, 9, 13, 63, 69]
- [17] X. Beebe and T. L. Rose, "Charge Injection Limits of Activated Iridium Oxide Electrodes with 0.2 ms Pulses in Bicarbonate Buffered Saline," *IEEE transactions on biomedical engineering*, vol. 3, no. 6, pp. 494–495, 1988. [cited on page 3]
- [18] N. L. Opie, A. N. Burkitt, H. Meffin, and D. B. Grayden, "Heating of the eye by a retinal prosthesis: modeling, cadaver and in vivo study.," *IEEE transactions on bio-medical engineering*, vol. 59, pp. 339–45, Feb. 2012. [cited on page 3]

- [19] U. Welsch, *Lehrbuch Histologie*. Munich: Elsevier, 3th ed., 2010. [cited on page 4]
- [20] R. F. Schmidt, F. Lang, and M. Heckmann, *Physiologie des Menschen mit Pathophysiologie*. Springer Heidelberg, 31st ed., 2011. [cited on page 4, 93]
- [21] K. R. Ward, E. J. F. Dickinson, and R. G. Compton, "How Far Do Membrane Potentials Extend in Space Beyond the Membrane Itself?," *International Journal of Electrochemical Science*, vol. 5, pp. 1527–1534, 2010. [cited on page 5]
- [22] A. Ames and F. B. Nesbett, "In vitro retina as an experimental model of the central nervous system.," *Journal of neurochemistry*, vol. 37, pp. 867–77, Oct. 1981. [cited on page 5, 63]
- [23] J. Sambrook and D. W. Russell, *Molecular Cloning A Laboratory Manual*. Cold Spring Harbor Laboratory Press, 3rd ed., Dec. 2001. [cited on page 5]
- [24] P. Vanysek, "Ionic Conductivity and Diffusion at Infinite Dilution," *CRC Handbook of Chemistry and Physics 92nd Edition Internet Version 2012*, 2011. [cited on page 5]
- [25] W. M. Haynes, *CRC Handbook of Chemistry and Physics*. National Institute of Standards and Technology, 92nd edition internet version 2012 ed., 2012. [cited on page 5, 7, 12]
- [26] A. Zeeck, *Chemie für Mediziner*. München: Urban & Fischer, 7th ed., 2010. [cited on page 5]
- [27] L. Hofmann, M. Ebert, P. A. Tass, and C. Hauptmann, "Modified pulse shapes for effective neural stimulation.," *Frontiers in neuroengineering*, vol. 4, p. 9, Jan. 2011. [cited on page 6, 10, 69]
- [28] U. Kaatze, "Complex permittivity of water as a function of frequency and temperature," *Journal of Chemical and Engineering Data* 34 (4), vol. 34, pp. 371–374, 1989. [cited on page 6]
- [29] J. B. Hasted, D. M. Ritson, and C. H. Collie, "Dielectric Properties of Aqueous Ionic Solutions. Parts I and II," *The Journal of Chemical Physics*, vol. 16, no. 1, p. 1, 1948. [cited on page 6]
- [30] G. Adam, P. Läuger, and G. Stark, *Physikalische Chemie*. Konstanz: Springer Heidelberg, 5th ed., 2009. [cited on page 7, 85]
- [31] S. Joucla and B. Yvert, "Improved focalization of electrical microstimulation using microelectrode arrays: a modeling study.," *PloS one*, vol. 4, p. e4828, Jan. 2009. [cited on page 7, 13, 89]

BIBLIOGRAPHY

- [32] O. Stern, "Zur Theorie der elektrolytischen Doppelschicht," *Zeitschrift für Elektrochemie*, vol. 30, pp. 508–516, 1924. [cited on page 8, 52]
- [33] D. Henderson and S. Lamperski, "Simple Description of the Capacitance of the Double Layer of a High Concentration Electrolyte," *Journal of Chemical & Engineering Data*, vol. 56, pp. 1204–1208, Apr. 2011. [cited on page 8, 85]
- [34] B. Conway and J. Mozota, "Surface and bulk processes at oxidized iridium electrodes-II. Conductivity switched behaviour of thick oxide films," *Electrochimica Acta*, vol. 28 (1), pp. 9–16, 1983. [cited on page 9, 26, 59]
- [35] W. M. Grill and X. F. Wei, "High efficiency electrodes for deep brain stimulation.," *Conference proceedings : 31st Annual International Conference of the IEEE Engineering in Medicine and Biology Society.*, vol. 978-1-4244, pp. 3298–3301, Jan. 2009. [cited on page 10, 89]
- [36] D. K. Freeman, D. K. Eddington, J. F. Rizzo, and S. I. Fried, "Selective activation of neuronal targets with sinusoidal electric stimulation.," *Journal of neurophysiology*, vol. 104, pp. 2778–91, Nov. 2010. [cited on page 10]
- [37] S. K. Kelly, J. L. Wyatt, and S. Member, "A Power-Efficient Neural Tissue Stimulator With Energy Recovery," *IEEE transactions on biomedical circuits and systems*, vol. 5, no. 1, pp. 20–29, 2011. [cited on page 10]
- [38] P. J. Langlois, A. Demosthenous, and I. Pachnis, "High-Power Integrated Stimulator Output Stages With Floating Discharge Over a Wide Voltage Range for Nerve Stimulation," *IEEE transactions on biomedical circuits and systems*, vol. 4, no. 1, pp. 39–48, 2010. [cited on page 10]
- [39] L. Robblee and T. Rose, "Electrochemical guidelines for selection of protocols and electrode materials of neural stimulation.," in *Neural Prosthesis: Fundamental Studies* (W. Agnew and McCreery DB, eds.), ch. 2, pp. 25–66, Englewood Cliffs, NJ Prentice Hall, 1990. [cited on page 12]
- [40] C. Koch, *Herstellung und Charakterisierung einer vollständig implantierbaren epiretinalen Sehprothese*. phd thesis, RWTH Aachen, 2011. [cited on page 11, 12, 24, 26, 59]
- [41] L. R. Bard, Allen J. Faulkner, *Electrochemical methods : fundamentals and applications*. New York: Wiley, 2001. [cited on page 12, 63]
- [42] A. L. Hodgkin, "A quantitative description of the membrane current and its application to conduction and excitation in nerve," *J Physiol*, vol. 117, no. 1952d, pp. 500–544, 1952. [cited on page 13]

- [43] C. C. McIntyre, A. G. Richardson, W. M. Grill, M. J. Birdno, A. M. Kuncel, A. D. Dorval, D. A. Turner, R. E. Gross, and W. M. Grill, "Modeling the Excitability of Mammalian Nerve Fibers : Influence of Afterpotentials on the Recovery Cycle Modeling the Excitability of Mammalian Nerve Fibers : Influence of Afterpotentials on the Recovery Cycle," *Journal of Neurophysiology*, vol. 87, pp. 995–1006, 2002. [cited on page 15]
- [44] A. Berntson and W. R. Taylor, "Response characteristics and receptive field widths of on-bipolar cells in the mouse retina.," *The Journal of physiology*, vol. 524 Pt 3, pp. 879–89, May 2000. [cited on page 15]
- [45] M. Krause, S. Ingebrandt, D. Richter, M. Denyer, M. Scholl, C. Sprossler, and A. Offenhausser, "Extended gate electrode arrays for extracellular signal recordings," *Sensors And Actuators B*, vol. 70, pp. 101–107, 2000. [cited on page 17]
- [46] H. Ecken, S. Ingebrandt, M. Krause, D. Richter, M. Hara, and a. Offenhäusser, "64-Channel extended gate electrode arrays for extracellular signal recording," *Electrochimica Acta*, vol. 48, pp. 3355–3362, Sept. 2003. [cited on page 17]
- [47] G. Wrobel, Y. Zhang, H.-J. Krause, N. Wolters, F. Sommerhage, A. Offenhäusser, and S. Ingebrandt, "Influence of the first amplifier stage in MEA systems on extracellular signal shapes.," *Biosensors & Bioelectronics*, vol. 22, pp. 1092–1096, Jan. 2007. [cited on page 17]
- [48] S. Eick, *Extracellular Stimulation of Individual Electrogenic Cells with Micro-Scaled Electrodes*. PhD thesis, RWTH Aachen, 2010. [cited on page 23, 25]
- [49] L. S. Robblee, J. I. Lefko, S. B. Brummer, and E. I. C. Laboratories, "Activated Ir : An Electrode Suitable for Reversible Charge Injection in Saline Solution," *Journal of the Electrochemical Society*, vol. 130 (3), pp. 731–733, 1983. [cited on page 25]
- [50] T. L. Aurian-Blajeni, B., Beebe, X., Rauh, R. D., and Rose, "Impedance of hydrated iridium oxide electrodes," *Electrochimica Acta*, vol. 34 (6), pp. 795–802, 1989. [cited on page 25, 65]
- [51] I.-S. Lee, C.-N. Whang, J.-C. Park, D.-H. Lee, and W.-S. Seo, "Biocompatibility and charge injection property of iridium film formed by ion beam assisted deposition," *Biomaterials*, vol. 24, pp. 2225–2231, June 2003. [cited on page 25, 65]

BIBLIOGRAPHY

- [52] D. Klein, S. L. Clauson, and S. F. Cogan, "Morphology and charge capacity of sputtered iridium oxide films," *Journal of Vacuum Science and Technology A - Vacuum Surfaces And Films*, vol. 7(5), no. December 1988, pp. 3043–3047, 1989. [cited on page 25, 65]
- [53] J. Mozota and B. Conway, "Surface and bulk processes at oxidized iridium electrodes-I. Monolayer stage and transition to reversivle oxide film behaviour," *Electrochimica Acta*, vol. 28 (1), pp. 1–8, 1983. [cited on page 26, 59]
- [54] S. Shah, A. Hines, D. Zhou, R. J. Greenberg, M. S. Humayun, and J. D. Weiland, "Electrical properties of retinal-electrode interface.," *Journal of neural engineering*, vol. 4, pp. S24–9, Mar. 2007. [cited on page 52]
- [55] W. Franks, I. Schenker, P. Schmutz, and A. Hierlemann, "Impedance characterization and modeling of electrodes for biomedical applications.," *IEEE transactions on bio-medical engineering*, vol. 52, no. 7, pp. 1295–302, 2005. [cited on page 52]
- [56] E. Warburg, "Ueber das verhalten sogenannter unpolarisirbarer elektroden gegen wechselstrom," *Annalen der Physik*, vol. 303, no. 3, pp. 493–499, 1899. [cited on page 53]
- [57] B. E. Conway, L. Ba, and M. A. Sattar, "Role of The Transfer Coefficient in Electrocatalysis : Applications to the H₂ and O₂ Evolution Reactions and The Characterization of Participating Adsorved Intermediates," *Int. J. Hydrogen Energy*, vol. 12, no. 9, pp. 607–621, 1987. [cited on page 63]
- [58] C. Song and J. Zhang, *Electrocatalytic Oxygen Reduction Reaction*. Springer Heidelberg, 1st edition ed., 2008. [cited on page 63, 64]
- [59] Ivo and Paseka, "Influence of hydrogen absorption in amorphous nip electrodes on double layer capacitance and charge transfer coefficient of hydrogen evolution reaction," *Electrochimica Acta*, vol. 44, no. 25, pp. 4551 – 4558, 1999. [cited on page 63]
- [60] Y. Sun, J. Lu, and L. Zhuang, "Rational determination of exchange current density for hydrogen electrode reactions at carbon-supported Pt catalysts," *Electrochimica Acta*, vol. 55, pp. 844–850, Jan. 2010. [cited on page 64]
- [61] R. Field and M. Ghowvanloo, "Finite Element Analysis of Planar Micromachined Silicon Electrodes for Cortical Stimulation," *Proceedings of 2006 International Conference on Microtechnologies in Medicine and Biology*, vol. TA17, pp. 221–224, 2006. [cited on page 89]

- [62] S. Raspopović, M. Capogrosso, X. Navarro, S. Micera, and S. Member, "Finite element and biophysics modelling of intraneural transversal electrodes: influence of active site shape," *32nd Annual International Conference of the IEEE EMBS Buenos Aires, Argentina*, pp. 1678–1681, 2010. [cited on page 89]
- [63] N. Laotaveerungrueng, C.-H. Lin, G. McCallum, S. Rajgopal, C. P. Steiner, A. R. Rezai, and M. Mehregany, "3-D microfabricated electrodes for targeted deep brain stimulation.," *Conference proceedings : Annual International Conference of the IEEE Engineering in Medicine and Biology Society. IEEE Engineering in Medicine and Biology Society. Conference*, vol. 2009, pp. 6493–6496, Jan. 2009. [cited on page 89, 95]
- [64] A. Golovnev and S. Trimper, "Steady state solution of the Poisson Nernst Planck equations," *Physics Letters A*, vol. 374, pp. 2886–2889, June 2010. [cited on page 90, 92]
- [65] M. Pabst, G. Wrobel, S. Ingebrandt, F. Sommerhage, and A. Offenhäusser, "Solution of the Poisson-Nernst-Planck equations in the cell-substrate interface.," *The European physical journal. E, Soft matter*, vol. 24, pp. 1–8, Sept. 2007. [cited on page 90, 92]
- [66] M. D. Ortigueira, *Fractional Calculus for Scientists and Engineers*, vol. 84. Springer Heidelberg, 2011. [cited on page 99, 100]
- [67] R. Remmert, *Funktionentheorie 2*. Springer Heidelberg, third ed., 2007. [cited on page 99]
- [68] H. Weber and H. Ulrich, *Laplace-Transformation*. Regensburg: Teubner, Wiesbaden, 8th ed., 2007. [cited on page 101]

Jül-4352
Juni 2012
ISSN 0944-2952